

NORTHWESTERN UNIVERSITY

Atomic Surface Structures of Oxide Materials: From Single Crystals to Nanoparticles

DISSERTATION

SUBMITTED TO THE GRADUATE SCHOOL  
IN PARTIAL FULFILLMENT OF THE REQUIREMENT

For the degree

DOCTOR OF PHILOSOPHY

Field of Materials Science and Engineering

By

Yuyuan Lin

EVANSTON, ILLINOIS

December 2014

UMI Number: 3669278

All rights reserved

INFORMATION TO ALL USERS

The quality of this reproduction is dependent upon the quality of the copy submitted.

In the unlikely event that the author did not send a complete manuscript and there are missing pages, these will be noted. Also, if material had to be removed, a note will indicate the deletion.



UMI 3669278

Published by ProQuest LLC (2014). Copyright in the Dissertation held by the Author.

Microform Edition © ProQuest LLC.

All rights reserved. This work is protected against unauthorized copying under Title 17, United States Code



ProQuest LLC.  
789 East Eisenhower Parkway  
P.O. Box 1346  
Ann Arbor, MI 48106 - 1346

© Copyright by Yuyuan Lin 2014

All Rights Reserved

## ABSTRACT

Atomic Surface Structures of Oxide Materials: From Single Crystals to Nanoparticles

Yuyuan Lin

Atomic surface structures of oxide materials are very important in many areas. Despite the importance, these structures are not fully understood, especially for the nanoparticles. In this study, the atomic surface structures of SrTiO<sub>3</sub> single crystals, SrTiO<sub>3</sub> nanocuboids, and CeO<sub>2</sub> nanoparticles are investigated by using a variety of techniques. The structural model for each system is proposed. In addition, the corresponding formation mechanisms and possible applications are discussed.

With STM image simulation, DFT energetics, BVS, and the previous knowledge of SrTiO<sub>3</sub> surface reconstructions, a structural model with a 4-fold symmetry is proposed for the (2×2) reconstruction on single crystal SrTiO<sub>3</sub>(001). The surface structure has a double-TiO<sub>2</sub>-layer feature and is very similar to the often observed c(4×2) surface reconstruction.

With aberration-corrected HREM, this study shows for the first time that the (100) surface of SrTiO<sub>3</sub> nanocuboids can be SrO, TiO<sub>2</sub>-rich reconstructions, or mixed with SrO and TiO<sub>2</sub>-rich reconstructions depending on the synthetic procedures. The findings are in agreement with DFT energetics, IR spectroscopic studies as well as surface acidity predictions.

With the oxygen atoms clearly observed by using aberration-corrected HREM, the atomic structures of (100), (110) and (111) surfaces on CeO<sub>2</sub> nanoparticles were determined for the first time. The (100) surface has a mixture of Ce, O and reduced CeO terminations on the outermost surface as well as the partially occupied lattice sites in the near-surface region (~1 nm from the



surface). The (110) surface has a combination of reduced flat  $\text{CeO}_{2-x}$  surface layers and “sawtooth-like” (111) nanofacets. The  $\text{CeO}_2$  (111) surface is O-terminated. The distinct amount of surface defects on the three facets implies the different surface redox properties.

In addition to the surface structures of as-prepared  $\text{SrTiO}_3$  and  $\text{CeO}_2$  nanoparticles, the atomic surface structures of the two nanoparticles under strong electron beam irradiation were investigated. The electron irradiation induces Ti-rich surface islands on the  $\text{SrTiO}_3$  nanocuboids and phase transformation of  $\text{CeO}_2$  to  $\text{Ce}_2\text{O}_3$ . The features of (100), (110), and (111) surfaces of  $\text{Ce}_2\text{O}_3$  are very similar to that of the  $\text{CeO}_2$ .

Approved by

Professor Laurence D. Marks

Department of Materials Science and Engineering

Northwestern University, Evanston, IL 60208, U.S.A

## Acknowledgements

First of all, I deeply appreciate my advisers Laurence Marks and Kenneth Poeppelmeier. Laurie's insight in science and concise and effective comments on my research are largely responsible for guiding me toward success in my PhD study. Laurie even helps me perform a lot of DFT calculations for my experimental results. Learning of Laurie's skills has enabled me to become an expert in electron microscopy. I would like to thank Laurie's patience during my first year as it was immensely helpful in allowing me to explore and learn most of the basics skills. I would also like to thank Laurie for holding high expectations for me in the later stage of my PhD career. His high expectations are important in giving me the proper trainings to thrive in the real world. As a student comes near to the end of his PhD career, Laurie has offered and continues to offer his guidance and support for my search for a future career path—whether it's a post-doctoral or an industrial career. I also want to thank Ken's help in my PhD study. Ken has provided me with a lot of freedom in conducting my researches. With Ken's help, I not only have been a materials scientist, but also have become a chemist. Ken often encourages me to talk to other people and learn about the American culture, which have significantly broadened my vision in science, social skills, and my appreciation for new cultures. I would also like to thank my thesis defense and qualifier committee: Professors Michael Bedzyk and Scott Barnett for their valuable time and suggestions.

I would like to thank my collaborators for their help in my PhD studies. Dr. Jianguo Wen's help in using the aberration-corrected TEM at Argonne National Laboratory has inspired some critical results in this thesis. Dr. Zili Wu's gracious help in materials synthesis and IR spectroscopy, as well as a lot useful suggestions significantly enriched my understandings in surface science and

catalysis. Without Dr. Andres E. Becerra-Toledo's help in DFT, I would not have finished the STM simulation project and a lot of other projects would have been slowed down. And I truly thank the STM results provided by Dr. Martin Castell's group. I need to thank Dr. Linhua Hu for synthesizing the SrTiO<sub>3</sub> nanocuboids using the oleic acid method, and Mr. Robert Kennedy for synthesizing the SrTiO<sub>3</sub> nanocuboids using the acetic acid method. Their materials are critical for my work in surface structure characterizations.

I must also thank my good friends and colleagues at Northwestern University who have helped me conduct researches and enjoy life. The students and postdoctors in Laurie and Ken's group have provided me with assistance and suggestions. I used a lot of Danielle Kienzle's DFT relaxed surface models for my PhD study. It is always very interesting to discuss with Yifeng. And I truly thank him for providing me with accommodation during my internship. It is very good to have Veerle, Romain, Yougui, Hongcheng, Chuandao, Jim E, Marty, Alicia, Dan, James, Karl, Kelvin, Robert and other people as my group members to study and work with. I wish Betty, Pratik, Lawrence, Emily, and Deniz success in their PhD studies and I am confident they will. I cannot forget the wonderful personnel at NUANCE center. Dr. Jinsong Wu and Dr. Shuyou Li provided me with my first hands-on lessons on how to use TEM. I appreciate them as they have always been nice and helpful when I had questions about using TEM. Wenyun Li and Baoxia Ren in NUANCE center have provided me very valuable tips in making good TEM samples. A special thanks to Ernest, CQ, Aiming, Shih-Han, Peijun, Nanjia, Martin, Shiqiang, Yi, and Jiaqing for all the interesting and useful discussions.

I would like to thank many wonderful people at Tulane University when I was conducting my Master's study. My adviser Ulli excited me to the study of surface science and gave me a great

first introduction to this research field. The people in Ulli's group provided me help in using STM, synthesizing nanostructure synthesis and in everyday life. It is a wonderful time to have Yunbin He, Peter Jacobson, Shaochun Li, Erie Morales, Khabibulakh Katsiev, Olga Dulub, Linghang Ying, Gareth Parkinson, and Jasim Uddin in the same research group. I need to thank Dr. Jibao He for teaching me to use the electron microscopes at Tulane. And I am very lucky to have my friends Jin Hu, Zifu Zhu, Ludi Miao, Fayong Luo, Shijia Zhang, Liu Liu, Tijiang Liu, and others to spend the first year in the USA with.

I appreciate Xiao Zhou's continuous help throughout my PhD career. At the end, I need to thank my parents for their selfless support in any and all circumstances. I cannot imagine my life without them.

## List of Abbreviations

AES Auger electron spectroscopy

ABF Annular bright field

ADF Annular dark field

ALD Atomic layer deposition

BF Bright field

BVS Bond valence sum

CMP Chemical mechanical polishing

DF Dark field

DFT Density functional theory

DL Double layer

DOS Density of States

LDOS Local density of states

EELS Electron energy loss spectroscopy

EDS Energy-dispersive X-ray spectroscopy

GGA Generalized gradient approximation

HAADF High angle annular dark field

HF Hartree-Fock

HREM High-resolution electron microscopy

ICP Inductively coupled plasma atomic emission spectroscopy

IR Infrared

LDA Local density approximation

LEED Low energy electron diffraction

PBE Perdew, Burke, Ernzerhof

RMT Muffin-tin radius

SOFC Solid oxide fuel cell

STEM Scanning transmission electron microscopy

STM Scanning tunneling microscopy

TEM Transmission electron microscopy

UHV Ultra-high vacuum

XPS X-ray photoelectron spectroscopy

XRD X-ray diffraction

## Table of Contents

<b>ABSTRACT.....</b>	<b>3</b>
<b>Acknowledgements.....</b>	<b>5</b>
<b>List of Abbreviations .....</b>	<b>8</b>
<b>Table of Contents .....</b>	<b>10</b>
<b>List of Figures.....</b>	<b>20</b>
<b>1. Introduction.....</b>	<b>21</b>
1.1 Motivation.....	21
1.2 Possible Surface Structures.....	23
1.3 Terminology of Surface Reconstructions .....	25
1.4 Organization.....	26
<b>2. Methods.....</b>	<b>28</b>
2.1 Introduction.....	28
2.2 Experimental.....	29
2.2.1 Electron-specimen interaction and TEM basics .....	29
2.2.2 HREM and STEM.....	30
2.2.3 TEM for surfaces.....	32
2.2.4 Electron diffraction .....	33
2.2.5 EELS .....	35
2.2.6 Infrared Spectroscopy .....	36
2.2.7 Auger Electron Spectroscopy and X-ray Photoemission Spectroscopy .....	37
2.2.8 Inductively coupled plasma atomic emission spectroscopy .....	39
2.3 Theoretical .....	39
2.3.1 DFT .....	39
2.3.2 Bond Valence Sum.....	43
2.3.3 STM and STM simulation.....	44
2.3.4 Introduction to HREM imaging theory .....	46
2.3.5 STEM.....	50
2.3.6 Multislice simulation for HREM.....	52
2.3.7 Direct methods .....	53

	11
<b>3. Surface Reconstructions of SrTiO<sub>3</sub> (001)</b> .....	<b>54</b>
3.1 Introduction.....	54
3.1.1 The Solved Surface Reconstructions of SrTiO <sub>3</sub> Single Crystals.....	55
3.1.2 Methods.....	61
3.1.3 Result and Discussion.....	62
3.1.4 Summary.....	69
<b>4. Atomic Surface Structures of CeO<sub>2</sub> nanoparticles</b> .....	<b>70</b>
4.1 Introduction.....	70
4.2 Experiment.....	75
4.3 Results and Discussion .....	76
4.3.1 (100) surface .....	77
4.3.2 (111) Surface.....	83
4.3.3 (110) surface .....	84
4.3.4 IR Spectroscopy.....	86
4.4 Summary.....	90
<b>5. Atomic Surface Structures of Ce<sub>2</sub>O<sub>3</sub> Nanoparticles</b> .....	<b>91</b>
5.1 Introduction.....	91
5.2 Experiment.....	96
5.3 Results and Discussion .....	96
5.3.1 (100) surface .....	99
5.3.2 (110) surface .....	105
5.3.3 (111) surface .....	111
5.4 Summary.....	113
<b>6. Synthesis Dependent Atomic Surface Structures of SrTiO<sub>3</sub> Nanocuboids</b> <b>114</b>	
6.1 Introduction.....	114
6.2 Experiment.....	115
6.3 Result and Discussion.....	118
6.3.1 Oleic Acid Synthesis.....	118
6.3.2 Acetic Acid Synthesis .....	124
6.3.3 Microwave Synthesis .....	126
6.3.4 Surface Formation Mechanisms.....	129



	12
6.4 Summary .....	136
<b>7. Electron-induced Ti-rich Surface Segregation on SrTiO<sub>3</sub> Nanocuboids.</b>	<b>137</b>
7.1 Introduction .....	137
7.2 Experiment .....	138
7.3 Results and Discussion .....	138
7.3.1 Beam damage .....	145
7.3.2 Mechanisms for the Surface Segregation .....	148
7.4 Summary .....	151
<b>8. Ongoing Projects and Future Directions .....</b>	<b>153</b>
8.1 Ongoing Projects .....	153
8.1.1 On the Plan-view HREM Surface Imaging .....	153
8.1.2 From Atomic Surface Structures to Catalytic Properties—Pt on SrTiO <sub>3</sub> Nanocuboids .....	159
8.2 Future Directions .....	161
8.2.1 Catalysts with Well-defined Shapes .....	161
8.2.2 Bimetallic Catalysts .....	162
8.2.3 Single Atom Catalysts .....	162
<b>Reference.....</b>	<b>164</b>

## List of Figures

Figure 1.1 Illustration of catalysts and catalytic reactions in heterogeneous catalysis. (a) A HAADF image of Pt catalysts on a SrTiO <sub>3</sub> support. (b) Illustration of adsorption, desorption, catalytic reactions.....	22
Figure 1.2 Some possible surface structures of oxides.....	25
Figure 1.3 Illustration of Wood's notation for surface reconstructions. Left: unit vectors of the surface structure and bulk structure. Right: a ( $\sqrt{2} \times \sqrt{2}$ ) surface reconstruction with the surface unit cell marked in green and bulk in black.....	26
Figure 2.1 Schematic view of a TEM setup and the electron-specimen interaction.....	30
Figure 2.2 Schematic view of the optics in HREM and STEM.....	32
Figure 2.3 Illustration of plan-view and profile-view surface imaging.....	33
Figure 2.4 Illustration of electron diffraction for surface structures in a TEM. A diffraction spot can be observed when the Ewald's sphere truncates a rel-rod.....	35
Figure 2.5 Schematic view of the interaction volume and the escape depths of different signals when an electron beam irradiates a specimen.....	38
Figure 2.6 Schematic view of the electron channeling model.....	47
Figure 3.1 The bulk and bulk truncated surface structures of SrTiO <sub>3</sub> .....	55
Figure 3.2 Side and top views of the DL-(2×1) model.....	57
Figure 3.3 Side and top views of the DL-(2×2) model.....	58
Figure 3.4 Side and top views of the DL-c(4×2) model.....	59
Figure 3.5 Illustration of the (3×3), ( $\sqrt{13} \times \sqrt{13}$ )R33.7°, and ( $\sqrt{5} \times \sqrt{5}$ )R26.6° surface models proposed by Kienzle et al.....	60
Figure 3.6 An experimental STM image shows a SrTiO <sub>3</sub> (001)-(2×2) surface reconstruction with a 4-fold symmetry. The inset shows the power spectrum of the image.....	63
Figure 3.7 The four (2×2) models used for STM simulation.....	65
Figure 3.8 The comparison of averaged experimental STM image and the simulated images using different models. (a) The averaged image of Fig. 3.6. (b)-(e) Simulated STM images using the models illustrated in Fig. 3.7(a)-(d) respectively.....	67

Figure 4.1 Schematic drawings of CeO<sub>2</sub> bulk structure (fluorite), surfaces and dipole moments. (a) A CeO<sub>2</sub> structural model with truncated {100}, {110}, and {111} surfaces. (b) Schematic view of the stacking of dipole moments along the [110] direction. The red and yellow squares represent O and Ce atoms and each arrow represents a dipole moment. The curly brackets represent a repeating unit. (c) Schematic view of the stacking of dipole moments along the [111] direction. The O-terminated (left) and Ce-terminated (111) (right) surfaces result in nonpolar and polar surfaces respectively. (c) Schematic view of the stacking of dipole moments along the [100] direction. The Ce-terminated (100) is a type III polar surface (left). The dipole moment can be compensated by transferring ½ O atoms from an O-terminated side to a Ce-terminated side (right). ..... 73

Figure 4.2 Illustration of the exposed facets of CeO<sub>2</sub> nanocubes. (a) Schematic view of the simplified and realistic exposed facets of a CeO<sub>2</sub> nanocube. (b) Experimental TEM image of a CeO<sub>2</sub> nanocube tilted to a [110] zone axis. .... 77

Figure 4.3 Experimental and simulated HREM results of the CeO<sub>2</sub> (100) surface. (a)-(b) Experimental HREM images of two {100} facets on the opposite sides of a CeO<sub>2</sub> nanocube. (c)-(h) The simulated HREM images of the different regions in (a) and (b), as indicated by the arrows. (i)-(n) The occupancies used in the simulation of each simulated HREM image. .... 78

Figure 4.4 Comparison between the partially occupied and fully occupied surface contrast. In Regions III-VI, (a) The cropped experimental images from Fig. 4.3(b). (b) The simulated HREM images using low surface atom occupancies. (c) The simulated HREM images with 100% atom occupancies. .... 80

Figure 4.5 HREM images taken at two different defocus. (a) The same image as in Fig. 4.3(b). (b) The image taken at a defocus ~1.5 nm less than (a). The arrows indicate O atoms. (c) A simulated HREM image for the area in the yellow box in (b) using the reconstructed CeO-terminated surface. (d) A simulated HREM image using the same condition as in (c) but with a Ce termination. .... 81

Figure 4.6 Time series of HREM images show the atomic diffusion of CeO<sub>2</sub> (100) surface, recorded at a time interval of 1 s. For the series of images, the bright spots are atoms. .... 83

Figure 4.7 (111) surfaces of a CeO<sub>2</sub> nanocubes. (a) An experimental HREM image on a (111) surface of CeO<sub>2</sub> nanocubes at [110] zone axis. (b) A simulated HREM image of the CeO<sub>2</sub> (111)

- surface with an O termination. The structural model is overlaid on the atom positions. (c) A simulated HREM image of the CeO<sub>2</sub> (111) surface with a Ce termination. .... 84
- Figure 4.8 (110) surfaces of CeO<sub>2</sub> nanocubes. (a) An experimental HREM image on a (110) surface of CeO<sub>2</sub> nanocubes at [110] zone axis. The white arrows indicate (111) nanofacets. (b) A simulated HREM image of the CeO<sub>2</sub> (110) surface with a CeO<sub>2</sub> surface termination. The structural model is overlaid on the atom positions. (c) A simulated HREM image of the CeO<sub>2</sub> (110) surface with a Ce termination. (d) Integrated line profiles from A1 to A2 indicated in (a). O vacancies are indicated by the squares (□). .... 85
- Figure 4.9 Size of {111} and {110} facets. (a) The size of a (111) facet of a relatively large nanocube (~70nm edge length). The edge length of the (111) facet is close to 1.5nm. (b) The size of a (111) facet of a nanocube with the size close to the average. The width of the (110) facet is close to 1.5 nm too. Note that the width of {110} facets are the same as the edge length of {111} facets. .... 89
- Figure 5.1 Structural models of cerium oxides. (a) The unit cell of A-type Ce<sub>2</sub>O<sub>3</sub>. (b) a 2×2×2 supercell of CeO<sub>2</sub> unit cells. (c) The unit cell of C-type Ce<sub>2</sub>O<sub>3</sub>. .... 93
- Figure 5.2 Illustration of phase transformation from fluorite CeO<sub>2</sub> to bixbyite Ce<sub>2</sub>O<sub>3</sub>. (a) A 2×2×2 supercell with ¼ of oxygen atoms missing. (b) The positions of d-site and b-site Ce atoms in C-type Ce<sub>2</sub>O<sub>3</sub>. (c) The unit cell and (100) surfaces of C-type Ce<sub>2</sub>O<sub>3</sub>, which is generated after a translation of the origin and relaxation from (a). (d) The atomic model of a (110) surface of C-type Ce<sub>2</sub>O<sub>3</sub>. (e) The atomic model of a (111) surface of C-type Ce<sub>2</sub>O<sub>3</sub>. .... 95
- Figure 5.3 Phase transformation from CeO<sub>2</sub> to C-type Ce<sub>2</sub>O<sub>3</sub>. (a) A HREM image of a CeO<sub>2</sub> nanocube. The inset shows the power spectrum. (b) A HREM image of a C-type Ce<sub>2</sub>O<sub>3</sub> nanocube. The inset shows the power spectrum. (c) EELS shows the difference between CeO<sub>2</sub> and Ce<sub>2</sub>O<sub>3</sub>. .... 98
- Figure 5.4 Experimental and simulated HREM images of a Ce<sub>2</sub>O<sub>3</sub> (100) surface. (a) and (b) Two experimental HREM images taken with a 2 nm difference in defocus. (c)-(e) The simulated HREM images using a O-, Ce<sub>4</sub>O<sub>3</sub>-, and Ce-terminated surface model respectively. .... 101
- Figure 5.5 Comparison between the partially occupied and fully occupied surface contrast. (a), (d),(h),(k) Simulated HREM images using a O-terminated (100) surface model. (b),(e),(i),(l) Simulated HREM images using a Ce<sub>4</sub>O<sub>3</sub>-terminated model. (c),(f),(j),(m) Simulated HREM

- images using a Ce-terminated model. Imaging conditions: (a)-(f) Simulated HREM images with the specimen thickness of 6 nm and defocus of 1 nm. (h)-(m) Simulated HREM images with the specimen thickness of 12 nm and defocus of -2 nm. 50% atomic occupancies were used for the outmost two surface layers in images (a), (b), (c), (h), (i), and (j). 100% atomic occupancies were used for the outmost two surface layers in images (d), (e), (k), (k), (l), and (m). ..... 102
- Figure 5.6 Surfaces of another Ce<sub>2</sub>O<sub>3</sub> nanoparticle with the surface cation layer as Ce-d. .... 104
- Figure 5.7 Atomic structures of the Ce<sub>2</sub>O<sub>3</sub> (110) surface. (a) The original HREM image of the Ce<sub>2</sub>O<sub>3</sub> (110) surface. (b) A simulated HREM image of (a) with a Ce<sub>2</sub>O<sub>3</sub>(Ce-d) termination. (c) A HREM image after 64s of continuous electron beam irradiation since (a) was recorded. (d) A simulated HREM image of (c) with a Ce<sub>2</sub>O<sub>3</sub>(Ce-m) termination. .... 106
- Figure 5.8 Evolution of C-type Ce<sub>2</sub>O<sub>3</sub> (110) surface from a Ce<sub>2</sub>O<sub>3</sub>(Ce-d) layer termination to a Ce<sub>2</sub>O<sub>3</sub>(Ce-m) layer termination. The images were selected from a time-series of 50 images with 1 s interval. .... 107
- Figure 5.9 Evolution of C-type Ce<sub>2</sub>O<sub>3</sub> (110) surface from a Ce<sub>2</sub>O<sub>3</sub>(Ce-m) termination to a Ce<sub>2</sub>O<sub>3</sub>(Ce-d) layer termination. The images were selected from another time-series of 50 images with 1s interval. .... 108
- Figure 5.10 Comparison of Ce<sub>2</sub>O<sub>3</sub>(Ce-m) and Ce<sub>2</sub>O<sub>3</sub>(Ce-d) surface terminations. (a) A (110) surface shows an initial termination of the Ce<sub>2</sub>O<sub>3</sub>(Ce-m). (b) Surface structure of Ce<sub>2</sub>O<sub>3</sub>(Ce-d). (c) Surface structure of Ce<sub>2</sub>O<sub>3</sub>(Ce-m). The blue boxes indicate unit cells of the two surfaces. The coordinations of each Ce atoms in the unit cell is indicated. .... 110
- Figure 5.11 Experimental and Simulated HREM images of the (111) surface of a Ce<sub>2</sub>O<sub>3</sub> nanoparticle. (a) Experimental HREM image. (b), (c) Simulated HREM images using an O- and Ce-terminated (111) surface model respectively. Parameters for simulation: defocus 2 nm, thickness 3.2 nm. .... 112
- Figure 6.1 Schematic view of three different hydrothermal methods in synthesizing SrTiO<sub>3</sub> nanocuboids. .... 117
- Figure 6.2 HREM results of SrTiO<sub>3</sub> nanocuboids synthesized by the oleic acid assisted process. (a) Low magnification experimental HREM image of SrTiO<sub>3</sub> nanocuboid in [110] viewing direction. (b) The power spectrum of (a). (c) High magnification image of (a), where the bright spots can be interpreted as atoms. (d) Simulated HREM image of (c). In (c), due to the cuboid

- nature of the sample, the sample thickness and defocus are increasing from left to right. Therefore, (d) is generated using 3 images simulated with continual changing defocus and thickness, which are increasing from left to right. .... 119
- Figure 6.3 Simulated and experimental HREM images using different surface structural models under the same imaging conditions. Clearly the SrO-(1×1) matches with the experiment best (image dimension:  $8.3 \times 24.5 \text{ \AA}^2$  for all). .... 121
- Figure 6.4 Comparison of the surface relaxation by using different DFT functionals. (a) Interlayer spacing comparison of the experimental image and simulated images for unrelaxed and DFT relaxed structures. The comparison is based on the area marked in the red box in Fig. 6.2(c). The interlayer spacings (i) are measured from Gaussian fits to the peak positions of the SrO-Ti atomic columns from the surface into the bulk. The error bars indicate the experimental deviation with respect to the mean values. (b) Cumulative error comparison between the DFT calculation using the PBE and the PBEsol0 functional. The base line was chosen as the 10th layer in the bulk from the surface (j=1 is the 10<sup>th</sup> interlayer spacing from the surface). .... 123
- Figure 6.5 Interlayer spacing oscillation is dependent on the thickness and coma. (a) At defocus=2nm, thickness=5nm, the best coma is at around 286Å. (b) By setting the aberrations fixed (coma at 286Å), changing the thickness, the best thickness is found at 50Å. .... 124
- Figure 6.6 HREM images from the acetic acid synthesis. (b) Experimental HREM image of a SrTiO<sub>3</sub> nanocuboid along [110]. (a) Low magnification image of (b). The inset shows the power spectrum. (c) A simulated image using a RT13 reconstructed surface. The RT13 atomic surface structures along the [110] viewing direction is overlaid in (b). In (b), owing to the nature of the sample, the sample thickness and defocus are increasing from right to left. Therefore, (c) was generated using 3 images simulated with different defocus and thickness, increasing from right to left. .... 125
- Figure 6.7 Simulated images using different surface reconstructions with the same imaging conditions. Clearly the locally ordered  $(\sqrt{13} \times \sqrt{13})R33.7^\circ$ ,  $(\sqrt{5} \times \sqrt{5})R26.6^\circ$  and  $(3 \times 3)$  reconstructions match with the experiment better than the well-ordered ones (image dimension:  $8.3 \times 23.0 \text{ \AA}^2$  for all). .... 126
- Figure 6.8 HREM images of SrTiO<sub>3</sub> nanocuboids obtained by the MA-HT synthesis. (b) Experimental HREM image of a SrTiO<sub>3</sub> nanocuboid along [110]. (a) Low magnification image

of (b). The inset show the power spectrum of (a). (c) A simulated image using a SrO terminated surface (areas with red arrows) and a layered structure model consisting of 50% of SrO and 50% of (3×3) surface terminations (areas with blue arrows). The (3×3) and SrO atomic surface structures along [110] is overlaid in (b). In (b), owing to the nature of the sample, the sample thickness and defocus are increasing from right to left. Therefore, (c) was generated using 4 images simulated with different defocus and thickness, increasing from right to left. .... 127

Figure 6.9 Simulated images using different surface reconstructions with the same imaging conditions. (image dimension:  $8.3 \times 23.3 \text{ \AA}^2$  for the simulated images,  $19.7 \times 23.3 \text{ \AA}^2$  for the experimental image)..... 128

Figure 6.10 Comparison of the experimental images, simulated images with the pure (3×3) reconstructed surface structure, and the layered structure with 50% of SrO and 50% of (3×3) surface (image dimension:  $8.3 \times 14.9 \text{ \AA}^2$  for all)..... 129

Figure 6.11 Comparative FT-IR study on the fresh SrTiO<sub>3</sub> nanocuboids (NC-with oleic acid), the ones after ethanol washing (NC after ethanol washing) and the ones after 600°C air annealing (NC-without oleic acid). The vibration absorbance peaks at  $1555 \text{ cm}^{-1}$  and  $1466 \text{ cm}^{-1}$  were assigned to asymmetric and symmetric stretching vibration of COO<sup>-</sup> of oleic acid. The peaks in the region around  $3000 \text{ cm}^{-1}$  should be assigned to the CH stretching bands of the oleic acid, with comparable intensity to the peaks at  $1555 \text{ cm}^{-1}$  and  $1466 \text{ cm}^{-1}$ . .... 131

Figure 6.12 Evidence of oleate covered on the surface. (a),(b) TEM images of as-prepared SrTiO<sub>3</sub> nanocuboids with oleate covered. (c),(d) TEM images of SrTiO<sub>3</sub> nanocuboids washed in ethanol. (e) TGA result shows the decrease of the mass of SrTiO<sub>3</sub> nanocuboids with the increases of temperature. .... 133

Figure 6.13 Mechanisms of the formation of different surface structures..... 135

Figure 7.1 Formation of surface islands on SrTiO<sub>3</sub> nanocuboids under electron beam irradiation. (a) A HREM image in [110] zone axis showing a flat (001) surface was observed initially, and was assigned to be the intrinsic surface. (b) With a ~2 nm converged electron probe applied on the nanocuboids for ~ 5s, an additional island can be observed clearly, as indicated by the yellow arrow. .... 139

Figure 7.2 Evolution of the SrTiO<sub>3</sub> (001) surface under electron beam irradiation. (a), (b) and (c) HREM images obtained by focusing the beam on the nanocuboids for ~ 3 s, 6 s, and 9 s,

respectively. In (a), beam induced additional layers start to form. In (c), TiO islands formed. The lattice spacing is $2.1\text{\AA}$ , as indicated by the yellow lines.....	141
Figure 7.3 Atomic resolution HREM images showing the interfacial structure of TiO and SrO-terminated SrTiO <sub>3</sub> . (a) An experimental HREM image taken at a small underfocus condition. (b) A cropped and magnified images of (a). (c) A cropped and magnified image of (b). (d) The simulated HREM image of (c). The simulation parameters are thickness=3 nm, defocus=-2 nm, Cs=-5 $\mu\text{m}$ , convergence angle = 0.3 mrad, focal spread = 3.5 nm, vibration = 0.4 $\text{\AA}$ in both x and y directions. No astigmatisms, coma, and sample tilt were considered in the simulation. The lattice spacing for SrTiO <sub>3</sub> and TiO are all set to 4.1 $\text{\AA}$ , thus no lattice strain can be seen in the simulation.....	142
Figure 7.4 EELS results on the islands and bulk regions of beam-damaged SrTiO <sub>3</sub> nanocuboids. (a) Illustration of the regions conducted EELS measurements. (b) and (c) are EELS results showing the difference of Sr N-edge, Ti L-edge, and O K-edge of the two regions as indicated in (a). .....	143
Figure 7.5 Comparison between TiO and Ti islands. (a) An experimental image showing TiO islands on the SrTiO <sub>3</sub> surfaces. (b) A Ti island beside a TiO island. (c) A series of simulated HREM images with thickness changes vertically from 1nm on top to 3 nm on the bottom and defocus changes horizontally from -10 nm on the left to 10 nm on the right. Each image represents a $3\times 3$ cell in the [100] zone axis. (d) The simulated HREM images with the same setting of (c) except using a bcc-Ti model. The simulation parameters other than the thickness and defocus are the same as the ones used in Fig. 7.3. ....	145
Figure 7.6 Illustration of the beam damage on a SrTiO <sub>3</sub> nanocuboid. The two yellow circles indicate the hole-drilling effect by a converged electron probe. ....	148
Figure 7.7 Mechanisms of the formation of Sr- and Ti-rich surface segregations under reduction and oxidation environment. ....	151
Figure 8.1 Atomic models of an artificial ( $3\times 3$ ) surface reconstruction on SrTiO <sub>3</sub> (111).....	154
Figure 8.2 Illustration of the imaging processing in plan-view HREM surface imaging. ....	156
Figure 8.3 Simulated HREM images of a single layer artificial SrTiO <sub>3</sub> (111)-( $3\times 3$ ). The atomic structure is shown in 8.1(a). ....	157



Figure 8.4 The HREM images obtained after the separation of the top and bottom surfaces. (a)-(d) Separated single surface images from the models with bulk thickness of 1 nm, 5 nm, 9 nm, and 13 nm. ....	158
Figure 8.5 Atomic resolution STEM images of Pt on SrTiO <sub>3</sub> nanocuboids with different terminations. Top: An ABF image shows the Winterbottom shapes of Pt with a cube-on-cube epitaxy on a SrTiO <sub>3</sub> nanocuboid with a SrO termination. Bottom: Top: A HAADF image shows the Winterbottom shapes of Pt with a rotated epitaxy direction on a SrTiO <sub>3</sub> nanocuboid with TiO <sub>2</sub> -rich surfaces. ....	160
Figure 8.6 Catalytic results of Pt on SrTiO <sub>3</sub> nanocuboids with different surface terminations. The Pt on SrO-terminated SrTiO <sub>3</sub> nanocuboids demonstrates higher activity in CO oxidation in an O-rich condition ([CO]: [O] =1: 40). ....	161

## List of Tables

Table 1 Some popular HREM simulation programs.....	50
Table 2 Assignment of IR bands from methanol adsorption on three ceria nanostructures at room temperature. The quantification of each methoxy species is shown in the parenthesis: red numbers represent theoretical value on the ideal surface while black numbers are from IR spectral fitting results (this table is reproduced from ref. [53], with permission from ACS Catal. 2012, 2, 2224–2234. Copyright 2012 American Chemical Society.).....	88

# 1. Introduction

## 1.1 Motivation

Understanding the structure-property relationship is the main task of materials science. In a variety of materials applications, the materials properties strongly depend on the surface structures. Understanding the surface structures is very important to understanding the properties and further developing the materials. These applications include catalysis [1-7], thin film technology [8-12], solid oxide fuel cells (SOFCs) [13-16], corrosion [17-19], chemical mechanical polishing (CMP) [20, 21], and others [22]. For example, in heterogeneous catalysis, the surfaces of catalysts adsorb the reactant gas molecules and facilitate the chemical reactions of the adsorbed molecules. Fig. 1.1 illustrates a realistic catalytic system in heterogeneous catalysis and a possible reaction mechanism. In thin film technology, the surface structures of substrate greatly impact the growth direction and other properties of the thin film [23]. In SOFCs, the surfaces of anode or cathode determine the reactivity of electrochemical reactions [14]. Materials' corrosion also happens on the surface initially. The surface of iron can easily be oxidized to form iron oxides, which are the composition of the iron rusts. For some rust-resistant metals, such as Al, dense oxide films can be formed on the surfaces as passivation layers to prevent further oxidation. In CMP, which is widely used in semiconductor foundry [21], it is found that different oxide slurries result in different polishing performances [20]. It is generally believed there is a strong binding between the surfaces of oxide slurries and the surfaces of the silicon wafers [20].

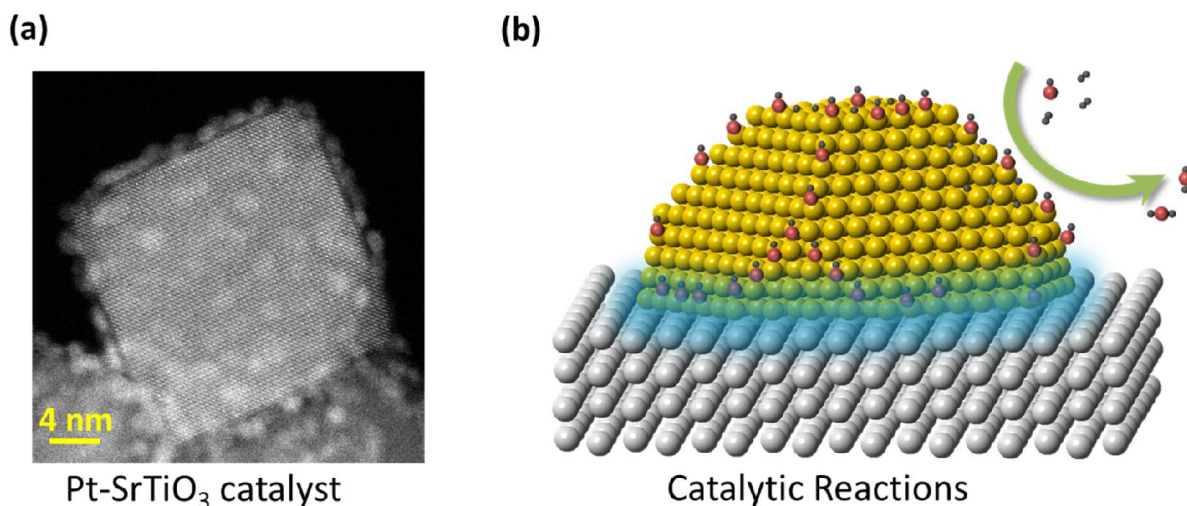


Figure 1.1 Illustration of catalysts and catalytic reactions in heterogeneous catalysis. (a) A HAADF image of Pt catalysts on a SrTiO<sub>3</sub> support. (b) Illustration of adsorption, desorption, catalytic reactions.

The definition of surface depends on the application areas. For a catalysis, thin film growth, and CMP, the surface usually refers to one or several atomic layers of the surface. Changes in the atomic surface structures can greatly impact their performances. For some other cases, such as SOFCs, a few nanometers to tens of nanometers of the surface region are important for the properties. The major focus of this study is on atomic scale surface structures. In particular, SrTiO<sub>3</sub> and CeO<sub>2</sub> are chosen as model systems for this study. SrTiO<sub>3</sub> is a popular material used as a substrate in thin film growth [24, 25]. High quality SrTiO<sub>3</sub> single crystal is relatively easy to obtain for growing high quality films. Recently, interesting properties, such as super conductivity, were discovered on the interface of SrTiO<sub>3</sub> and LaAlO<sub>3</sub> [9, 26]. The interface has potential applications in oxide electronics [27, 28]. Our group further utilizes SrTiO<sub>3</sub> nanocuboid as a substrate for the growth of Pt nanoparticles, which was proved to enhance the stability of the Pt

catalysts [29]. In this case, the SrTiO<sub>3</sub> nanocuboids act as catalytic supports. CeO<sub>2</sub> is a material widely used in catalysis [5, 30-32], SOFCs [15, 33, 34], and CMP [21]. It is believed the surface of CeO<sub>2</sub> can provide its lattice O to reactants and be re-oxidized by gas phase O<sub>2</sub> [35]. As a result, the surface of CeO<sub>2</sub> is active in oxidative reactions. It is worth noting that nanoparticles are used in catalysis due to their large surface area, as the surface area is usually proportional to the reactivity. Therefore, both the surface structures of nanoparticles and single crystal are important.

The majority of the previous atomic surface structure studies are on the single crystals [36-39]. The atomic structural studies on the nanoparticles are rare [40-42]. This is usually referred to as the materials' gap in surface science and catalysis. The single crystal surfaces are simplified systems to real catalysts. Sometimes the studies on single crystal surfaces provide insightful information on surfaces of catalysts as well as the reaction mechanisms [43, 44]. However, for some other cases, the surface structures of single crystals may not be present in real catalysts. The sample preparations of single crystals and nanoparticles are very different. For example, a variety of surface reconstructions have been discovered on the single crystals under high temperature annealing [45-47]. The calcination temperature for preparation of catalysts is usually not as high [48-50]. To bridge the materials' gap, both the atomic surface structures of single crystals and nanoparticles are covered in this study. In particular, the nanoparticles used in this study are the ones with well-defined shapes, which allow one to determine the factors that control the surfaces and the corresponding catalytic properties.

## **1.2 Possible Surface Structures**

Mathematically, there are infinite possible surface structures can be created. Physical or chemical driving forces make some surface structures present and others not. Generally, the atomic surface

structure can be considered as intrinsic or extrinsic. The formation of intrinsic surface structures is due to intrinsic stability and kinetic factors. If a surface adsorbs external species such as gas molecules, the surface structures become extrinsic. There is no exact intrinsic surface structure, as surface is always interacting with external environment by chemisorption or physisorption of other species. There are residual gas molecules even in ultra-high vacuum (UHV) environment. The physisorption is usually weak that adsorbed species can be easily removed. The chemisorbed species can rather tightly bond to the surface, which can impact the surface structure and the corresponding properties. As a result, a careful surface structure analysis should always consider the possible adsorption. Practically, the specimen should be kept as clean as possible, which helps to exclude some adsorptions.

For metal oxide surfaces, there are several often observed atomic surface phenomena. A simple binary oxide sometimes can have several surface terminations. For example, an O layer termination or a metal layer termination, as shown in Fig. 1.2. A surface can be formed by truncating a bulk crystal or end of synthesis. The different surface terminations usually undergo surface relaxation or form a surface reconstruction with a drastically different surface structure from the bulk truncated termination. The surface structures are as a result of both thermodynamics and kinetics. The surface tends to form the structures with the lowest energy. However, if a structure is very different from the initial as-prepared surface, there is an activation energy associated with the transformation of the as-prepared surface to a surface with lower surface energy.

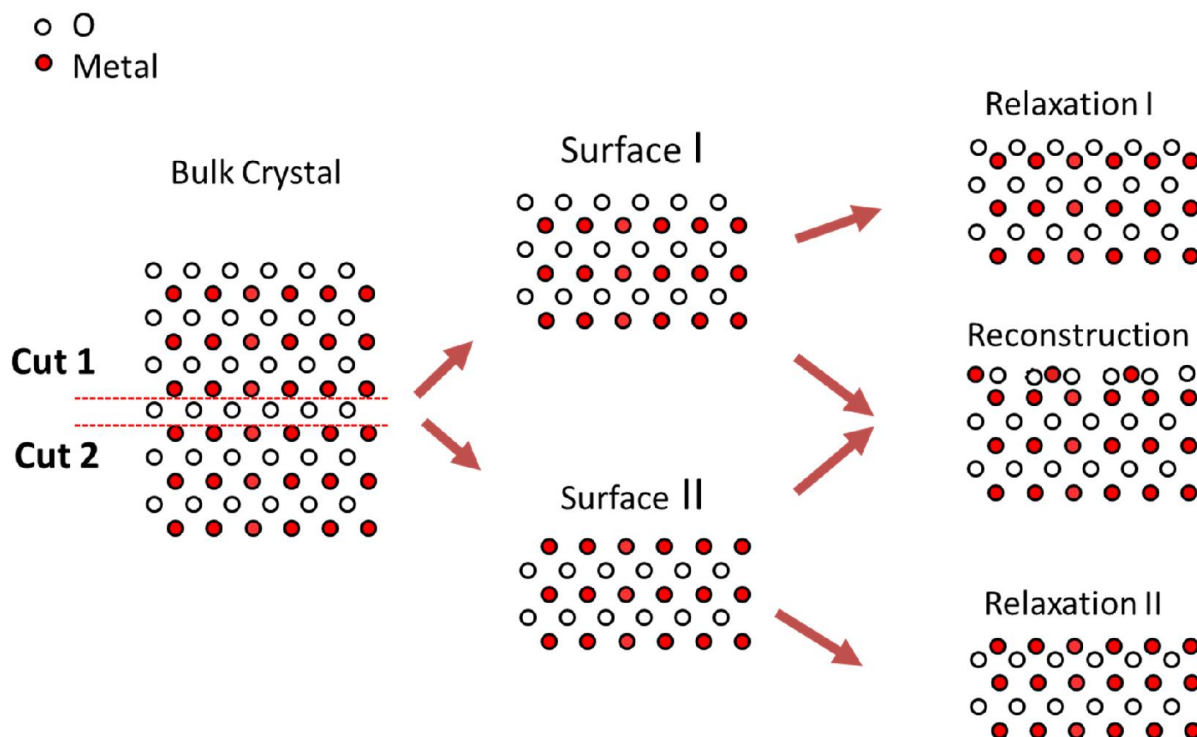


Figure 1.2 Some possible surface structures of oxides.

Moreover, it is always reasonable to consider the O vapor pressure for oxide surfaces. O vapor pressure is correlated with the O chemical potential. The chemical potential is part of the thermodynamic Gibbs free energy of the surface. A low energy O-terminated surface structure can have O vacancies when the surrounding O vapor pressure is low. On the other hand, a metal-terminated surface starts to adsorb O if the O vapor pressure is high enough. Usually it is only important to consider the region of O vapor pressure that is similar to in the real applications.

### 1.3 Terminology of Surface Reconstructions

Usually, Wood's notation is used to represent surface reconstructions, as shown in Fig. 1.3. The X denotes the name of crystal, for example, SrTiO<sub>3</sub>. The (hkl) denotes the Miller index of the

surface of interest. The  $(m \times n)$  denotes the surface periodicity with respect to the bulk truncated surface unit cell. For some cases, the reconstructions have a rotation with respect to the bulk registry, which is denoted by  $R\phi$ . Fig. 1.3 shows a surface reconstruction with a  $45^\circ$  rotated  $(\sqrt{2} \times \sqrt{2})$  periodicity. If the reconstruction is on  $\text{SrTiO}_3$  (001), the reconstruction can be denoted by  $\text{SrTiO}_3(001)-(\sqrt{2} \times \sqrt{2})R45^\circ$ . For simplicity, the crystal name and Miller index of surface are often neglected in this study.

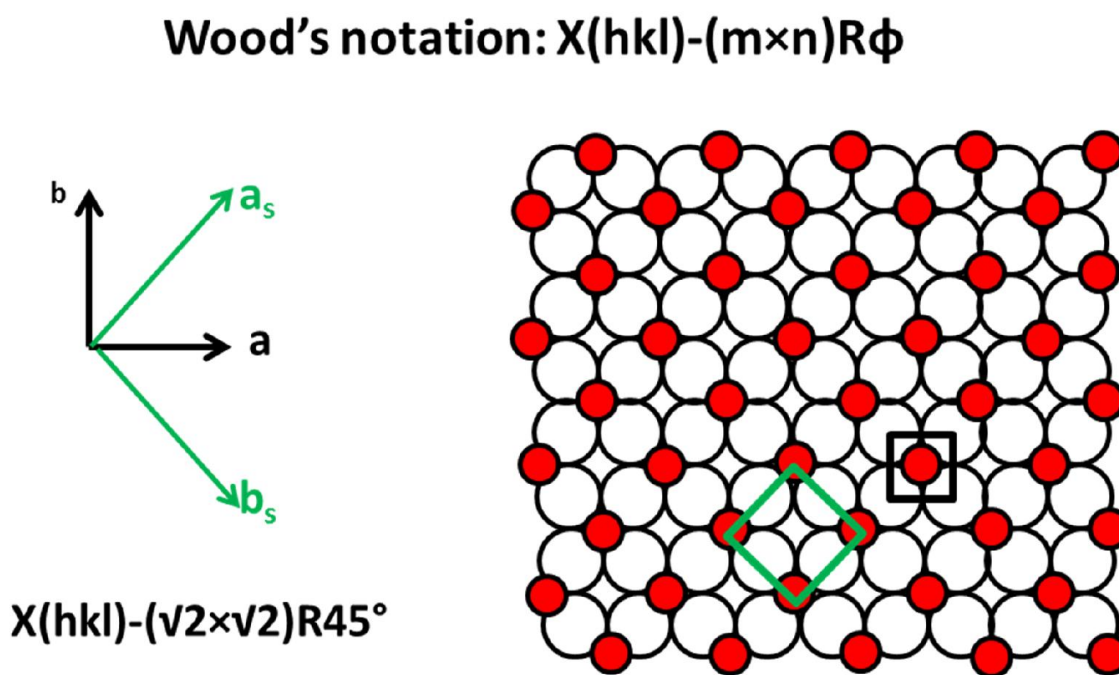


Figure 1.3 Illustration of Wood's notation for surface reconstructions. Left: unit vectors of the surface structure and bulk structure. Right: a  $(\sqrt{2} \times \sqrt{2})$  surface reconstruction with the surface unit cell marked in green and bulk in black.

## 1.4 Organization

This dissertation is presented as follows: chapter 2 illustrates the experimental and theoretical tools used in this work. Chapter 3 provides a brief overview of the surface reconstructions of

SrTiO<sub>3</sub>(001), which is in the form of single crystals. Furthermore, a (2×2) surface reconstruction of the SrTiO<sub>3</sub> (001) was investigated by STM and DFT. A possible structural solution is proposed. Chapters 4 to 7 focus on the atomic surface structures of nanoparticles. Chapter 4 provides the atomic surface structures of CeO<sub>2</sub> nanoparticles while chapter 5 provides the atomic surface structures of reduced Ce<sub>2</sub>O<sub>3</sub> nanoparticles. The atomic surface structures of SrTiO<sub>3</sub> nanocuboids are presented in Chapter 6. The atomic surface structures of SrTiO<sub>3</sub> under strong electron beam are investigated in Chapter 7. Chapter 8 illustrates the preliminary results of two ongoing projects. One is on the catalytic properties of nanoparticles with different atomic surface structures; the other is on the testing of plan-view HREM imaging for surface analysis. The last part of Chapter 8 provides some ideas for future studies.



## 2. Methods

### 2.1 Introduction

This chapter introduces the characterization techniques for the surface studies. Conventional surface sensitive techniques such as scanning tunneling microscopy (STM), X-ray photoemission spectroscopy (XPS), and Auger electron spectroscopy (AES) will be briefly described. These techniques can provide very useful information such as surface periodicity, symmetry, and chemical compositions. For ordered atomic structures of complex oxides, such as surface reconstructions of SrTiO<sub>3</sub>, the transmission electron diffraction (TED) together with direct methods and density functional theory (DFT) can usually give a more reliable solution. The above mentioned experimental techniques are well-established for solving the surface structures of single crystals, but they are not designed to solve the surface structures of nanoparticles. In the latter case, operating TEM in high resolution electron microscopy (HREM) or scanning transmission electron microscopy (STEM) mode can provide atomic resolution structural information on each nanoparticle, including the surface.

In catalysis, spectroscopic studies with molecular probes are often used to characterize atomic surface structures of nanoparticles. For instance, methanol or CO molecules are intentionally introduced to nanoparticles and the subsequent nanoparticles are characterized using infrared (IR) spectroscopy or others [51-53]. As the molecules usually cannot penetrate into the nanoparticle, the spectroscopic signal is also surface sensitive. These techniques are less well-known in UHV surface science community as the surface area of the single crystals is not large enough to generate a reasonably strong signal in the spectroscopy. The techniques are ideal for studying the

surface chemistry of nanoparticles as they have a much larger surface area with the same amount of material. However, if the nanoparticles have random shapes, the signals in the spectroscopic studies can be from different facets, and low-coordinated sites such as corners and edges. The spectroscopic studies on the nanoparticles with well-defined shapes are able to provide atomic surface structural information on a large scale, which can be used together with local characterization techniques such as HREM to understand the surface structures better.

## **2.2 Experimental**

### **2.2.1 Electron-specimen interaction and TEM basics**

The wealth of information TEM can provide is due to the different electron-specimen interactions and versatility of TEM operation methods. Fig. 2.1(a) shows a cross-section view of a simplified TEM model. Changing the convergence of the illuminating beam and using different apertures or detectors can lead to different operating modes for specific applications. Fig. 2.1(b) shows different types of signals generated by a high energy electron beam (usually 80-300 KeV) passing through a thin specimen. Images are formed by the detection of transmitted beams. The objective lens aperture can be used to selectively choose the direct beam to form images with, which are known as bright field (BF) images. If the scattered electrons are chosen, the corresponding images are dark field (DF) images. The BF and DF images sometimes are very useful to deliberately enhance or suppress signals of a particular material, crystal plane, or defects. Analyzing the energy loss of the inelastically scattered beam can help to determine the elemental composition and bonding configurations of materials, which is the principle of electron energy loss spectroscopy (EELS). Above the specimen, the characteristic X-ray signals can be utilized for Energy-dispersive X-ray spectroscopy (EDS) analysis. Collecting the signals

of the secondary electrons and backscattered electrons can form surface-sensitive SEM-like images.

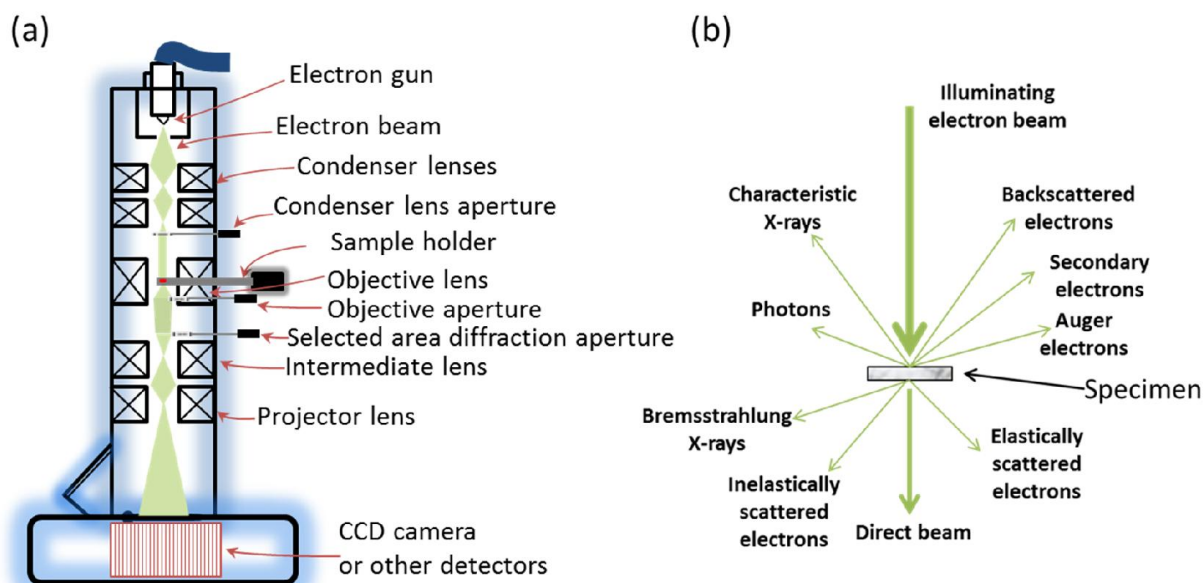


Figure 2.1 Schematic view of a TEM setup and the electron-specimen interaction.

### 2.2.2 HREM and STEM

HREM and STEM are the most often used operation modes for atomic resolution imaging in TEM. Fig. 1-3 shows a comparison between STEM mode and HREM mode. In STEM mode, the electron beam converges to a probe (typically less than 1nm) which scans across the sample, while HREM makes use of static parallel beam imaging. In STEM mode, after the electrons exit the sample, the scattered beams and direct beam can be collected in the diffraction plane by annular detectors. The analog signal on each detector is digitalized and displayed on the computer screen. The electrons collected by the annular dark field detectors (ADF) can form images in which the contrast is directly related to the atomic number of the materials if the

collection angle is high enough. Thus the ADF images are often called  $Z$ -contrast images, although this is a dangerous term as it can be quite misleading [54]. Usually the larger the atomic number  $Z$  is, the brighter the material appears on the  $Z$ -contrast ADF images while the vacuum is displayed as a black background. The  $Z$ -dependency can be tuned by the collection angle of annular detectors. For example, increasing the collection angle of ADF detectors increases the  $Z$ -dependency of the image contrast. The direct beam and scattered beams within a very small angle can be collected by the bright field (BF) detector. Usually the collection angle ( $\theta$ ) for BF detector is less than 10 mrad. A detector with collection angle larger than 50 mrad is considered to be a high angle ADF (HAADF) detector. For HAADF images, the contrast is proportional to  $Z^n$  ( $n$  can be  $\sim 1.7$ ) [55-57]. By tuning the collection angle, it is possible to obtain images with contrast linear to the  $Z$ . If a beam stopper is applied on the BF detector to block the direct electrons, the resulting images are called annular bright field (ABF) images [58]. Typically in HREM mode, all of the signals in the diffraction plane pass through additional TEM lenses and form a HREM image on a CCD camera. Selectively allowing the direct or diffracted spots in the diffraction plane to pass through the remaining lens optics can form BF or DF images respectively. The lattice fringes in HREM images are a result of the interference among the direct and diffracted spots. In STEM, as the collection angle of the BF detector is small enough that the beam can be considered a parallel beam, BF-STEM and HREM have the reciprocity relationship and thus the mechanisms of image contrast are identical so long as inelastic scattering can be ignored [59].

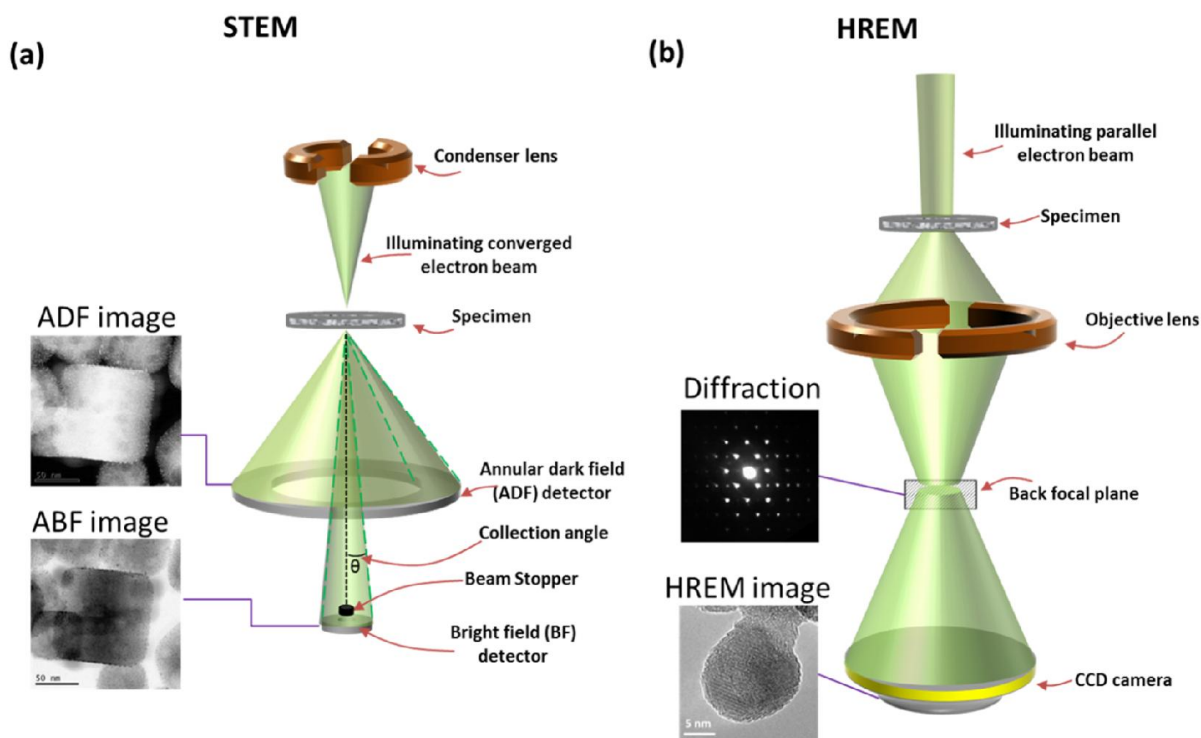


Figure 2.2 Schematic view of the optics in HREM and STEM.

### 2.2.3 TEM for surfaces

Both the plan-view and profile-view techniques in TEM can be used to characterize atomic surface structures of materials. In this study, the most often used techniques are profile-view HREM and STEM. Fig. 2.3 shows the schematic comparison between the plan-view and profile-view imaging. The profile-view imaging techniques are very useful in observing the projection of a 2D surface. HREM and STEM can also be used in plan-view mode. However, the interpretation of the surface contrast is more complicated, which involves deconvolution of the overlapped signals from the top surface, bulk, and bottom surface. Probably the most important plan-view technique for the study of atomic surface structure is electron diffraction. A number of

the atomic structure of the SrTiO<sub>3</sub> surface reconstructions have been solved by plan-view diffraction. However, for the systems without well-defined reconstructions, the surface diffraction spots cannot be separated from the bulk spots. As a result, the techniques are not as useful in solving the surface structures such as bulk truncated layers, surfaces with disordered defects, surface relaxations, and small scale surface reconstructions. In contrast, these surface features can be clearly observed by atomic resolution HREM and STEM.

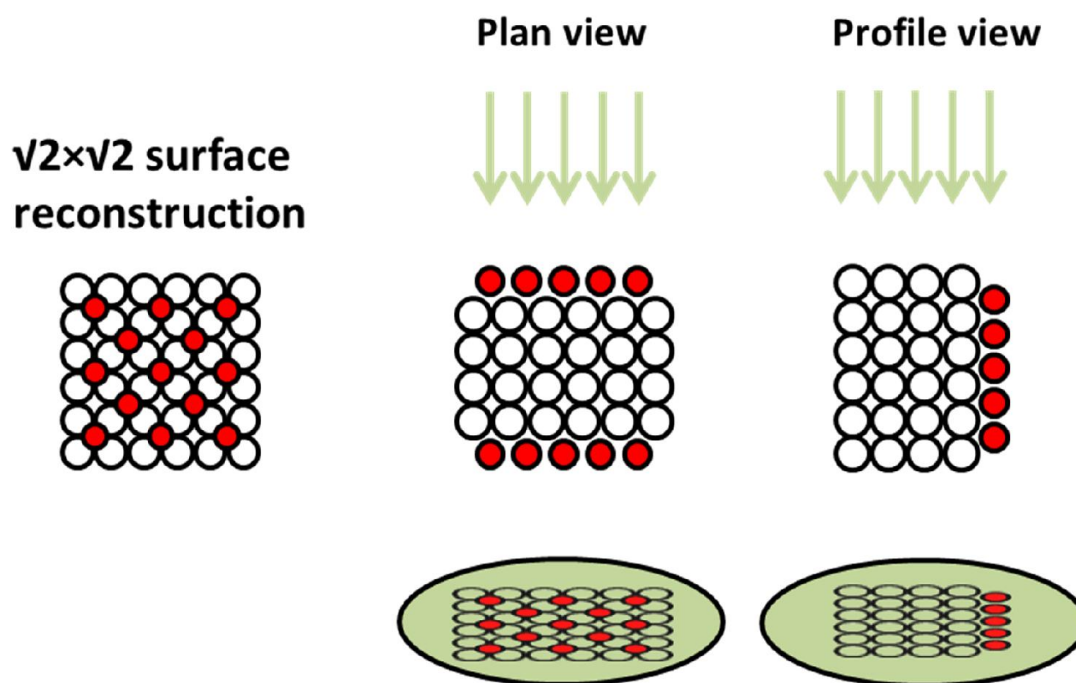


Figure 2.3 Illustration of plan-view and profile-view surface imaging.

#### 2.2.4 TED

In TEM, the transmitted beam includes the diffracted beam and direct beam. By changing the strength of the intermediate lens, a diffraction pattern can be recorded. The electron diffraction is similar to X-ray diffraction (XRD). However, there are some important differences. Electrons

usually interact with the materials more significantly than the electron diffraction can undergo multiple reflections (dynamical diffraction) instead of a single reflection (kinematical diffraction) in XRD. As a result, the forbidden reflections determined by the lattice of crystal can show up in electron diffraction. Moreover, the well-established structure retrieval methods require the correct intensities of the kinematical diffraction spots. The structural solutions based on electron diffraction are much more difficult to obtain. A solution simply using the retrieval methods as used in XRD may not be correct. Therefore, the surface sensitive electron diffraction techniques such as Low-energy electron diffraction (LEED) and Reflection high-energy electron diffraction (RHEED) are often used to identify the surface periodicity, but seldom used to solve a surface structure.

In TED, the dynamical diffraction can be reduced by tilting the electron beam or crystal. If the crystal is tilted  $\sim 30$  mrad off from the zone axis, the dynamical effect is reduced significantly. Another benefit of tilting the crystal is the relative surface signal in the diffraction pattern is enhanced, as shown in Fig. 2.4. Due to the finite size of the TEM crystal, the diffraction spots have a certain dimension in the reciprocal space. The dimension of the spots has an inverse relation to the size of a feature in real space. As surface reconstructions usually are only one to several layers thick, the diffraction spots are very long rods (the beam direction), which is much longer than the reciprocal rods (rel-rods) of the bulk crystal. As the crystal is tilted off the zone axis, the Ewald's sphere has a larger chance to truncate the surface rel-rods than the bulk rel-rods. As a result, the bulk signal is weakened significantly if a crystal is not in a zone axis while the surface signal is only slightly changed. The relative surface signal is enhanced.

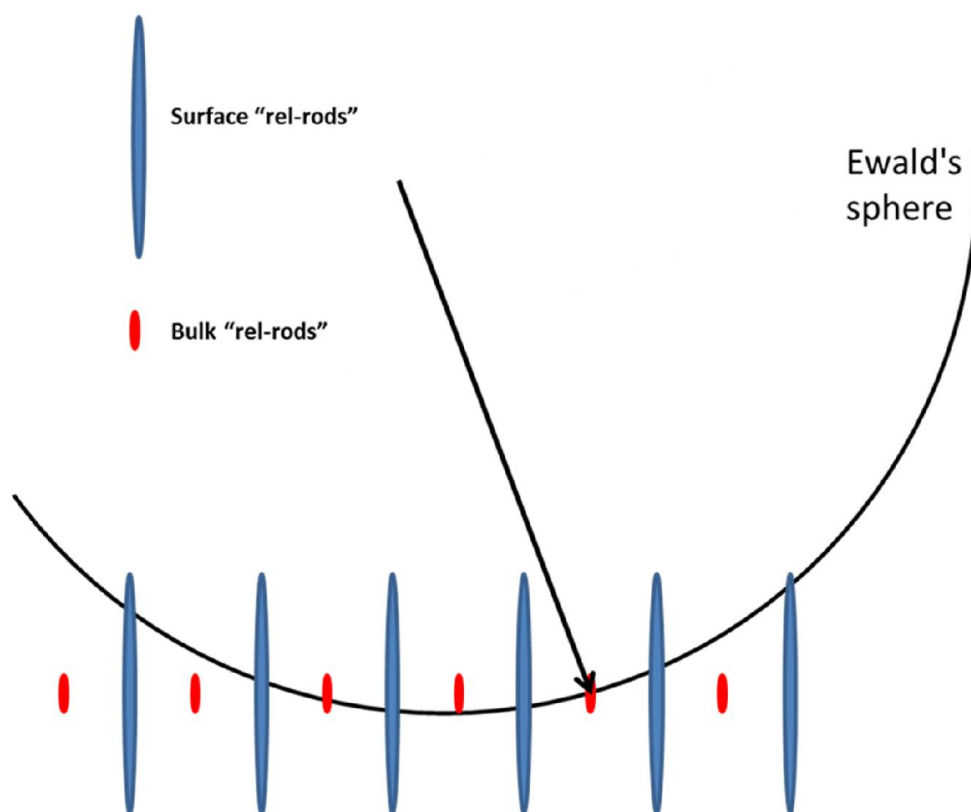


Figure 2.4 Illustration of electron diffraction for surface structures in a TEM. A diffraction spot can be observed when the Ewald's sphere truncates a rel-rod.

### 2.2.5 EELS

The electrons can undergo inelastic scattering in the specimen. The energy loss can be detected by an EELS spectrometer. The working principle of an EELS spectrometer is some magnetic prisms which can separate the transmitted electrons with different energies. Based on the amount of energy loss, there are generally a zero-loss region (0 to a few eV), a low-loss region (5 – 50 eV), and a core-loss region in EELS ( $> 50$  eV). The zero-loss region is composed of elastically scattered electrons. The low loss region contains the transmitted electrons which have been interacting with weakly bonded outer shell electrons of materials [60]. An example of the low



loss region is the plasmon peaks, which are due to the resonance of the TEM beam electrons and the valance electrons of materials. The zero-loss region contains little analytical information about the specimen material. However, it is often used to measure the energy spread of TEM instruments. The relative ratio of the low-loss and zero loss regions can be used to detect the thickness of the specimen. By filtering the low-loss and core-loss electrons and only allowing the zero loss electrons to arrive at an image recording media, an energy filtered image can be formed. The edges in the core-loss region are due to the interaction of the beam electrons with the inner shell electrons of materials. The beam electrons transfer a certain amount of energy to the core shell electrons of the material to induce ionization. As the ionization energy is usually element specific, the core-loss ionization edges are characteristic signals of ejections. In addition, the fingerprint of the ionization edges includes the electron loss near-edge structure (ELNES) and extended energy-loss fine structure (EELFES), which can be used to identify the oxidation states and coordination environment of elements [61].

Compared to EDS, EELS can have a higher spatial resolution and provide additional analytical information (such as the coordination). The negative aspects of EELS are the low signal of thick samples and the insensitivity of heavy elements.

### **2.2.6 IR Spectroscopy**

Unlike the electron based characterization techniques in TEM, the photon energy associated with the infrared (IR) is not large enough to excite electrons from the shells of atoms. However, infrared can induce the vibrational excitations of the covalent bonded atoms or groups. The covalent bonds can be analogous to the springs between atoms. Each structure can resonantly absorb the energy from the infrared beam. Owing to the resonant adsorption, the vibration

excitations are characteristic signals which can be used to detect the bonding of the molecules. In this study, the vibrational excitations are from the adsorbed molecules on the solid surface. IR spectroscopy measures the light absorbance as a function of wavelength. Usually in laboratory instruments, the IR spectroscopy measures the light absorbance in reciprocal space, which is referred to as Fourier transform infrared (FT-IR) spectroscopy. In FT-IR, the light absorbance is measured as a function of wavenumber ( $\text{cm}^{-1}$ ). For some common bonding structures, the C-H adsorption band is located at  $\sim 3000 \text{ cm}^{-1}$ ,  $\text{C}=\text{C}$  and  $\text{C}\equiv\text{N}$  are located around  $\sim 2200 \text{ cm}^{-1}$ , and  $\text{C}=\text{O}$  is located  $\sim 1500 \text{ cm}^{-1}$  to  $1800 \text{ cm}^{-1}$ . In addition, the bond strength of the same adsorption mode correlates to the frequency. A higher frequency usually results in higher bond strength (Badger's rule). For example, if a  $\text{C}\equiv\text{C}$  adsorption frequency is increased from  $2200 \text{ cm}^{-1}$  to  $2250 \text{ cm}^{-1}$ , the  $\text{C}\equiv\text{C}$  bonding is stronger. This can be qualitatively understood by using the spring model between the atoms, as the spring constant increases (the strength of bonding), the frequency increases.

### **2.2.7 AES and XPS**

AES is a surface sensitive technique used to analyze the surface chemical composition. All the AES results in this study were performed by Dr. Martin Castell's group at Oxford University. When an electron beam irradiates a specimen, secondary electrons, backscattering electrons, and Auger electrons can emit from the surface. The signals can all be used to analyze materials surface, but in a different scale. Usually the escape depth of Auger electrons is within a few nm surface region; hence it is very surface sensitive. The secondary electrons are generated within a  $5 \sim 50 \text{ nm}$  surface region, while the backscattered electrons are generated within several hundred

nm. The secondary and backscattered electrons are used to form SEM images. The excitation volume of X-ray can reach as deep as of a few  $\mu\text{m}$ , which is used as EDS signals.

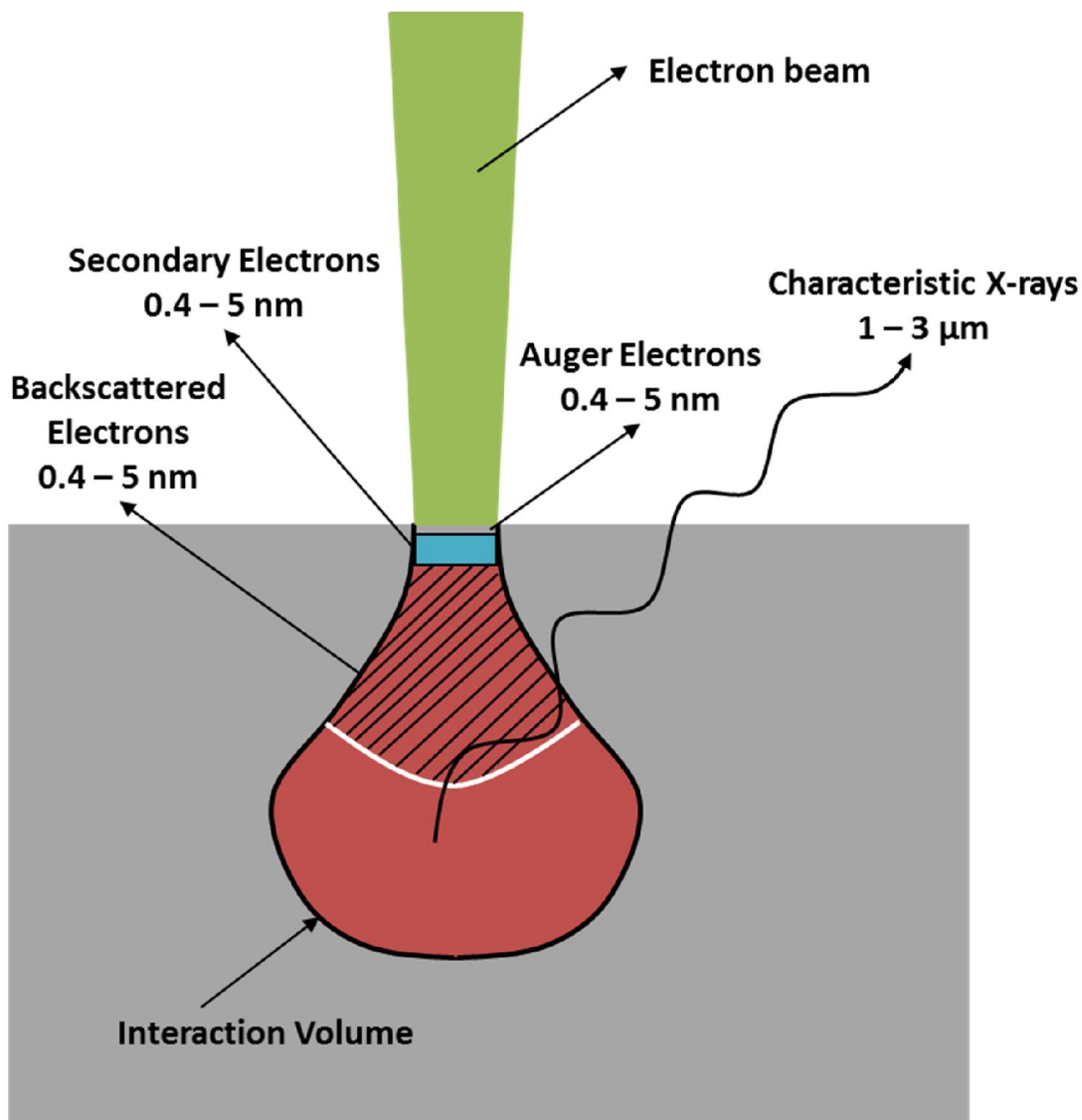


Figure 2.5 Schematic view of the interaction volume and the escape depths of different signals when an electron beam irradiates a specimen.

XPS utilizes the emitted electrons generated by the high energy X-ray irradiation on materials' surfaces. Usually XPS is plotted with the change of kinetic energy while XPS is plotted with

respect to the binding energy. However, intrinsically both XPS and AES measure the characteristic energies of elements. AES and XPS have similar surface sensitivity. XPS has an advantage over AES that it can also measure the chemical state in addition to identifying elements. Measuring chemical states using AES is not as straightforward. On the other hand, as secondary electrons and other signals are generated together with Auger electrons, AES can be coupled with SEM to obtain morphological information of surfaces.

### **2.2.8 Inductively coupled plasma atomic emission spectroscopy**

Inductively coupled plasma atomic emission spectroscopy (ICP-AES) is an analytical chemistry technique which can be used to precisely obtain the compositions of the metal ions in solution. ICP is used in this study to measure the loading of Pt in the SrTiO<sub>3</sub> supported Pt systems. ICP utilizes plasma to excite the electrons of metal ions. The excited electron can transit to ground state by emitting a photon with a characteristic energy. The characteristic energy is measured to identify elements. Experimentally, a solid sample should be dissolved completely with the concentrations of each ions to be 0.2 ~ 70 ppm. Usually the oxide nanoparticles should be dissolved in aqua regia or HF. The concentrations of elements in the sample solution are calculated based on fitting to the spectra of the standards. The error associated in ICP is less than 10%.

## **2.3 Theoretical**

### **2.3.1 DFT**

The modern physics is based on quantum mechanics and the theory of relativity. In quantum mechanics, the Schrödinger equation is the analogue of Newton's law in classical mechanics.

Mathematical prediction of a system's motion or property requires solving the Schrödinger equation in quantum mechanics. Eq. 1 shows the time-independent Schrödinger equation,

$$\hat{H}\phi_m(\vec{r}) = \varepsilon_m\phi_m(\vec{r}) \quad \text{Equ. 1}$$

where  $\hat{H}$  is the Hamiltonian operator and  $\Psi$  is the wave function. The  $\hat{H}$  includes partial derivative terms and is the operator for the kinetic energy and the Coulombic interactions between the charged particles. Solving Eq. 1 results in eigenvalues and eigenstates of energy. As the Schrödinger equation is a partial differential equation, solving it requires much more effort than Newton's equation. Analytical solution for simple systems such as a hydrogen atom is possible. For other more complicated systems, such as a solid material with many atoms and electrons, analytically solving the many-body Schrödinger's equations is a formidable task. Without the right approaches and approximations, even numerical solutions are extremely difficult to obtain. DFT is created to solve such many-body quantum mechanics problem.

The theorems proposed by Hohenberg and Kohn in 1964 established the basis of DFT [62]. The basic idea is that there is a one-to-one correspondence between the electron charge density and the expectation value of any observable property in the ground state. As the charge density can be represented by its eigenvalues and eigenstates, the other ground state observable properties such as energy are functionals of the ground state density. This is where the name DFT comes from. Kohn and Sham [63] further derived the many-body Schrodinger equation to have the same form as a single-body Schrodinger equation, as shown in Equ. 2. The interactions between the charged particles (electrons and nuclei) except the Coulomb repulsion between electrons

(called the Hartree term) are included in an exchange-correlation functional ( $V_{xc}$ ) term. The local density approximation (LDA) is the first overwhelmingly successful approach used to calculate the exchange-correlation functional, which is only dependent on the local electron density. The remaining problem is a self-consistency problem: the Hamiltonian operator is unknown since both the Hartree and  $V_{xc}$  terms depend on the electron density  $\rho$ . A guessed  $\rho$  can initially be used to calculate the Hartree and  $V_{xc}$  terms (using LDA or other functionals). Solving the Schrodinger's equation can obtain a calculated density ( $\rho_n$ ). If the difference between  $\rho$  and  $\rho_n$  is negligible, then the guessed density is a self-consistent one. Otherwise a new density is constructed based on the  $\rho_n$ . This self-consistent density could be obtained after some interactions with the help of a computer.

$$\left( -\frac{\hbar^2}{2m_e} \nabla_m^2 + \frac{e^2}{4\pi\epsilon_0} \int \frac{\rho(\vec{r}')}{|\vec{r} - \vec{r}'|} d\vec{r}' + V_{xc} + V_{ext} \right) \phi_m(\vec{r}) = \epsilon_m \phi_m(\vec{r}) \quad \text{Equ. 2}$$

The recent development of DFT theory focuses on the exchange-correlation functional and the numerical approaches. The generalized gradient approximation (GGA) depends on both the local density and its gradient. There are different versions of GGA. The PBE functional is one of the most popular GGA versions [64], and is believed to be more accurate than the original LDA in calculating some properties of materials. The authors of the PBE functional (Perdew et al.) recently developed a revised functional for PBE, which is PBE for solid and surfaces (PBEsol) in order to improve the lattice parameter and surface energy estimation of DFT [65]. DFT usually works well for metals but not for the transition metal oxides and insulators. In fact, DFT often fails for the predictions of strong correlated systems, which is due to the d and f electrons of the materials coupling too strongly with the 2p states of oxygen. A solution is adding a fraction of

exact-exchange for relevant orbitals using the Hartree-Fock (HF) method. The original DFT functional becomes a hybrid functional. For some calculations in this study, the hybrid functional PBEsol0, which is a combination of PBEsol and HF equations, is used. The exact fraction varies from system to system. For the calculation of SrTiO<sub>3</sub>, the fraction 0.5 is used for the d electrons of TiO<sub>2</sub>. The value is determined by fitting the DFT energies to the experimental heat of formations of Ti oxides.

In this study, the DFT calculations were performed using WIEN2k software [66], which includes a full potential all-electron scheme as well as relativistic effects. In WIEN2k, the expansion is performed using the augmented plane waves + local orbitals (APW+lo) method. In this method, space is partitioned into the area near the nuclei and the area between them. The near-nuclei area is called the muffin-tin region and the outer area is the interstitial region. In the muffin tin region, the basis set consists of spherical harmonics multiplied by radial functions, with additional local orbital terms added to increase flexibility. In the interstitial region, the basis set consists of plane waves. These basis sets are forced to satisfy some boundary conditions at the end of the muffin tin region so as to make the solution physically reasonable. The accuracy of the calculation is set manually by deciding the  $R_{\min}K_{\alpha}^{\max}$ , which controls the truncation of basis sets. A calculation will be accurate enough by using a relative large  $R_{\min}K_{\alpha}^{\max}$ .

DFT calculation is often used in this study. It is used to calculate the density of states (DOS), which can be further used to simulate STM images. A number of surface structures are relaxed by DFT to obtain the locally lowest energy configurations and the associated surface energy. The difference in the normalized surface energy between each structure indicates the

relative stability of them. DFT can be utilized more to understand other experimental results, such to simulate EELS and XPS, although that is not explored in this study.

### 2.3.2 Bond Valence Sum

DFT is quantitative and based on the first principles in physics. Performing DFT calculation is time-consuming and sometimes not straightforward. In contrast, Bond valence sum (BVS) is a convenient tool often used to test the stability of chemical bonding. BVS is empirical and performing BVS calculation is fast. BVS (V) sums individual bond valance ( $v_i$ ) surrounding an atom as in Equ. 3

$$V = \sum(v_i) \quad \text{Equ. 3}$$

The individual bond valance is calculated by Equ. 4.

$$v_i = \exp\left(\frac{R_0 - R_i}{b}\right) \quad \text{Equ. 4}$$

where  $b$  is an empirical constant and is usually set to 0.37 Å,  $R_i$  is the observed bond length and  $R_0$  is a parameterized length for the particular bonding. A reasonable structure should have all the atoms with their BVS similar to their ideal valence states. For example, a BVS for a  $\text{Sr}^{2+}$  in a proposed model should be close to 2. If the BVS shows 1.1, which is very different from 2, the proposed model should be revisited.

BVS are often used to check the bulk structures or organic molecules in organic and inorganic chemistry. Our group performed comprehensive BVS study on the surface structures of  $\text{SrTiO}_3$ ,



and found that the prediction of BVS and DFT are consistent [67]. This indicates BVS is also valid for surface structures. Practically, our group often uses BVS to pre-relax a surface structure before performing DFT calculation. In addition, BVS is used to confirm the validity of DFT relaxed surface structures and compare the relative stabilities of different surface structures.

### **2.3.3 STM and STM simulation**

STM was invented by Gerd Binnig and Heinrich Rohrer in 1981 at IBM Zürich. The principle of STM is the tunneling effect in quantum mechanics, which indicates the electrons can tunnel through a finite potential with a certain nonzero probability. In other words, there can be a tunneling current between two objects without a conducting layer between each other. In STM, a sharp tip is rastered across a surface with a bias voltage applied between the specimen and tip. Owing to the quantum tunneling effect, there is a tunneling current between the specimen and tip. The tunneling current (or tip height) is monitored at every position. The STM can be operated at constant current and constant height modes. Operating the STM in the constant current mode is usually safer as the distance between the tip and surface can be automatically adjusted to avoid crashing. As the tunneling current is very sensitive to the surface electronic structures and morphology, STM is very surface sensitive. The lateral resolution can reach  $1\text{Å}$  while the depth resolution can reach  $0.1\text{Å}$ .

The intrinsic contrast on the STM images is the tunneling current between the tip and specimen. The early Bardeen tunneling theory [68] implies that the tunneling current is directly related to the density of electron states in both the sample and the STM tip. The general idea used by Bardeen is to first solve the Schrodinger equations of the tip and sample independently

and then use Fermi golden rule to calculate the overlap of the wavefunctions generated by the two free systems. The resulting solution for the tunneling current is

$$I = \frac{4\pi e}{\hbar} \int_0^{eV} \rho_S(E_F - eV + \varepsilon) \rho_T(E_F + \varepsilon) |M|^2 d\varepsilon \quad \text{Equ. 5}$$

where  $\rho_S$ ,  $\rho_T$  are the density of states of the sample and the tip, respectively.  $M$  is the tunneling matrix element, which is assumed not to depend significantly on the bias voltage. While the density of states of the sample can be obtained by ab-initio methods such as DFT, the one for the STM tip is generally unknown. Tersoff and Hamann further assume that the apex atom on the STM tip only has the s-wave orbitals [69]. Then the tunneling can be represented as

$$I_T(S \rightarrow T) \sim \sum_k |\varphi_k(\vec{R}_0)|^2 = \int_{E_F}^{E_F + eV_b} \rho(\vec{R}_0, \varepsilon) d\varepsilon \quad \text{Equ. 6}$$

Equ. 6 indicates the tunneling current approximately only depends on the density of states at the center of tip apex. The Tersoff-Hamann approximation is generally valid when the bias voltage is small ( $<100\text{meV}$ ). But for the  $\text{SrTiO}_3$  surface, the STM images were obtained at a high voltage (around 1 V). Therefore, a modification on the Tersoff-Hamann approximation [70] was made by adding a weighting term since the barrier is higher for lower energy states; although this is more rigorous the effect is small. Moreover, a blurring effect via a radial convolution feature was also applied to account for tip-size and thermal effects. DFT codes such as WIEN2k can readily calculate the surface local density of states (LDOS) over a range of energy levels. Therefore, DFT calculations can be used to simulate STM images and identify which surface model is more similar to the experimental images.

### 2.3.4 Introduction to HREM imaging theory

The contrast in HREM image can arise from both interference pattern of the electron beam with the sample and electron beam with the TEM lens. Thus the spots (either bright or black spots) can be real or just artifacts. A general process of a HREM image formation includes 5 steps: (1) a parallel electron beam illuminates on the sample, (2) the electrons interact with the sample, (3) the electrons leave the sample (often called exit wave), (4) the electrons pass through the TEM lens optics, and (5) the electron wave form a HREM image on a CCD camera or other recording media. The final intensity in a HREM image is the modulus square of the arriving final electron wave function  $\varphi(r)$ :

$$I = |\varphi(r)|^2 \quad \text{Equ. 7}$$

In the simplest approximation, called linear imaging theory, the electron wave function  $\varphi(r)$  is a convolution of the exit wave function ( $\varphi_e$ ) and a point spread function (P):

$$\varphi(r) = \varphi_e \otimes P \quad \text{Equ. 8}$$

where P contains the effects caused by all the TEM optics. P is close to a delta function in a perfect microscope. Thus the resulting HREM images are exit wave images. The fringe patterns in such images are purely due to the interference between the sample and electron beam. If the sample is tilted to a low-index zone, there is close to a one-to-one correspondence of the atom column positions and the spots in such images. The perfect microscope for HREM does not exist. However, within the resolution of concern, aberration-corrected TEMs can be good approximations to perfect microscopes.

The spots on the exit wave images can either be black or white, depending on sample thickness and zone axis. The dependence can be intuitively understood by the electron channeling theory

[71]. When a crystal is tilted to a zone axis, the atoms are aligned to columns along the electron beams, as shown in Fig. 2.6(a). After the electrons reach the sample, the routines of the passing electron wave in the sample is confined to the channels provided by the atoms in the material due to the interactions between the atom and the passing electrons. The intensity of the electron wave along each atom column is oscillating with a certain periodicity. Thus the intensity wave of the exit wave is thickness dependent. Furthermore, we can derive the intensity of the exit-wave is zone-axis dependent and element dependent, as shown in Fig. 2.6(b). For a zone axis along which the atoms are packed sparsely, the oscillation is slower along the columns where atoms are closely packed. With the same thickness and atom density of atom columns, the electron wave traveling along the columns with heavy elements oscillates faster than along the columns with light elements. Therefore, a significant advantage of HREM is that even with the presence of heavy elements, the light elements are can still be visualized.

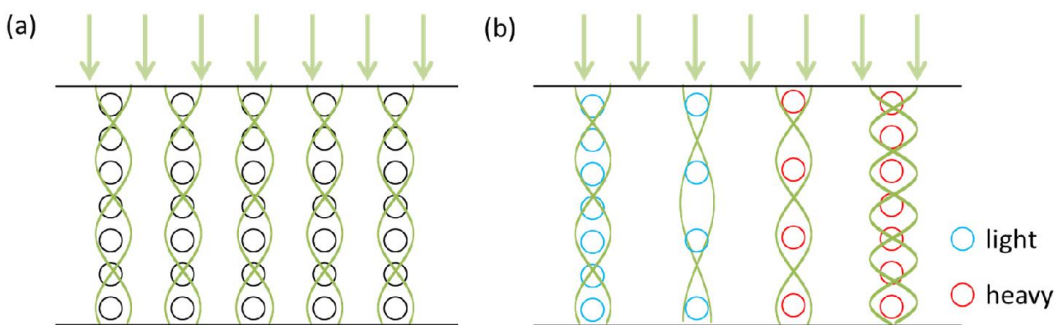


Figure 2.6 Schematic view of the electron channeling model.

Fig. 4 shows a comparison between the exit wave image and a simulated HREM images using an aberration corrected HREM with the change in thickness.

Now we start to take the TEM lens effect into consideration. If the sample is thin enough that the channeling wave before the contrast reversal is induced by the sample thickness, the thin sample can be considered as a phase object. This is a convenient model for the math, but it rarely that accurate in practice. The exit wave can be written as

$$\varphi_e(\mathbf{r}) = 1 - i\sigma V_p(\mathbf{r})t \quad \text{Equ. 9}$$

Equ. 9 is the well-known weak phase object approximation (WPOA) in HREM. The point spread function in a linear imaging model can be written as

$$P(r) = \mathcal{F}\{T(\mathbf{u})\} = \mathcal{F}\{A(\mathbf{u})E(\mathbf{u})\exp(i\chi(\mathbf{u}))\} \quad \text{Equ. 10}$$

where  $\mathbf{u}$  is the reciprocal vector, and  $T(\mathbf{u})$  is the point spread function  $P(r)$  in reciprocal space, And  $T(\mathbf{u})$  is the contrast transfer function (CTF) in HREM. In CTF,  $A(\mathbf{u})$  and  $E(\mathbf{u})$  are two envelop functions which limit the resolution, and the  $\chi(\mathbf{u})$  term includes all the aberration terms such as defocus, astigmatism, coma, spherical aberration, and other high order aberrations. The  $\chi(\mathbf{u})$  can be written in polar coordinates as

$$\begin{aligned} \chi(u, \theta) = c\mathbf{u} + \frac{f}{2}\lambda\mathbf{u}^2 + \frac{A_1}{2}\lambda\mathbf{u}^2\cos 2(\theta - \theta_{22}) + \frac{A_2}{3}\lambda^2\mathbf{u}^3\cos 3(\theta - \theta_{33}) \\ + \frac{1}{3}B_2\lambda^2\mathbf{u}^3\cos(\theta - \theta_{31}) + \frac{\lambda^3}{4}C_s\mathbf{u}^4 + \dots \end{aligned} \quad \text{Equ. 11}$$

where  $c$ ,  $f$ ,  $A_1$ ,  $A_2$ ,  $b$ ,  $C_s$  are the amplitudes of image drift, defocus, 2-fold astigmatism, 3-fold astigmatism, coma, and spherical aberration,  $\theta_{22}$ ,  $\theta_{33}$ ,  $\theta_{31}$  denote the angles of 2-fold astigmatism, 3-fold astigmatism, and coma.

Combining Equ. 9 and 10 and ignoring the high order terms, Equ. 7 results in

$$I = |\varphi(\mathbf{r})|^2 \approx 1 + 2\sigma V_p(r)t \otimes \sin(\chi(r)) \quad \text{Equ. 12}$$

provided the scattering is weak. Equ. 12 is essentially a result of using WPOA and linear imaging theory. According to Equ. 12, the white and black contrast in HREM images are controlled by the sine term. The reversal of a positive sine value to a negative one is the reason for contrast reversal in HREM images. Consider Equ. 12 in a reciprocal space can lead to a better understanding of contrast reversal for thin samples. Equ. 12 in reciprocal space becomes

$$I \approx \delta(u) + 2\sigma V_p(u)t \times \sin(\chi(u)) \quad \text{Equ. 13}$$

The  $\chi(u)$  term is in a sine function, which will have values ranging from -1 to 1 as  $u$  increase. For example, if a reciprocal lattice spot corresponding to a (200) lattice plane has a reciprocal spacing  $u_{(200)}$  that results in a negative value of the sine term while the  $u_{(311)}$  results in a positive value of the sine term, then the atoms within the (200) and (311) lattice planes show spots with a reversed contrast. As we want all the atoms to show up as the same contrast, the sine term should be as flat as possible. That is what aberration correction does. If the aberration correction is unavailable, then an optimum defocus value can be found to result in a long flat region on the sine function, which is often called large passband. Another interesting result of Equ. 13 is that the image contrast is minimal in an absolute aberration-corrected microscope ( $\chi(u) = 0$ ). Therefore, for some systems, a defocus or Cs is intentionally used in order to enhance the contrast of HREM images.

A list of some HREM simulation programs is shown in Table. 1. HREM is sensitive to lens aberrations, instrument stability, sample tilt and others. In a typical simulation program, besides

the sample structure, imaging parameters such as the defocus, spherical aberration, sample thickness, astigmatism, and sample tilt are all required as inputs to generate simulated HREM images. The more uncontrolled the imaging parameters are in the HREM experiment, the more effort it takes to use HREM simulation to interpret the experimental image.

<b>Programs</b>	<b>Authors</b>
MacTempas	Roar Kilaas
JEMS	Pierre Stadelmann
NCEMSS	Michael O'Keefe and Roar Kilaas
xHREM	Kazuo Ishizuka
QSTEM	Christopher Koch
WebEMAPS	Jian-min Zuo

Table 1 Some popular HREM simulation programs.

### 2.3.5 STEM

When the electron beam converges to a probe with a size on the atomic scale, atomic resolution imaging is possible. However, the contrast differs considerably between BF, ABF, ADF and HAADF images in STEM. A BF-STEM image should be understood (by reciprocity) as a HREM image. The changing of specimen thickness and defocus can cause contrast reversal in the atom positions. In ADF images, good image localization at atom positions is also due to s-state channeling although changes in orientation (strain) can also lead to significant contrast [72]. In general, it is better to use larger collection angles, i.e. HAADF, in order to minimize this although it can never be completely eliminated [54]. However, the set of channeling states are sampled differently by the detectors in ADF and particularly HAADF and HREM. In HAADF, the intensity of the spots only slightly changes with the specimen thickness [73]. There is no contrast reversal with respect to the thickness change provided the thickness is not too large. The atoms in HAADF images appear as white spots in most cases. The aberrations such as defocus

can also induce significant delocalization in HAADF images. However, the contrast will not reverse as in HREM. The atoms remain white as the defocus changes in HAADF images.

The significant difference between ADF/HAADF and BF images arises from the direct beam, which is collected by the BF detector. In principle, if the direct beam is blocked, the interference between the direct and diffracted beams in the specimen can be neglected. In practice, a beam stopper can be put on top of the BF detector to block the direct beam. The resulting images collected by the BF detector are ABF images. The ABF technique has the same advantage as HAADF in that it has relatively low sensitivity to specimen thickness and defocus compared to HREM. In addition, it has good sensitivity to both heavy and light elements, similar to BF imaging. Intuitively, as the large angle scattered beam (the electrons collected by HAADF) is not collected, the atoms appear black in ABF. Experimental and simulated ABF images on several materials all demonstrated that the ABF technique is less sensitive to thickness and defocus [74, 75].

Although the interpretation of HAADF and ABF images is relatively easy, sometimes image simulations are necessary, particularly for two materials with different thicknesses. In HAADF images, the “Z-contrast” is only for specimen with the same imaging condition (such as thickness and defocus). For two species in a specimen with different thicknesses, the intensity is not necessarily directly related to Z. The popular HREM simulation programs usually contain a package for STEM simulation. The simulation of STEM images usually requires more computational time than HREM simulation.



### 2.3.6 Multislice simulation for HREM

In the simulation program of HREM used in this study (Mactempas), the electron-specimen interaction is calculated based on the multislice method [76]. The lens impact on the exit wave is calculated based on the non-linear imaging theory [77]. Multislice method is an efficient approach to fully take the dynamical diffraction of the electrons in a specimen into account.

The electron behavior in the specimen is treated by solving the time-independent Schrodinger equation, as shown in Equ. 14.

$$\left[ -\frac{\hbar^2}{2m} \nabla^2 - eV(x, y, z) \right] \Psi_f(x, y, z) = E\Psi_f(x, y, z) \quad \text{Equ. 14}$$

As the electron beam has a high velocity along the z direction (optic axis of TEM), the wavefunction can be written as a wavefunction slowly changing with z times the plane wave in z direction.

$$\Psi_f(x, y, z) = \Psi(x, y, z) \exp\left(\frac{2\pi iz}{\lambda}\right) \quad \text{Equ. 15}$$

Then the schrodinger equation becomes

$$\left[ \nabla_{xy}^2 + \frac{4\pi i}{\lambda} \frac{\partial}{\partial z} + \frac{2meV(x, y, z)}{\hbar^2} \right] \Psi(x, y, z) = 0 \quad \text{Equ. 16}$$

The specimen can be treated as a layered structure along the z-direction, with each layer corresponding to a slice in the multislice method. The exit electron wave is then calculated by taking into account the electron wave scattered by many slices of the specimen in a specific thickness.

$$\Psi(x, y, z + \Delta z) = \exp \left[ \int_z^{z+\Delta z} \left( \frac{i\lambda}{4\pi} \nabla_{xy}^2 + i\sigma V(x, y, z') \right) dz' \right] \Psi(x, y, z) \quad \text{Equ. 17}$$

Further treatment with Equ.17 yields:

$$\Psi(x, y, z + \Delta z) = p(x, y, \Delta z) \otimes [t(x, y, z)\Psi(x, y, z)] + O(\Delta z^2) \quad \text{Equ. 18}$$

where  $t(x, y, z) = \exp\left[i\sigma \int_z^{z+\Delta z} V(x, y, z')dz'\right]$  is the transmission function and  $p(x, y, \Delta z) = \frac{1}{i\lambda\Delta z} \exp\left[\frac{i\pi}{\lambda\Delta z}(x^2 + y^2)\right]$  is the propagator function. As long as the initial value of the wavefunction at the entrance plane of the sample and the description of the crystal are given, the wavefunction at any depth of the specimen ( $z$  value) can be obtained.

### 2.3.7 Direct methods

The diffraction pattern we recorded by TEM or XRD shows the intensity of the diffracted beams, while the phase part is lost. If both the intensity and phase are known, the complete form of the structure factor of the crystal will be obtained. By using the complete form of the structure factor, a scattering potential map would be obtained by a simple inverse Fourier transform.

Direct methods are designed to approximate the lost phase term by exploiting the relationships of the phases in the kinematical amplitude measurement and the scattering from atoms. The phases only need to be in a root-mean-square error of 10–20 degrees in general. The estimated phases and the corresponding amplitude can produce the charge density (with x-rays) or electrostatic potential (with electrons) maps. The peaks in the maps are correlated with the real atom positions with an error less than 1Å. As the electron diffraction for surfaces usually only have very limited number of reflections, usually multiple possible density maps will be obtained. In addition, the density maps for surfaces are only for the reconstructions themselves. There is no information of bulk registry. Thus additional refinements should be conducted. A viable way is to perform DFT calculation to compare the energies of each possible structure.

### 3. Surface Reconstructions of SrTiO<sub>3</sub> (001)

#### 3.1 Introduction

This chapter presents the surface reconstructions of SrTiO<sub>3</sub> single crystal surfaces. The atomic structures of solved SrTiO<sub>3</sub> surface reconstructions will be briefly illustrated. The focus of this chapter is on the atomic structure a SrTiO<sub>3</sub>(001)-(2×2) surface reconstruction. Previous STM studies reveals that there is a (2×2) reconstruction on the (001) surface of SrTiO<sub>3</sub> with a 4-fold symmetry [78]. However, the previously proposed solution for the (2×2) reconstruction only has a 2-fold symmetry [79, 80]. By comparing the simulated STM images of the four possible surface structures, the best-fit structure for the experiment with a 2-fold symmetry is found. If the previous proposed solution is correct, this study suggests there are two different (2×2) surface structures.

This chapter illustrates the conventional methods to solve an atomic structure of surface reconstructions, which combine the STM, DFT, and AES. Coupling the techniques is powerful. A structural solution can be obtained to meet all the requirements deduced from the experimental results. However, the structural solutions from the conventional methods may not be unique. Misinterpretation of an experimental result with a wrong structural model is possible. The problem is more severe for complex materials with a large reconstructed surface unit cell, as there are too many possible structural solutions to handle. In the present case, with the (2×2) surface, there are also a large amount of possible surface structural solutions. Fortunately, the reconstructed cell is small. In addition, the previous work on the atomic structures of SrTiO<sub>3</sub> surface reconstructions clearly indicates the double-TiO<sub>2</sub> surface feature [47, 80-83]. Following

the implication, together with experimental results obtained, the number of possible structural solutions is significantly reduced. The proposed structure matching all the requirements can be a correct one.

### 3.1.1 The Solved Surface Reconstructions of SrTiO<sub>3</sub> Single Crystals

Especially for complex materials, the surface structures can be very complicated. SrTiO<sub>3</sub> is a relatively simple material with a perovskite ABO<sub>3</sub> (A and B are metal ions) structure type. Along the [001] direction, SrTiO<sub>3</sub> can be considered as a repeatedly alternating stacking of SrO and TiO<sub>2</sub> layer, as shown in Fig. 3.1. As a result, the bulk truncated surface can either be a SrO and TiO<sub>2</sub> layer. If the bulk truncated surface is not stable, the situation can be more complicated. A number of surface reconstructions, including the (1×1) [84], (2×1)[47, 85, 86], (2×2) [78, 84, 87-92], c(4×2) [81, 85, 93], c(4×4) [85], (4×4) [93], c(6×2) [94, 95], ( $\sqrt{5}\times\sqrt{5}$ )R26.6° [96-99] and ( $\sqrt{13}\times\sqrt{13}$ )R33.7° [82, 100], have been reported using different surface sensitive techniques. Many structural models have been proposed for some of the reconstructions.

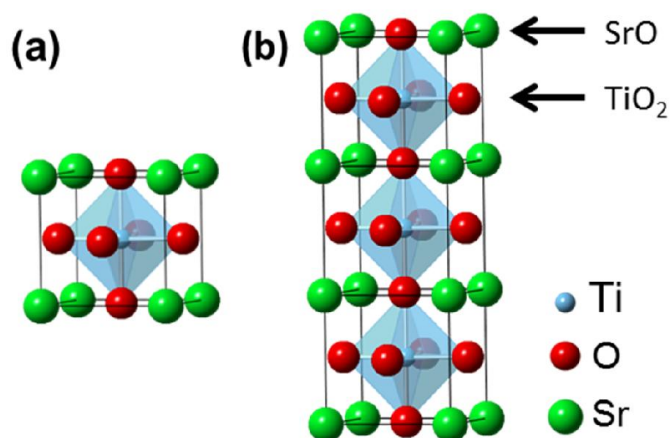


Figure 3.1 The bulk and bulk truncated surface structures of SrTiO<sub>3</sub>.

There are mainly three categories of proposed structural solutions for the surface reconstructions of SrTiO<sub>3</sub>. The generally accepted one is based on the double-TiO<sub>2</sub>-layer (DL) model which is obtained from combined results of the TEM (or X-ray) diffraction experiments, DFT calculation, and simulations of microscopic images [47, 79-82]. The surface structures obtained from this approach can be considered unbiased best-fit solutions for the experimental results. The other two categories include reconstruction models based on single Sr adatom [93, 98] or O vacancies [101]. However, these models are usually proposed from the STM images. It is possible that other structures (such as the DL models) can also match the STM results. In addition, Sr adatom or O vacancies indicate strong reduced surfaces. The reconstructions are likely unstable at realistic conditions, such as in the air. This is also indicated by DFT studies, which suggest that the Sr adatom model requires conditions that far from equilibrium [102]. The atomic models of some solved DL reconstructions of SrTiO<sub>3</sub> (001) are illustrated below.

#### **3.1.1.1 (2×1)**

The (2×1) surface reconstruction was reported by Cord et al. Erdman et al. demonstrated for the first time using diffraction analysis (direct methods) coupled with DFT and HREM plan-view imaging to obtain a unique solution of the (2×1) [47]. The proposed structure has an additional reconstructed TiO<sub>2</sub> layer on a TiO<sub>2</sub>-terminated SrTiO<sub>3</sub> surface, which was then referred to as a double-TiO<sub>2</sub>-layer model (DL). The DL concept indicates the complexity of SrTiO<sub>3</sub> surface and paves the way for understanding surface chemistry. A number of structural solutions of the other reconstructions were found to share similar surface chemistry and structure. Fig. 3.2 shows the schematic model of the DL-(2×1) structure. Each surface Ti atom is bonded to 4 surface O atoms and 1 subsurface O atom, which can be considered as a TiO<sub>5</sub> polyhedral unit. There are debates over the stability of this DL-(2×1) model, as the surface energy is relatively high. Combining STM,

DFT, XPS, and BVS, a more stable reconstruction under realistic conditions should be H<sub>2</sub>O dissociatively adsorbed on the base DL-(2×1) surface [103].

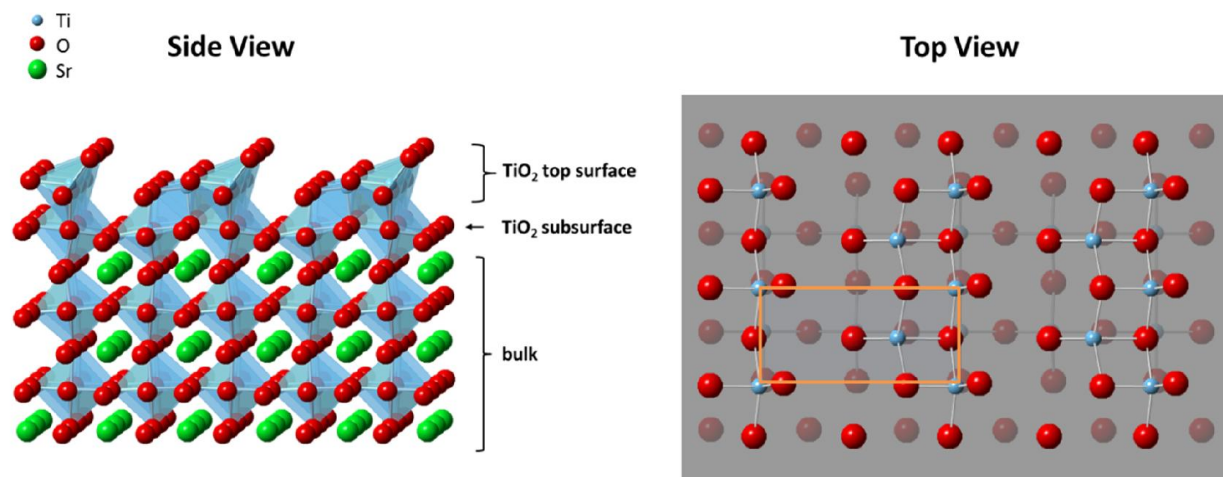


Figure 3.2 Side and top views of the DL-(2×1) model.

### 3.1.1.2 (2×2)

The first (2×2) reconstruction on SrTiO<sub>3</sub> (001) was reported by Cord et al., who used LEED and annealed the sample in an oxygen-rich vacuum; no structural model was proposed [84]. An early STM study which showed a (2×2) surface reconstruction was later shown to be a ( $\sqrt{5}\times\sqrt{5}$ )R26.6° reconstruction [104, 105]. Two more recent STM studies conducted by Silly et al. and Kubo et al. found that the (2×2) surface has a 4-fold symmetry [78, 93]. Kubo et al. further proposed a structure consisting of Sr adatoms on a TiO<sub>2</sub>-terminated surface [93]. In a theoretical study, Warschkow et al. used DFT calculations to explore several possible reconstructions with a double-layer TiO<sub>2</sub> termination, including three with (2×2) periodicity [79]. In 2007, Herger et al. supported the double-layer TiO<sub>2</sub> model using surface X-ray diffraction and showed that there is a coexistence of (2×1), (2×2) and (1×1) reconstructions with a temperature dependence [80]. The (2×2) domains were attributed to the structure which has the lowest surface energy with a 2-fold

symmetry in the study by Warschkow et al. The atomic model is shown in Fig. 3.3. Similar to the  $(2 \times 1)$ , the surface can be considered an arrangement of  $\text{TiO}_5$  polyhedral units.

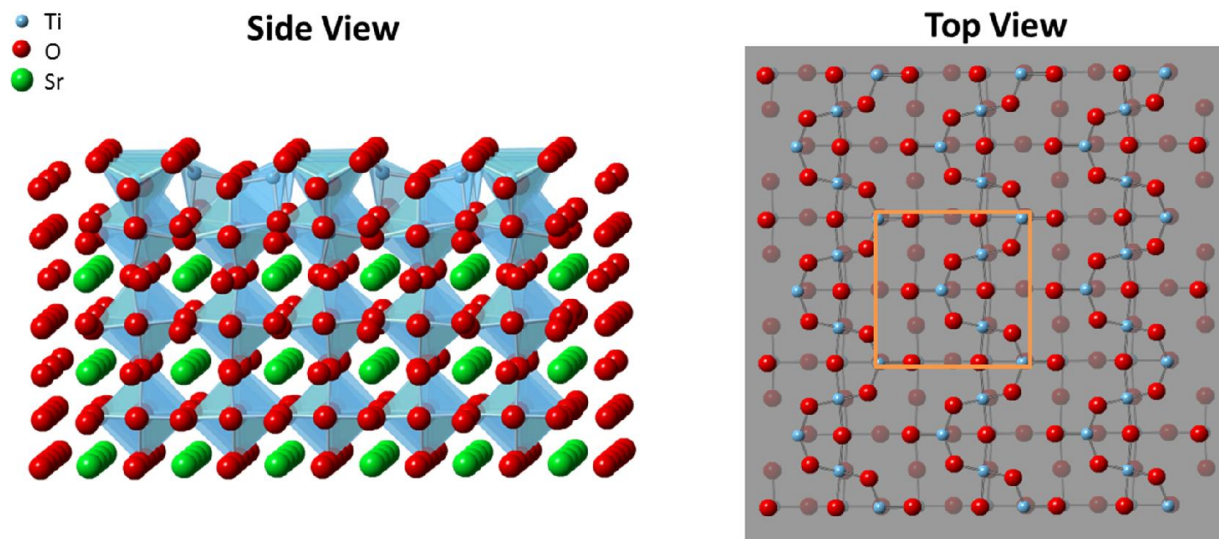
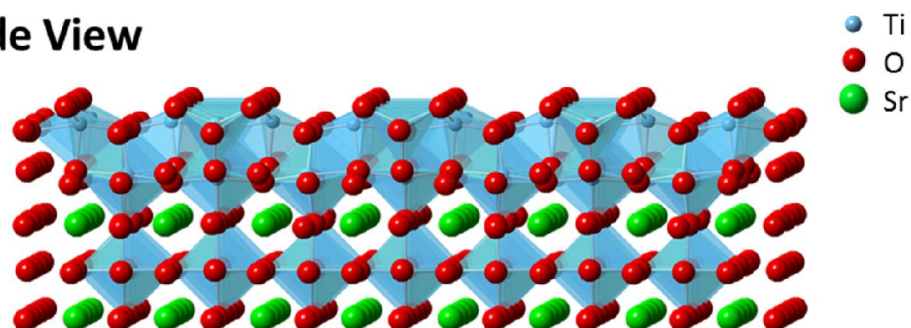


Figure 3.3 Side and top views of the DL- $(2 \times 2)$  model.

### 3.1.1.3 $c(4 \times 2)$

The  $c(4 \times 2)$  was first observed by LEED and STM [85, 94]. Erdman et al. first proposed the DL- $c(4 \times 2)$  solution using TEM diffraction analysis and DFT [81]. The DL- $c(4 \times 2)$  can be deduced from the DL- $c(2 \times 1)$  reconstruction. Fig. 3.4 shows the atomic model of the reconstruction. The top layer consists of edge-sharing  $\text{TiO}_5$  polyhedra. The aftermath studies favor the DL- $c(4 \times 2)$  model. For example, the plan-view EELS study shows a good match between the experimental result and the simulation from the DL- $c(4 \times 2)$  model [83]. In addition, the polyhedral quartet feature of the DL- $c(4 \times 2)$  model was believed to exist in other reconstructions of  $\text{SrTiO}_3$  (001).

### Side View



### Top View

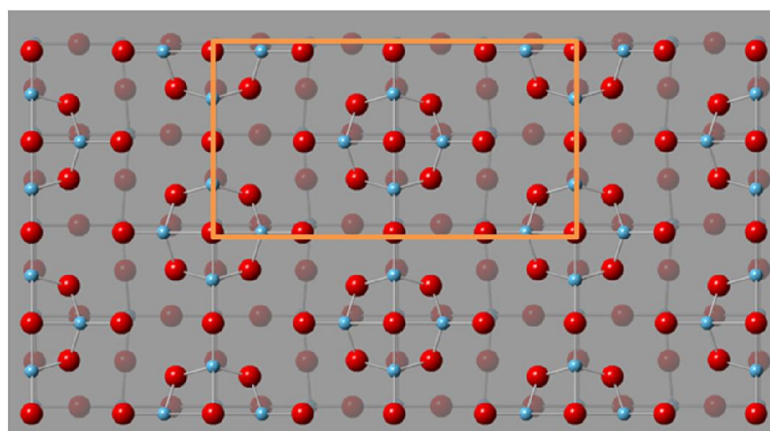


Figure 3.4 Side and top views of the DL-c(4×2) model.

#### **3.1.1.4 (3×3), $(\sqrt{13}\times\sqrt{13})R33.7^\circ$ , and $(\sqrt{5}\times\sqrt{5})R26.6^\circ$**

The  $(\sqrt{13}\times\sqrt{13})R33.7^\circ$  and  $(\sqrt{5}\times\sqrt{5})R26.6^\circ$  reconstructions of SrTiO<sub>3</sub> (001) have been observed by many experiments [82, 96-100]. Kienzle et al. obtained a structural solution from the TEM diffraction analysis and DFT calculation [82]. The proposed solution is similar to the DL reconstructed models based on the arrangements of the polyhedral TiO<sub>5</sub> polyhedral units, as shown in Fig. 3.5. The DFT calculation shows the three DL reconstructions fall close to the convex hull of the surface energy versus the surface excess TiO<sub>2</sub>. Moreover, a new concept of



glass-like reconstructions is proposed. With the analogue of  $\text{SiO}_2$  glass, the surface can be considered as networks of locally ordered corner- and edge-sharing  $\text{TiO}_5$  units. Thus, it is possible to have a coexistence of locally ordered  $(3 \times 3)$ ,  $(\sqrt{13} \times \sqrt{13})R33.7^\circ$ , and  $(\sqrt{5} \times \sqrt{5})R26.6^\circ$  reconstructions. The coexistence is assigned to the similar energy levels of the three reconstructions, and increasing the entropy can reduce the Gibbs free energy.

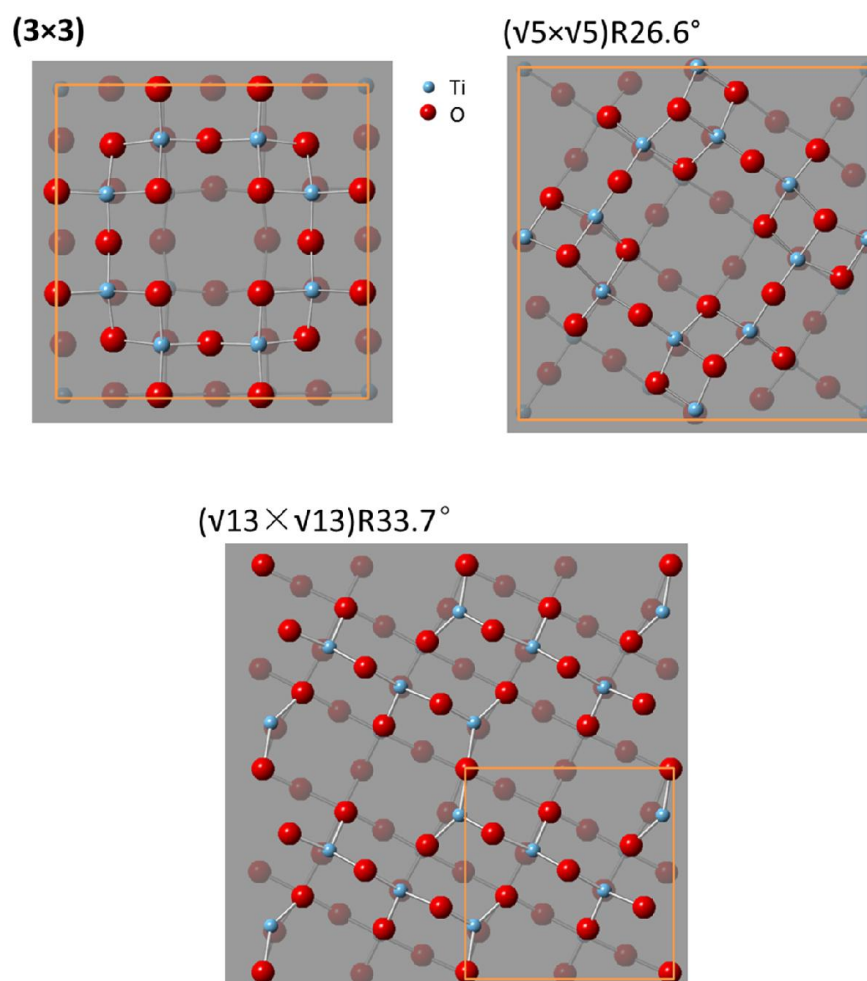


Figure 3.5 Illustration of the  $(3 \times 3)$ ,  $(\sqrt{13} \times \sqrt{13})R33.7^\circ$ , and  $(\sqrt{5} \times \sqrt{5})R26.6^\circ$  surface models proposed by Kienzle et al.

### 3.1.2 Methods

The experimental data used here is from the previous work by Silly et al [78]. The sample was purchased from PI-KEM, UK, with 0.5% Nb doping and epi-polished (001) surfaces. Before transferring the sample to the UHV chamber, it was chemically etched in a buffered  $\text{NH}_4\text{F}$ -HF solution to clean the surface contamination as well as prudentially remove the surface SrO. The STM experiments were carried out in a UHV chamber (JEOL JSTM4500S). The experimental pressure was kept down to  $10^{-10}$  mbar. A  $(2\times 2)$  surface reconstruction was observed after annealing the sample at  $950^\circ\text{C}$  for 2 hours.

The DFT calculations were performed using the full-electron WIEN2k code. The  $\text{TiO}_{2-x}$  terminated surfaces were modeled using a repeated slab configuration, consisting of atomic layers with the following stacking sequence: surface- $\text{TiO}_2$ -SrO- $\text{TiO}_2$ -SrO- $\text{TiO}_2$ -SrO- $\text{TiO}_2$ -SrO- $\text{TiO}_2$ -SrO- $\text{TiO}_2$ -surface. The vacuum spacing between each slab was around 14 Å. The Sr adatom surface was modeled using a similar slab but with one additional layer of both  $\text{TiO}_2$  and SrO. The corresponding vacuum spacing was around 13 Å in this case. All atoms were allowed to relax until all forces were below  $0.1 \text{ eV}/\text{Å}$ . Muffin-tin radii of 2.36, 1.70 and 1.20 Bohr were used for Sr, Ti, and O, respectively, as well as a  $\text{min(RMT)}\times\text{Kmax}$  of 5.5. The PBE version of the generalized gradient approximation for the exchange-correlation energy was chosen. Constant-current STM images were simulated using a modified Tersoff-Hamann approximation [69, 70], considering the states from the Fermi energy ( $E_f$ ) to about 1.3 eV above it, after artificially populating these. The 1.3 eV is also the bias voltage of the STM study. In addition, a weighting term was applied to account for the varying effective tunneling barrier, as well as a

blurring addition through a quarter-cosine curve radial convolution feature of radius  $2\text{\AA}$  to account for the tip-size and thermal effects; the method is described in greater detail in [70].

### **3.1.3 Result and Discussion**

Fig. 3.6 shows a large flat terrace of the square ( $2\times 2$ ) surface reconstruction. Fourier filtering technique was used to average the image to reveal detail information. The power-spectrum of the STM image is inset in Fig. 3.6. The Fourier averaged image is shown in Fig. 3.8.

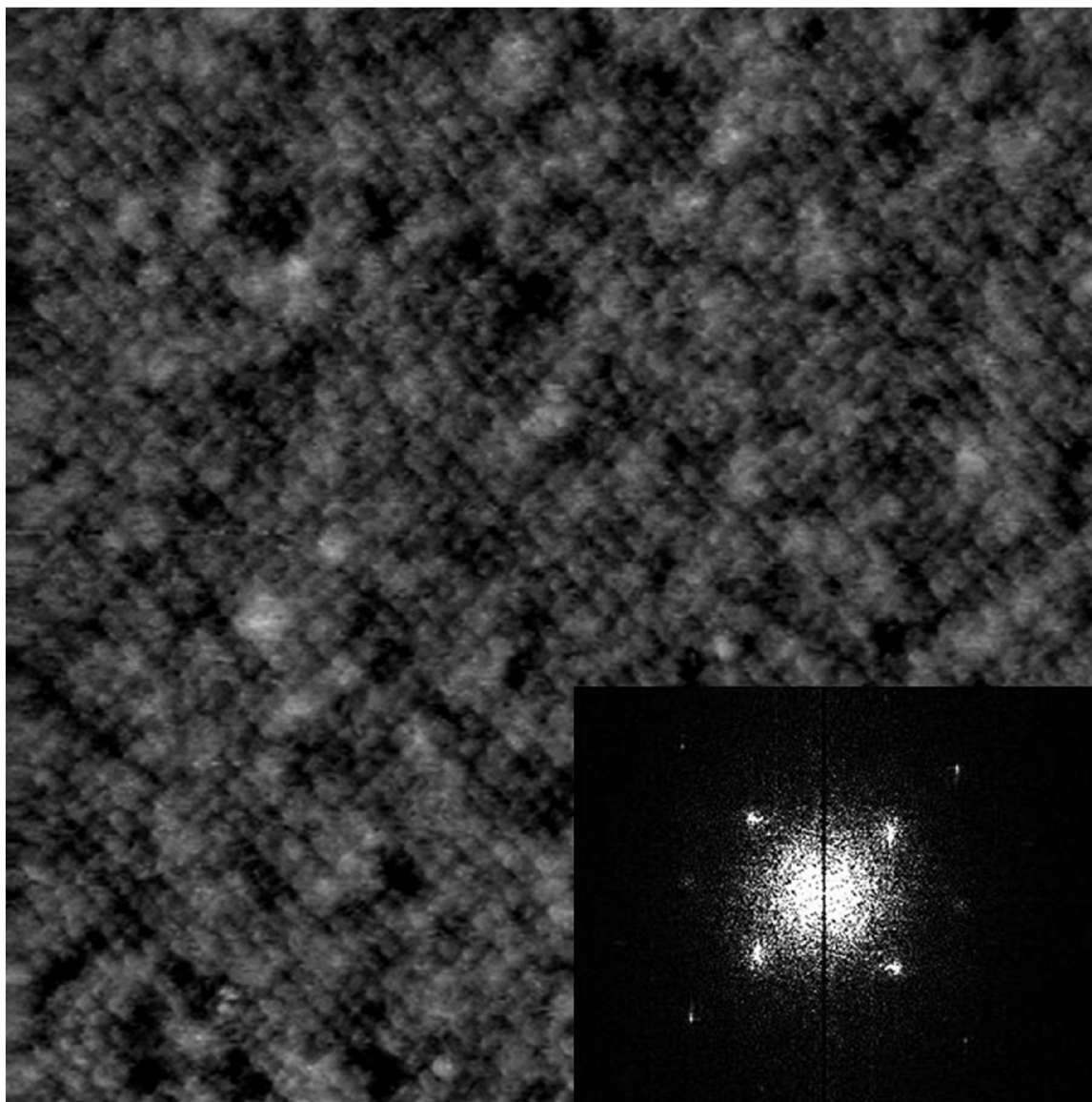


Figure 3.6 An experimental STM image shows a  $\text{SrTiO}_3(001)-(2 \times 2)$  surface reconstruction with a 4-fold symmetry. The inset shows the power spectrum of the image.

A previous Auger electron spectroscopy (AES) study [106] investigated the surface chemistry of this sample. There was no visible signal of Nb up to the detection limit of AES. According to the AES data, there were hints of a slightly reduced oxygen coverage of the  $(2 \times 2)$  surface, with the UHV-cleaved (001) surface as a reference.

While it is in principle possible for the reconstruction to be SrO-rich, the only confirmed SrTiO<sub>3</sub> (001) surface structures are TiO<sub>2</sub>-rich. Moreover, Kawasaki et al. showed that the chemical etching process in weakly acidic NH<sub>4</sub>F–HF solution favors the TiO<sub>2</sub> terminated surface by preferentially removing SrO [25]. Hence four possible surface structures were considered. Three of them are TiO<sub>2-x</sub>-terminated surface structures of SrTiO<sub>3</sub> (001), as shown in (2×2)A, (2×2)B and (2×2)C in Fig. 3.7. The (2×2)D in Fig. 3.7 is the Sr surface adatom model proposed by Kubo et al [93]. For simplicity, no Nb is considered in any of the DFT models. The (2×2)A and (2×2)C structures in Fig. 3.7 are double-layer TiO<sub>2</sub> terminated surface models, which were also considered in Warschkow et al.'s work [79]. The (2×2)C structure has the lowest surface energy according to the DFT calculations and usually is referred to as a solved structure for the (2×2) reconstruction. However, it does not have the 4-fold rotational symmetry found in the STM images. It is expected that the simulation of this structure will not match the experimental STM image well. The (2×2)B model, not explored in the aforementioned theoretical study, was considered because of the slight oxygen reduction observed in the AES study, which is also the only qualitative difference with respect to (2×2)A. The (2×2)D model was also chosen as a candidate surface structure because of its correct 4-fold symmetry and oxygen deficiency.

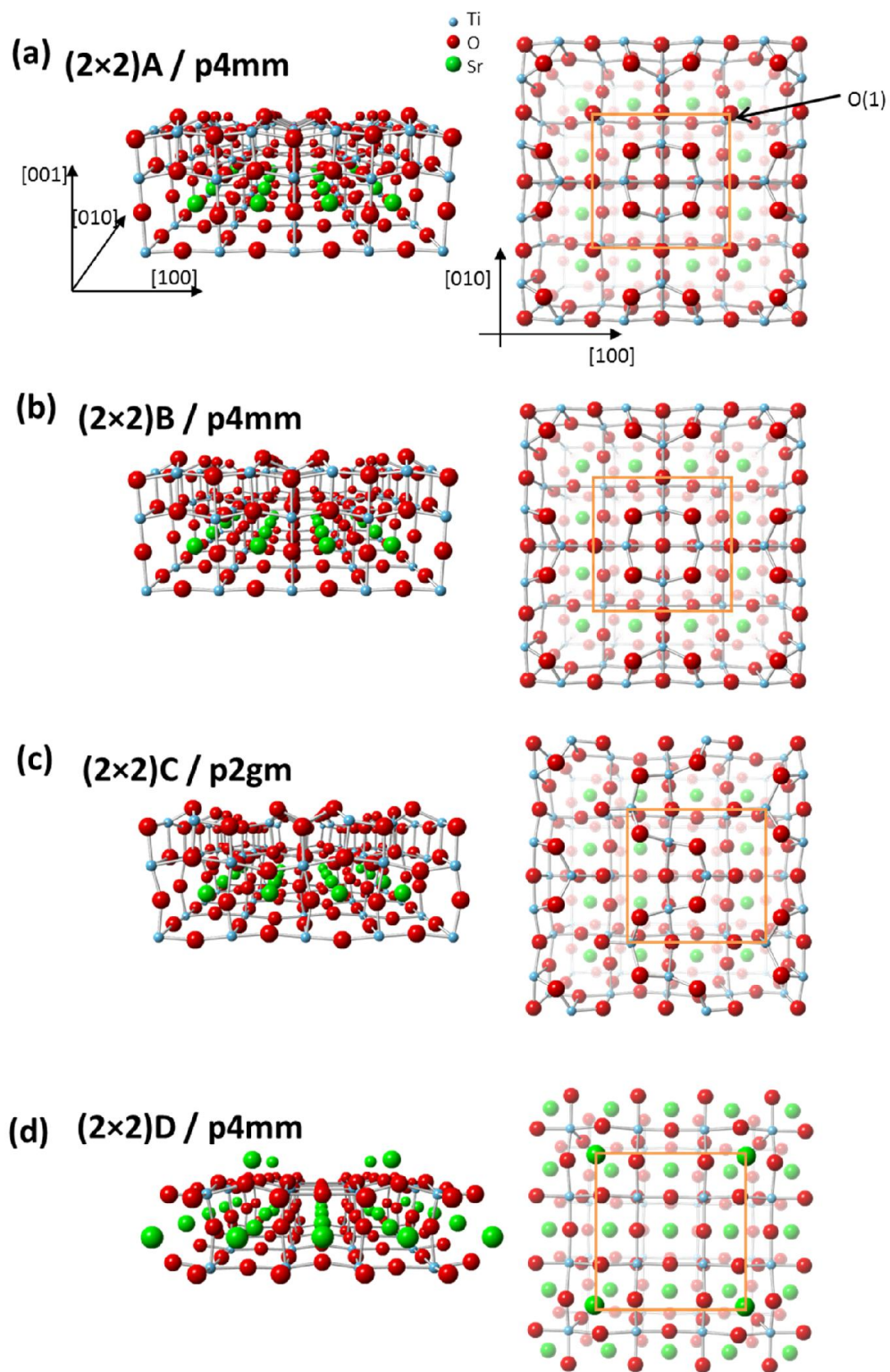


Figure 3.7 The four  $(2 \times 2)$  models used for STM simulation.

Fig. 3.8 shows the comparison between the averaged experimental STM image and the simulated images. The simulated image from the  $(2\times 2)A$  structure is the closest to the experimental STM image, as shown in Fig. 3.8(b). This is because the row of spots in the filtered image is continuous, as indicated by the red circles. This feature indicates that there is a nonzero local DOS (within the imaged energy range) between the large spots in the rows, which is most visible in the simulated image by the  $(2\times 2)A$  model. The other models are quantitatively worse fits. As expected, the simulated image of the previously solved  $(2\times 2)$  model with a 2-fold symmetry is very different from that of the experiment. It shows a zigzag contrast compared to the plaid-like contrast in the experimental STM image. The mismatch cannot be overcome by changing the STM simulation parameters, such as the bias voltage and the isosurface density within a realistic range.

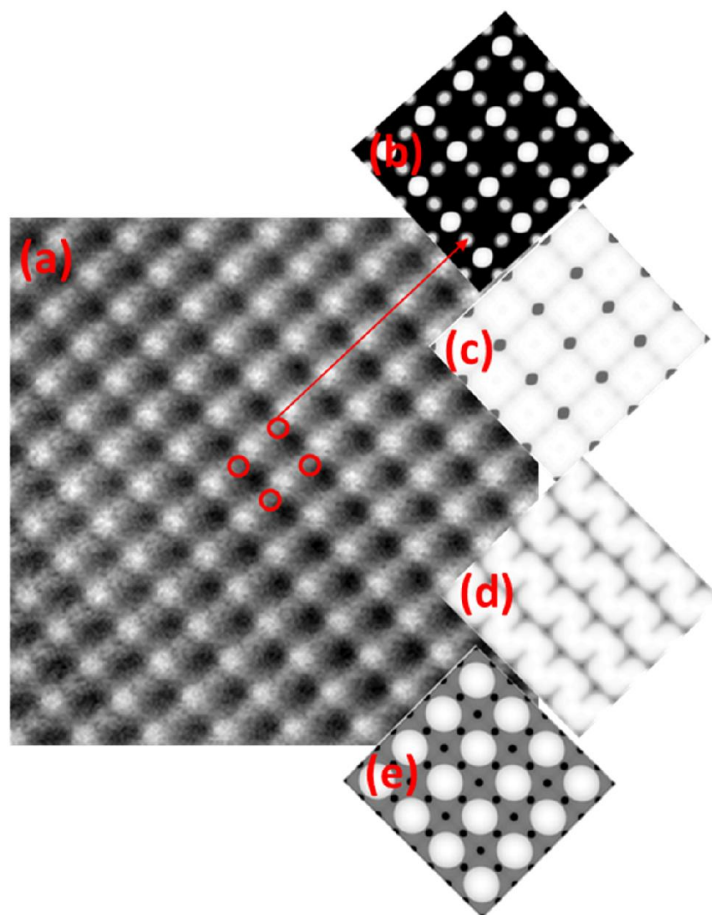


Figure 3.8 The comparison of averaged experimental STM image and the simulated images using different models. (a) The averaged image of Fig. 3.6. (b)-(e) Simulated STM images using the models illustrated in Fig. 3.7(a)-(d) respectively.

The proposed model ((2×2)A in Fig. 3.7) is similar to the structurally solved SrTiO<sub>3</sub>(001)-c(4×2). Shifting every second reconstructed cell row in (2×2)A by one bulk lattice constant will result in the solved stable c(4×2) surface. The geometrical similarity may suggest that the (2×2) surface may be transformed from the c(4×2) surface by using different sample preparation conditions. The other characteristic of the proposed (2×2) model is the somewhat unusual one-fold coordinated surface oxygen atoms are bonded to the subsurface Ti atoms to form double bonds



(Ti=O). The Ti=O has a bond length about 0.3 Å less than that of the typical Ti–O single bond in SrTiO<sub>3</sub> bulk structures. The relaxation may help to compensate the energy associated with the Ti=O. A bond-valence sum analysis shows that the valences for Ti and O atoms of the Ti=O are 3.77 and –1.71, respectively, which are close to what is expected.

The surface energy calculated for the proposed structure ((2×2)A in Fig. 3.7) is 1.05 eV per (1×1) unit cell, as determined by subtracting the energy for bulk SrTiO<sub>3</sub> and TiO<sub>2</sub> from the total energy. This is comparable with other structures with the same stoichiometry modeled using the same DFT calculation parameters. Although the (2×2)A surface is not the lowest energy case, its surface energy is lower than the solved and often observed (2×1) surface, which is 1.15 eV per (1×1) unit cell. Moreover, shifting every second reconstructed cell row in the (2×2)A structure by one bulk lattice constant will result in the solved c(4×2) structure, as shown in Fig. 3.4. The agreement between the simulated and experimental STM data also indicates the (2×2)A structure is reasonable. It is worth noting that two different reconstructions with the same stoichiometry and periodicity may well exist; the present report on the (2×2)A structure does not contradict the identification by Herger et al. on the (2×2)C structure [80].

Usually, annealing in UHV results in a slight reduction of the oxide surface. However, (2×2)A is fully oxidized. The AES experiment has shown that the oxygen peak height reduction of the present (2×2) specimen is between 3% and 7%, but there is no discernible titanium enrichment. The origin of the oxygen peak height reduction could be due to any number of factors that are not related to the structure of the surface reconstruction. The factors include the following: the UHV cleaved surface is not necessarily a good reference of stoichiometry as it can readily adsorb water and other oxygen containing molecules; the oxygen deficiency is due to randomly

distributed oxygen vacancies; and different reconstructions result in different shadowing and Auger electron diffraction effects that affect the oxygen peak height. It is worth noting that the oxygen signal in the AES study on the  $(2\times 2)$  is comparable with that found on the  $\text{SrTiO}_3$   $(001)$ - $c(4\times 2)$ , which has a double-layer  $\text{TiO}_2$  terminated surface and is full oxidized.

### 3.1.4 Summary

With STM image simulation using DFT, four structural models are compared. The fully oxidized DL- $(2\times 2)$ A with a 4-fold symmetry best matches the experimental results. The simulated STM image from the solved DL- $(2\times 2)$ C with a 2-fold symmetry shows very different contrast from the experimental one. The proposed DL- $(2\times 2)$ A in this study shows reasonable surface energy and surface BVS. This study clearly indicates the different structures can exist for the same surface periodicity and stoichiometry (the  $(2\times 2)$ A and  $(2\times 2)$ C in this case). The similarity between the square DL- $(2\times 2)$ A and  $c(4\times 2)$  indicates the kinetics may also play an important role in surface reconstructions.

## 4. Atomic Surface Structures of CeO<sub>2</sub> nanoparticles

### 4.1 Introduction

CeO<sub>2</sub> has been widely used in catalysis [5, 30-32], SOFCs [15, 33, 34], and chemical mechanical abrasive materials [21, 107]. CeO<sub>2</sub> based materials can be used as a three-way catalyst for automobile exhaust [108]. In SOFCs, CeO<sub>2</sub> are used as an anode material [14]. In chemical mechanical polishing field, the use of CeO<sub>2</sub> powder in slurries can enhance the polishing rate of silicon wafers [20]. The excellent properties originate from its remarkable redox ability [2], oxygen storage capability [109], and ion conductivity [33]. For example, under reducing conditions, the O vacancies start to form on the surface [110]. Under oxidation conditions, the vacancies can be eliminated rather easily. For some oxidative catalytic reactions, it is believed that the lattice O at the surfaces of CeO<sub>2</sub> participate in the reactions to provide atomic oxygen [2, 35], while the adsorption of O<sub>2</sub> gas is on the surface O vacant sites of CeO<sub>2</sub>. The formation of surface O vacancies is associated with the reduction of surrounding Ce<sup>4+</sup> to Ce<sup>3+</sup> [110]. The stability of Ce with either a 4+ or 3+ valence is believed to be the main reason for the excellent redox properties.

To further enhance the redox properties of CeO<sub>2</sub>, usually there are two general approaches. One is to substitute other oxides such as ZrO<sub>2</sub> to form a CeO<sub>2</sub>-ZrO<sub>2</sub> solid solution [5]. For ZrO<sub>2</sub>, it is probably the lattice strain effect that reduces the O vacancy formation energy [111, 112]. The substitution of Ce by other metals such as Mn, Pr, Sn, the O vacancy formation is enhanced possibly by both lattice strain and electronic effects [113], it should be noted that the valences for those metals are different from the Ce. The other approach is to synthesis CeO<sub>2</sub> nanoparticles

with different shapes [114-117]. The shape control of CeO<sub>2</sub> nanoparticles are rather easy, and a variety of CeO<sub>2</sub> nanostructures including nanocubes, nanorods, nanooctahedra have been obtained [118, 119]. The catalytic properties of these nanostructures are often different, which is attributed to the facets exposed of the nanocrystals. The nanorods have mainly {100} and {110} surfaces exposed, while the nanooctahedra have {111} facets predominantly exposed and the nanocubes have the {100} facets predominantly exposed. The (100), (111) and (110) surfaces have different atomic and electronic structures, which can lead to differences in surface O vacancy formation energy and catalytic performances. For example, CeO<sub>2</sub> nanocubes show higher activity in water gas shift (WGS) reaction than CeO<sub>2</sub> nanooctahedra [120].

Fig. 4.1(a) shows a schematic view of the bulk and the bulk truncated surface structures of CeO<sub>2</sub>. CeO<sub>2</sub> is a centrosymmetric material with a fluorite structure (space group Fm-3m). However, cleaving CeO<sub>2</sub> along different directions results in distinct surface structures and stabilities. For ionic crystals, there is a dipole moment associated with each pair of cation and anion. Tasker classified the surface structures of ionic crystals into three categories based on the electrostatic considerations [121]. The (110) surface of CeO<sub>2</sub> is a Type-I surface. In the [110] direction, CeO<sub>2</sub> is composed of stacking layer units with stoichiometry of CeO<sub>2</sub>, as shown in Fig. 4.1(b). In each unit, the dipole moments are in opposite directions that the net dipole moment is zero. Therefore the bulk truncated CeO<sub>2</sub> (110) surface is non-polar and stable. For the (111) surface, the bulk truncated surface can be O- or Ce-terminated, as shown in Fig. 4.1(c). The O-terminated (111) surface is classified as the type-II surface, which is also considered as a stable surface. For this type of surface, the stacking unit can be three layers with the Ce layer in the middle. Therefore, the net dipole moment for each stacking unit is zero. In contrast, the Ce-terminated (111) surface

is a type III polar surface. The stacking unit is three atom layers with a net dipole moment associated from the O layers to the Ce layer. As the thickness increase, the dipole moment stacks up and the surface becomes unstable. Therefore, an O-terminated (111) surface is often assumed. A more interesting case is for the (100) surface. Along the [100] direction, both the bulk truncate O- or Ce-terminated surfaces are type-III polar surfaces. A possible solution for the surface is transferring  $\frac{1}{2}$  O atoms from an O-terminated surface to a Ce-terminated surface although this would lead to a macroscopic difference in the oxygen chemical potential. As a result, a new stacking unit can be defined and there is zero net dipole moment associated with each unit. In principle, the  $\frac{1}{2}$  O reconstructed surface should be stable, which is referred to as the CeO termination. It is worth noting that the criteria of the surface stabilities are only valid for the “normal” condition. For instance, at a high oxidation condition, the (100) surface can have a stable O termination. In contrast, with highly reducing conditions, the Ce-terminated surface can be stabilized.

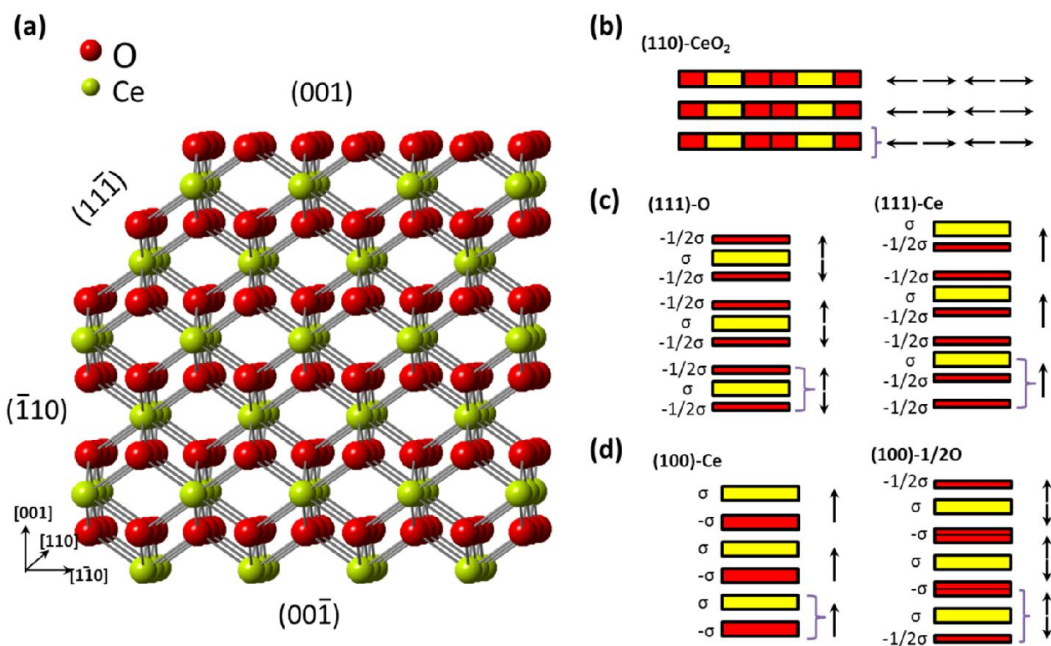


Figure 4.1 Schematic drawings of CeO<sub>2</sub> bulk structure (fluorite), surfaces and dipole moments. (a) A CeO<sub>2</sub> structural model with truncated {100}, {110}, and {111} surfaces. (b) Schematic view of the stacking of dipole moments along the [110] direction. The red and yellow squares represent O and Ce atoms and each arrow represents a dipole moment. The curly brackets represent a repeating unit. (c) Schematic view of the stacking of dipole moments along the [111] direction. The O-terminated (left) and Ce-terminated (111) (right) surfaces result in nonpolar and polar surfaces respectively. (c) Schematic view of the stacking of dipole moments along the [100] direction. The Ce-terminated (100) is a type III polar surface (left). The dipole moment can be compensated by transferring 1/2 O atoms from an O-terminated side to a Ce-terminated side (right).

The electrostatic arguments qualitatively describe the surface stability and predicted possible surface structures. Studies on the surface structures of CeO<sub>2</sub> are extensive, especially for the (111) surface of CeO<sub>2</sub> single crystal [110, 122, 123]. It is generally believed the (111) surface is O-terminated. In reducing conditions, surface and subsurface O vacancies can be created. For example, Esch et al. used DFT and STM studies to show that subsurface oxygen vacancies are

critical for the formation of linear vacancy clusters on the (111) surface [110]. The study indicates that subsurface vacancies can enhance further surface oxygen release in catalytic applications. Here the subsurface refers to the third surface layer (O layer). Recently the (2×2) ordering of subsurface O vacancies was reported by Torbrügge et al. using AFM, which is also in agreement with later STM and DFT studies [123]. Nörenberg et al. observed a number of surface reconstructions on the CeO<sub>2</sub> (100) surface [124]. The  $\sqrt{2}/2(3\times 1)R45^\circ$  and  $\sqrt{2}/2(3\times 2)R45^\circ$  surface reconstructions were observed initially at 400°C after 900°C annealing. The  $\sqrt{2}/2(3\times 1)R45^\circ$  surface was modeled by a  $\frac{1}{2}$  O removed, however, the proposed surface structures were not verified by other studies. The c(3×3) was observed at 400°C after reoxidation, annealing and sputtering. When it comes to the (110) surface, no clear atomic scale images were available. Nörenberg et al. observed line features in their STM images after annealing to 940°C and the structure was assigned to a (2×1) reconstruction [125]. After annealing to 1030°C, the {111} facets formed on the surface.

The surface structures of CeO<sub>2</sub> nanoparticles are more relevant in catalysis than their single crystal counterpart. Compared to STM, HREM is a convenient technique for imaging atomic surface structures, especially for the recently developed aberration-corrected TEM. The aberration-corrected HREM studies were able to image the surface Ce atom positions of CeO<sub>2</sub> nanoparticles [126-128]. However, the O atoms were not visible. In principle, the separation of O atom column are large enough to be imaged under low index zone axes. It is possible that the Ce atom columns are much heavier than the O columns, contrast of O atoms are not as significant as that of Ce atoms if the specimen is not well-tilted.

## 4.2 Experiment

CeO<sub>2</sub> nanocubes were prepared following the procedures detailed in a previous work [52]. In a typical synthesis, 0.868 g Ce(NO<sub>3</sub>)·6H<sub>2</sub>O (99% Sigma-Aldrich) and 9.6 g NaOH was dissolved in 5 and 35 ml DI water respectively. The solutions were mixed with continuous slurring for 30 minutes. The mixed solution was transferred to a 125 ml autoclave with a Teflon liner. The autoclave was heated to 180 °C for 24 hours. The end product with white (with slight yellow) color was cleaned, collected, and dried at 90 °C for 10 hours. The dry nanocubes were then dispersed in ethanol to make a suspension. Several droplets of the suspension were applied to a Cu grid with lacy carbon film coated. The Cu grid was put into a TEM column without further specimen treatment.

The HREM experiment in this study was performed using a Cc and Cs corrected FEI Titan 80-300 KeV microscope operated at 200 KeV at Argonne National Laboratory. All the aberrations were tuned to an acceptable level before recording the images. Typically, the Cs was corrected to ~5 μm, Cc was corrected to < 1 μm. The 2-fold astigmatism was corrected to ~ 0 nm. The coma and 3-fold astigmatism were tuned to be several nanometers. These parameters were measured before and after the HREM experiment. The exact values were continuously changing during the experiment. Therefore, the experimental values of the aberrations were only used as starting values for HREM simulations.

The HREM simulations were performed using MACTEMPASX software based on multislice method [76] and non-linear imaging theory [77]. To obtain a quantitative match between the simulated and experimental images, the HREM imaging conditions, specimen thickness, and tilt were determined by maximizing the normalized cross-correlation coefficient (NCCC) between



the experimental and simulated images. An additional constraint was that the imaging conditions should be physically reasonable taking into account the shape and size of the nanocubes as well as the fact that in an aberration corrected TEM the magnitude of residual aberrations is relatively small. The NCCC is defined as:

$$NCCC = \frac{\sum_i (I_1(i) - \bar{I}_1) \cdot (I_2(i) - \bar{I}_2)}{\sqrt{\sum_i (I_1(i) - \bar{I}_1)^2 \sum_i (I_2(i) - \bar{I}_2)^2}}$$

where the sum is over the pixels in an image motif and the contrast of the experimental and simulated images is normalized to zero mean. Thus the absolute contrast mismatch issue will not contribute in the NCCC.

### 4.3 Results and Discussion

Fig. 4.2(a) shows the general shape of CeO<sub>2</sub> nanocubes. The nanocubes have predominantly the {100} facets exposed while the corners and edges are truncated by {110} and {111} facets. The {110} and {111} facets can be clearly seen when the nanocubes are tilted to the [110] zone axis, as shown in Fig. 4.2(b). Therefore, at the same imaging conditions, the three facets can be imaged simultaneously.

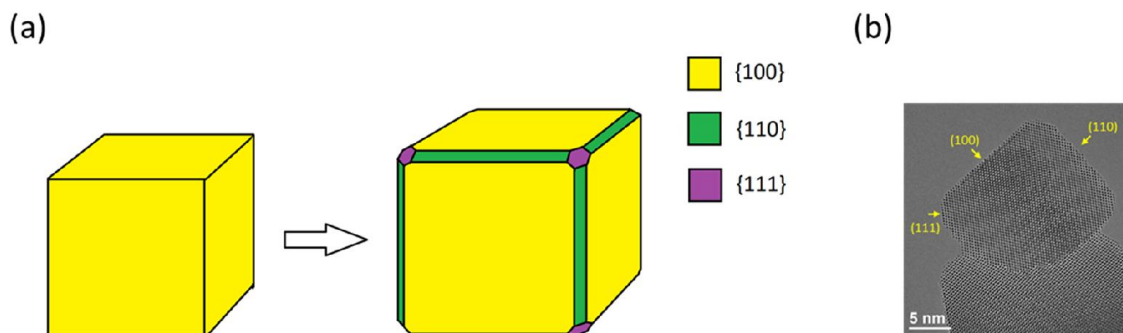


Figure 4.2 Illustration of the exposed facets of CeO<sub>2</sub> nanocubes. (a) Schematic view of the simplified and realistic exposed facets of a CeO<sub>2</sub> nanocube. (b) Experimental TEM image of a CeO<sub>2</sub> nanocube tilted to a [110] zone axis.

#### 4.3.1 {100} surface

Figs. 4.3(a) and (b) show the experimental HREM images of two opposite {100} facets. Figs. 4.3(c)-(h) are the simulated images for the areas indicated by the arrows. The areas I and II in Fig. 4.3(a) show Ce and O terminations respectively, which match well with the simulated images in Figs. 4.3(a) and (d). Therefore, both Ce and O terminations can exist on the same facet. Region III in Fig. 4.3(b) is believed a  $\frac{1}{2}$ O removed CeO termination, which matches with the simulated image using the  $(\sqrt{2} \times \sqrt{2})R45^\circ$  reconstructed CeO model [129] (half of the outermost surface O are removed in a checkerboard style). Regions IV-VI are Ce-terminated surfaces, which matches with the simulated images.

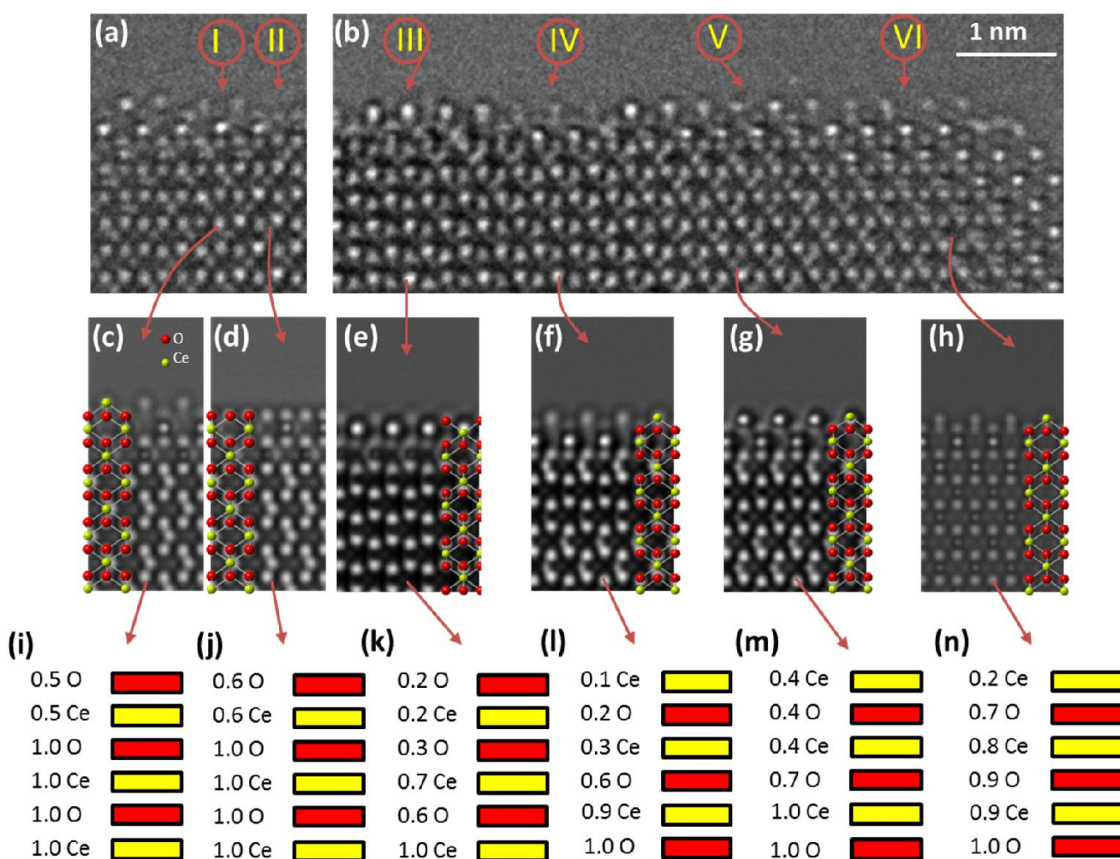


Figure 4.3 Experimental and simulated HREM results of the CeO<sub>2</sub> (100) surface. (a)-(b) Experimental HREM images of two {100} facets on the opposite sides of a CeO<sub>2</sub> nanocube. (c)-(h) The simulated HREM images of the different regions in (a) and (b), as indicated by the arrows. (i)-(n) The occupancies used in the simulation of each simulated HREM image.

A significant feature of the (100) surface is the near surface region has low atomic occupancy. Figs. (i)-(n) are the occupancies used for each atom layers in the simulations. The contrast in HREM images can be qualitatively understood by the electron channeling theory. The intensity of each atom column oscillates as the thickness increasing. The heavier (or denser) the atoms is, the more severe the intensity modulation. Therefore, the Ce columns become black is due to the electron channeling contrast [71] at the thick regions. The contrast of O columns does not change

as fast as that of the Ce columns with respect to the thickness change. Due to the cubic shape, the thickness of the specimen is increasing from right to left of Fig. 4.3(b). In the bulk region, the white contrast of O columns are maintained while the contrast of Ce columns changes from white to black as the thickness increases. The area with low occupancy (at the surface) can be understood as an “effective thin” area. Therefore, the surface Ce columns show white contrast, which is opposite from the bulk counterpart. The low occupancy indicates the high concentration of vacancies.

However, the occupancy values are not exactly correct, which is due to the absolute contrast mismatch problem between the experimental and simulated images [130-132]. The simulated images usually show higher contrast than the experimental images by a factor, usually referred to as the Stobbs factor [132]. It is because some of the incoherent aberrations (image spread, vibration, focal spread, inelastic scattering to mention some) vary and cannot be directly measured at the same time as the images are obtained. Nevertheless, as the thickness and defocus are approximately known, the semi-quantitative trend of the occupancy values should be correct. The low occupancies of the surface atoms are obvious, as the image contrast of the 100% occupied surface are very different from the experiment, as shown in Fig. 4.4. In Fig. 4.4, (a), (b) and (c) are the experimental images, simulated images using low surface occupancies, and simulated images with 100% surface occupancies respectively.

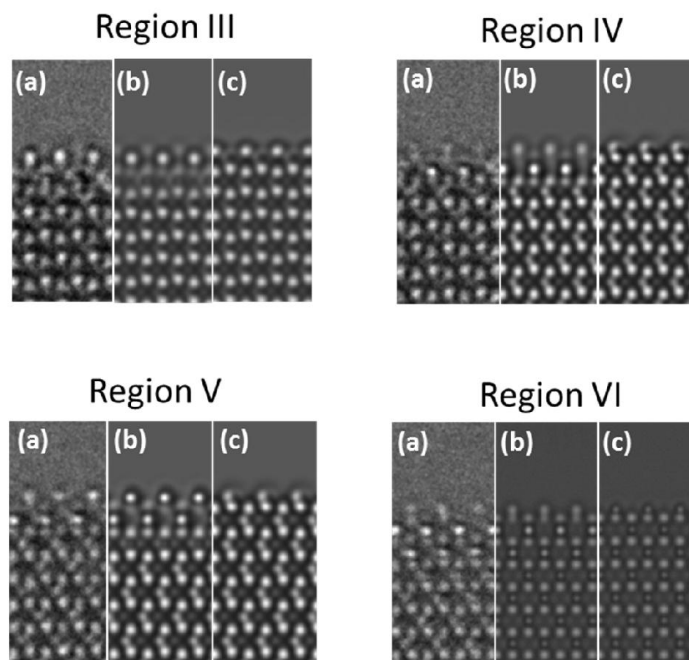


Figure 4.4 Comparison between the partially occupied and fully occupied surface contrast. In Regions III-VI, (a) The cropped experimental images from Fig. 4.3(b). (b) The simulated HREM images using low surface atom occupancies. (c) The simulated HREM images with 100% atom occupancies.

As mentioned,  $\text{CeO}_2$  (100) is a polar surface. However, the expected  $\frac{1}{2}$  O removed surface (the CeO termination) is only observed in a small area. Fig. 4.5 displays the images of the CeO termination area taken at different defocus, which confirms the presence of CeO termination. The presence of different surface terminations on the (100) surface should be attributed to the similar surface energy of the local terminations. For a material with a non-zero temperature, the Gibbs free energy should be considered rather than just the enthalpy. The different terminations result in the increase of entropy. As  $G=H-ST$ , the Gibbs free energy can be lower at the non-zero

temperature with multiple surface terminations, even some surface configurations have slightly lower energy than others.

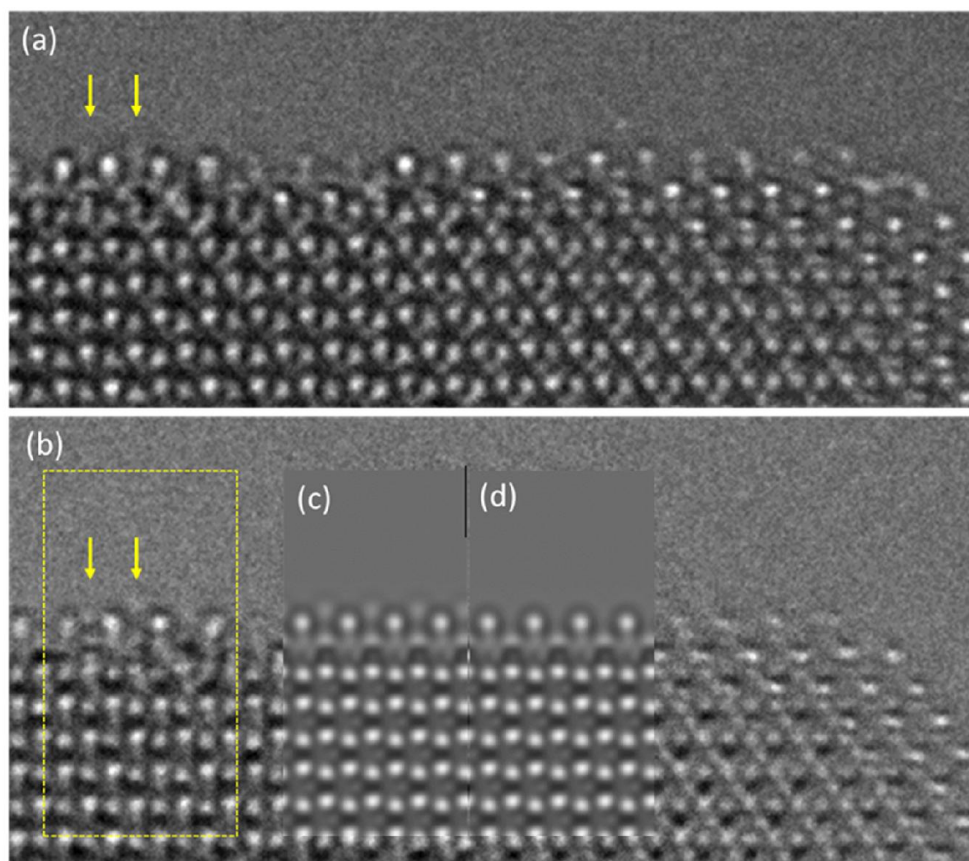


Figure 4.5 HREM images taken at two different defocus. (a) The same image as in Fig. 4.3(b). (b) The image taken at a defocus  $\sim 1.5$  nm less than (a). The arrows indicate O atoms. (c) A simulated HREM image for the area in the yellow box in (b) using the reconstructed CeO-terminated surface. (d) A simulated HREM image using the same condition as in (c) but with a Ce termination.

Another feature of {100} surfaces observed in this study is the hopping of atoms on the surface, which is in agreement with previous HREM studies of CeO<sub>2</sub> nanoparticles [127, 128]. The surface atoms diffuse on the surface (see Supporting Information), which results in random and unpredictable surface atomic rearrangements. However, similar features to Figs. 2b,e are present in almost all of our HREM images. Therefore, this single image represents the general features on the surface. The electron beam intensity was reduced (from  $4 \times 10^3$  e/Å<sup>2</sup>s to  $5 \times 10^2$  e/Å<sup>2</sup>s) to probe electron beam effects on the surface diffusion; however the surface hopping seems to be unavoidable. To identify whether the mixed terminations of CeO<sub>2</sub> (100) are intrinsic or electron beam induced, infrared spectroscopy experiments were conducted, and their results will be presented in the discussion section.

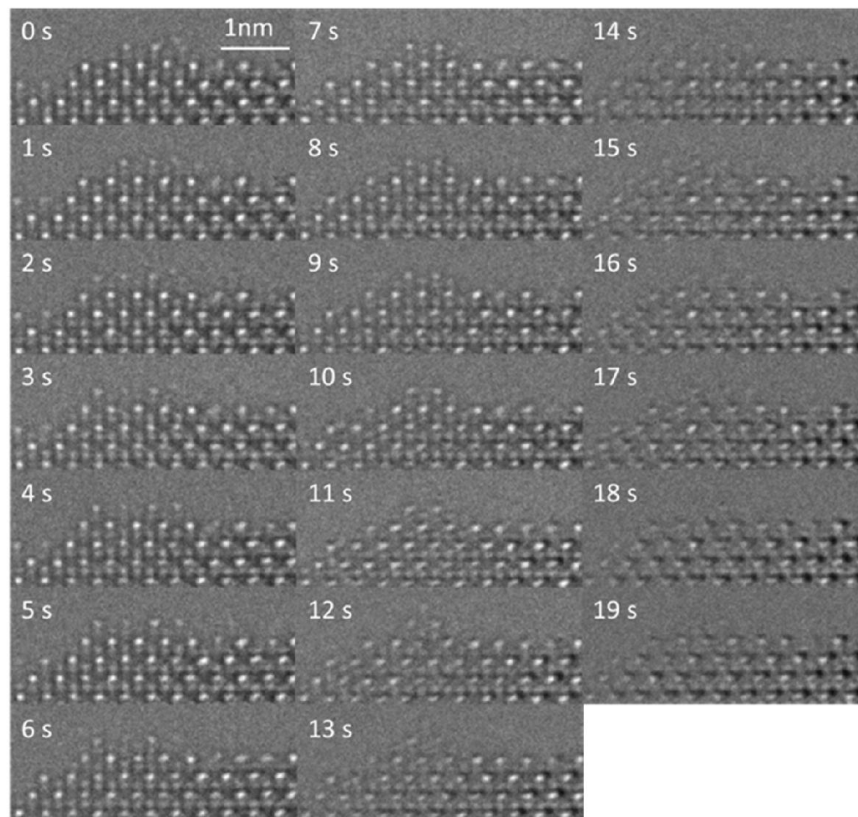


Figure 4.6 Time series of HREM images show the atomic diffusion of  $\text{CeO}_2$  (100) surface, recorded at a time interval of 1 s. For the series of images, the bright spots are atoms.

### 4.3.2 (111) Surface

Fig. 4.7(a) shows the experimental HREM image of a  $\text{CeO}_2$  (111) surface. The imaging condition are similar to the previous case: the white spots are atoms. Fig. 4.7(b) and (c) are simulated HREM images with an O-terminated and Ce-terminated surface respectively. Clearly, the simulated image with an O-terminated surface model matches with the experiment much better than the Ce-terminated one. The experimental and simulated images with O-terminated (111) surfaces show the outmost layer consists of dim white spots. According to the electrostatic consideration, the O-terminated surface is stable while the Ce-terminated surface is a type-III



polar surface. Therefore, the O-terminated (111) surface is expected. Studies on CeO<sub>2</sub> single crystals show that the (111) surface is O-terminated as well [110, 133]. In addition, under a certain reduction condition, the sub-surface O vacancies are observed to be stable [123, 124]. In this profile-view HREM study, the overall contrast of O column is not very sensitive to the vacancies. No definitive conclusion of sub-surface O vacancies can be made.

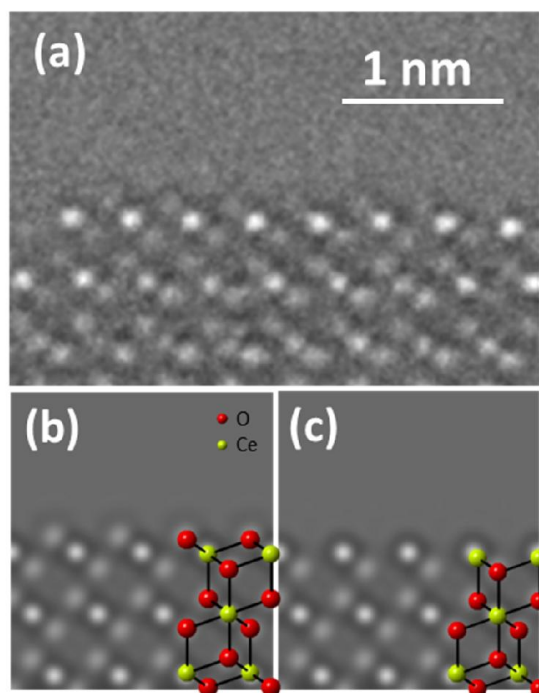


Figure 4.7 (111) surfaces of a CeO<sub>2</sub> nanocubes. (a) An experimental HREM image on a (111) surface of CeO<sub>2</sub> nanocubes at [110] zone axis. (b) A simulated HREM image of the CeO<sub>2</sub> (111) surface with an O termination. The structural model is overlaid on the atom positions. (c) A simulated HREM image of the CeO<sub>2</sub> (111) surface with a Ce termination.

### 4.3.3 (110) surface

The experimental HREM image of the (110) surface in profile-view is shown in Fig. 4.8(a). All the white spots in the images are atoms. The white spots with stronger intensity are Ce atoms, while the spots with weaker intensity are O atoms. The simulated images using CeO<sub>2</sub>-terminated

and Ce-terminated surface are shown in Fig. 4.8 (b) and (c) respectively. Fig. 4.8(d) shows line-profiles with a width of 7 and 9 pixels drawn from A1 to A2, as indicated in Fig. 4.8(a). The averaged intensity of the vacuum area is treated as a noise level, which is also shown in Fig. 4.8(d). Assuming the unidentifiable intensity of the O atom positions are O vacancies, the CeO<sub>2</sub> (110) contains a large amount of O vacancies. In addition to the flat (110) termination, the “sawtooth-like” features are also presented on the surface, as indicated by the white arrows in Fig. 4.8(a). The “sawtooth-like” features are identified as the (111) nanofacets. Therefore, the (111) nanofacets and CeO<sub>2-x</sub> terminations coexist on the (110) surface.

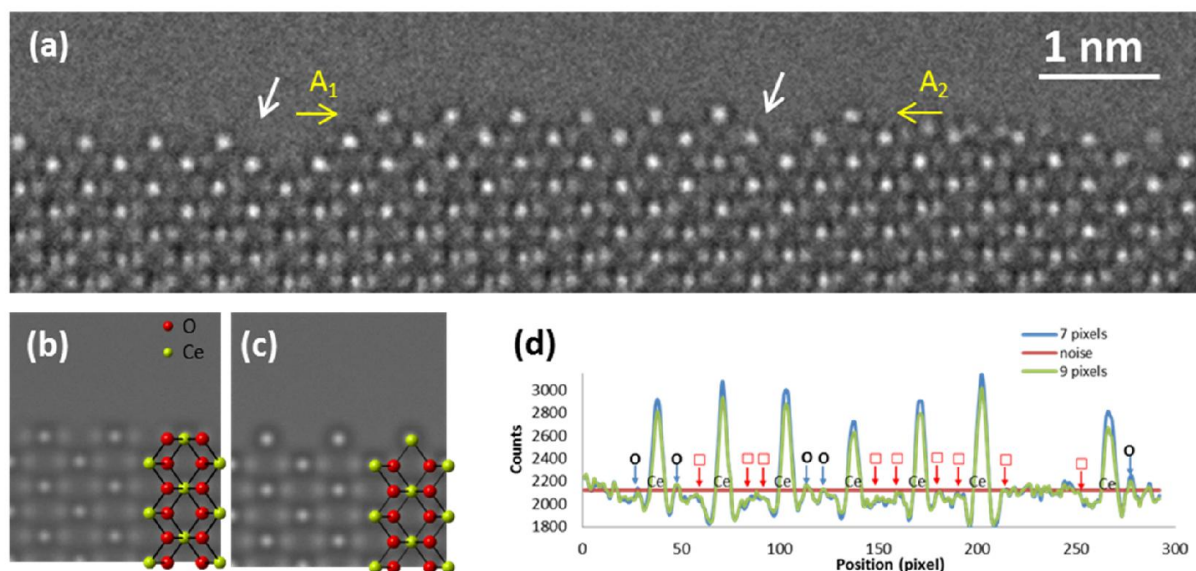


Figure 4.8 (110) surfaces of CeO<sub>2</sub> nanocubes. (a) An experimental HREM image on a (110) surface of CeO<sub>2</sub> nanocubes at [110] zone axis. The white arrows indicate (111) nanofacets. (b) A simulated HREM image of the CeO<sub>2</sub> (110) surface with a CeO<sub>2</sub> surface termination. The structural model is overlaid on the atom positions. (c) A simulated HREM image of the CeO<sub>2</sub> (110) surface with a Ce termination. (d) Integrated line profiles from A1 to A2 indicated in (a). O vacancies are indicated by the squares (□).

The coexistence of the (111) nanofacets and flat  $\text{CeO}_{2-x}$  indicates the low energy of (111) faceting on the (110) surface. Although both the (110) and O-terminated (111) surfaces are non-polar, DFT studies show that the (111) surface has lower energy than the (110) energy [134-136]. However, the apex of the (111) nanofacets can induce additional energy. Thus the energy of the (111) nanofacets and  $\text{CeO}_{2-x}$  surface is comparable and a coexistence is expected.

The high concentration of O vacancies indicates the low O vacancy formation energy. Based on the intensity profile analysis on the HREM images of three nanocubes, there are approximately 30% oxygen vacancies on the  $\text{CeO}_{2-x}$  part of the (110) surface. The exact value of the oxygen vacancy concentration can vary with the change of O vapor pressure and electron beam irradiation. Nevertheless, as the imaging conditions for the (100), (110) and (111) surfaces are similar, the ratio indicates the relative ease of oxygen vacancies formation compared to the  $\text{CeO}_2$  (111) surface.

#### **4.3.4 IR Spectroscopy**

The IR spectroscopy experiment was conducted by Dr. Zili Wu et al. at Oak Ridge National Laboratory [53]. The HRTEM study shows reproducible results on several different nanoparticles. However, much larger quantities of nanoparticles are required for catalytic tests. In addition, the surface structures are observed under electron beam irradiation. To further confirm whether the observed surface structures are presented intrinsically on the majority of the nanoparticles, IR studies were conducted. The IR spectroscopy analysis on the structures of different facets is simplified greatly by using nanostructures with well-defined shapes. In particular, the nanocubes, nanooctahedra and nanorods were assumed to have predominately

{100}, {111}, and {110} facets exposed, respectively. In the IR study, pulses of gas phase methanol molecules in He were delivered to the nanostructures at room temperature. The methoxy species were adsorbed on the nanostructures and the IR spectra were recorded continuously. The recording was stopped when the IR spectra showed no further changes. The final steady state IR spectra were analyzed quantitatively.

Four general adsorption modes of methoxy on the surfaces of CeO<sub>2</sub> can be characterized at the C-O and C-H stretch regions: on-top methoxy (Type I), bridging methoxy (Type II), bridging methoxy with surrounding surface O vacancies (Type II'), and 3-coordinate methoxy (Type III). The composition of each adsorption modes for CeO<sub>2</sub> nanostructures is shown in Table 2. The numbers in black are the experimentally measured values while the numbers in red indicate the composition of each adsorption mode on the ideal CeO<sub>2</sub> surfaces. For example, it is expected that on-top methoxy species can be formed upon dissociative adsorption of methanol on the rods and octahedra, as the 7-coordinate Ce on the (111) surface and 6-coordinate Ce on (110) are unsaturated. Indeed, the experimental results show the octahedra with {111} facets only have type I adsorption. The formation of type II and III methoxy species is not possible on the pristine {110} surface, as the nearest spacing between surface Ce atoms is too large for the bridging adsorption (steric hindrance). However, the rods have these types of adsorption in the real situation, which should be attributed to the defected or reconstructed (110) surface. The type II methoxy adsorption is 100% if the (100) surface only has the structure of the ½ O removed CeO surface reconstruction. Type I on-top adsorption on the (100) surface with the CeO reconstruction is not possible due to the steric hindrance of the remaining surface O atoms. However, the experimental measurement shows the presence of all the adsorption modes on the

nanocubes ((100) surface), which are attributed to the defected surface or the surface with local Ce terminations. The IR study indicates only the (111) surface has an ideal O-terminated structure. For the (100) and (110) surface, structures different from the ideal surface terminations are present. Therefore, the conclusion from the IR study matches with the HREM results.

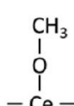
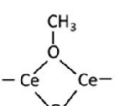
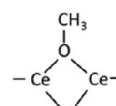
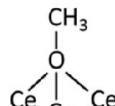
Ceria surfaces	Type I methoxy (percentage)	Type II methoxy (percentage)	Type II' methoxy (percentage)	Type III methoxy (percentage)
				
Rods {110}	1104 - $\nu(\text{CO})$ , 2802 - $\nu_s(\text{CH}_3)$ , 2913 - $\nu_{as}(\text{CH}_3)$ . (100% / 75%)	1047 - $\nu(\text{CO})$ , 2802 - $\nu_s(\text{CH}_3)$ , 2913 - $\nu_{as}(\text{CH}_3)$ . (0% / 3%)	1032 - $\nu(\text{CO})$ , 2802 - $\nu_s(\text{CH}_3)$ , 2913 - $\nu_{as}(\text{CH}_3)$ . (0% / 12%)	1016 - $\nu(\text{CO})$ , 2802 - $\nu_s(\text{CH}_3)$ , 2913 - $\nu_{as}(\text{CH}_3)$ . (0% / 10%)
Cubes {100}	1106, 2817, 2916. (0% / 43%)	1077, 2805, 2923. (100% / 5%)	1037, 2805, 2923. (0% / 40%)	1019, 2805, 2923. (0% / 12%)
Octahedra {111}	1109, 2806, 2913. (100% / 100%)	None	None	None

Table 2 Assignment of IR bands from methanol adsorption on three ceria nanostructures at room temperature. The quantification of each methoxy species is shown in the parenthesis: red numbers represent theoretical value on the ideal surface while black numbers are from IR spectral fitting results (this table is reproduced from ref. [53], with permission from ACS Catal. 2012, 2, 2224–2234. Copyright 2012 American Chemical Society.).

It seems the edges and corners of  $\text{CeO}_2$  nanocrystals are truncated with some minor facets. For example, the {110} and {111} facets are present on the  $\text{CeO}_2$  nanocubes. However, the

contribution of these sites to the total methoxy adsorption should be negligible. TEM study is conducted on 15 individual  $\text{CeO}_2$  nanocubes with sizes ranging from 15 to 100 nm, and found that the size of  $\{111\}$  facets is almost constant. The edge length of the  $\{111\}$  hexagons is  $\sim 1.5$  nm and does not change with the size of a  $\text{CeO}_2$  nanocube. Two examples are shown in Fig. 4.9. With the average edge length of  $\text{CeO}_2$  nanocubes (size value from XRD) being 43 nm, the  $\{110\}$  and  $\{111\}$  facets contribute to less than 7% of the total surface area. In the original IR results, type I, II and III modes contribute to 43%, 45% and 12% of the methoxy adsorption, respectively. If we take the contributions of the minor facets into account, the corrected values of the adsorption mode contribution of type I, II and III would be 40.5%, 47.3% and 12.2% on the  $\{100\}$  facets of the nanocubes, respectively. Hence the multiple adsorption modes do not only arise from the minor facets.

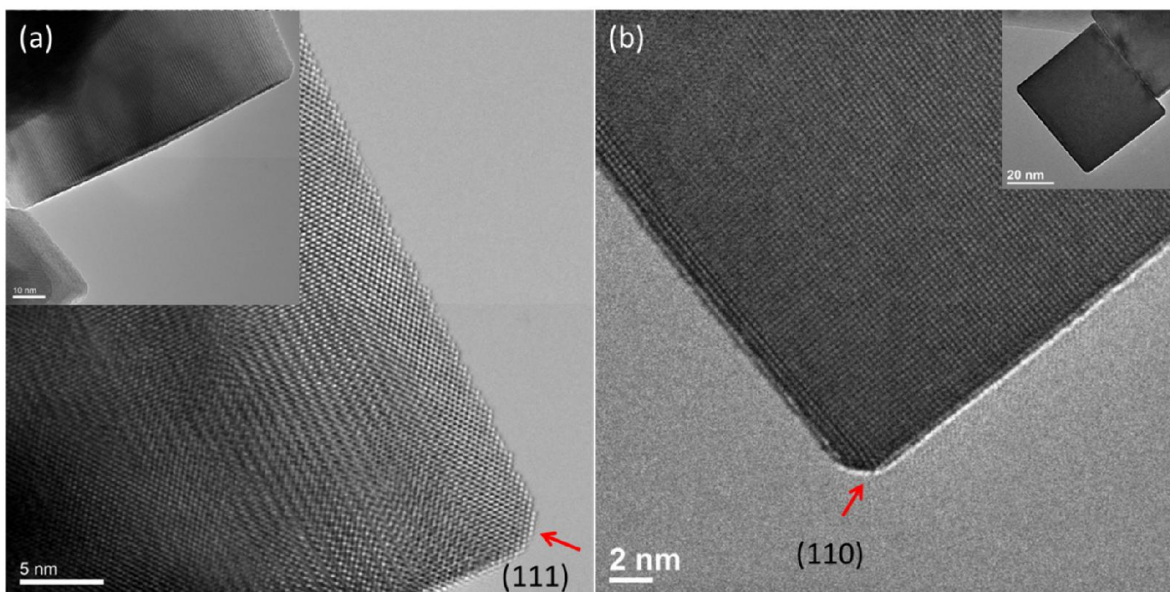


Figure 4.9 Size of  $\{111\}$  and  $\{110\}$  facets. (a) The size of a  $(111)$  facet of a relatively large nanocube ( $\sim 70$  nm edge length). The edge length of the  $(111)$  facet is close to 1.5 nm. (b) The size of a  $(111)$  facet of a nanocube with the size close to the average. The width of the  $(110)$  facet is

close to 1.5 nm too. Note that the width of {110} facets are the same as the edge length of {111} facets.

#### **4.4 Summary**

The atomic surface structures of CeO<sub>2</sub> nanocubes are characterized by aberration corrected HREM and IR spectroscopy. The nanocubes are predominantly the {100} facets exposed. The edges and corners are truncated by the {110} and {111} facets. Under the same imaging condition, the atomic surface structures are distinct. CeO<sub>2</sub> (111) surface is O-terminated. The (110) surface has (111) faceting and reduced CeO<sub>2-x</sub> surfaces. (100) surface has mixed surface terminations with partially occupied near-surface region (~1 nm). Clearly, the electrostatic potential affects surface structures. The density of surface O vacancies indicates the redox properties of the surfaces and sheds lights on the shape-selective catalysis of CeO<sub>2</sub> nanostructures.

## 5. Atomic Surface Structures of Ce<sub>2</sub>O<sub>3</sub> Nanoparticles

### 5.1 Introduction

The redox properties of CeO<sub>2</sub> are of particular interest for its important technological applications. Usually in catalysis or some other applications, CeO<sub>2</sub> can provide O to other reagents (or materials) by creating O vacancies on its surface [35, 137]. The Ce ions neighboring the O vacancies are reduced to Ce<sup>3+</sup> [138]. The reduction starts at the surface of CeO<sub>2</sub>. As the reduction continues, the O vacancies diffuse into the bulk [139]. It is found the O vacancies can form orderings rather easily that the CeO<sub>2</sub> can be reduced to a variety of crystalline CeO<sub>2-x</sub> ( $x \leq 0.5$ ) compounds [140]. A series of intermediate phases (Ce<sub>2</sub>O<sub>3</sub>-CeO<sub>2</sub>) under different temperatures and oxygen vapor pressures has been reported previously [140]. The Ce<sub>2</sub>O<sub>3</sub> and CeO<sub>2</sub> are reported to be the predominant phases over a relatively wide range of O vacancy concentrations [140].

In chapter 4, the atomic surface structures of fluorite phase CeO<sub>2</sub> nanoparticles are discussed. This chapter presents the atomic surface structures of the Ce<sub>2</sub>O<sub>3</sub> nanoparticles, which are a completely reduced form of Ce oxides. Understanding the atomic surface structures of Ce<sub>2</sub>O<sub>3</sub> is important for several reasons. Although Ce<sub>2</sub>O<sub>3</sub> is considered a completed reduced form of CeO<sub>2</sub>, the oxidation state of the surface Ce can be different from the bulk. Understanding the atomic surface structure of the Ce<sub>2</sub>O<sub>3</sub> can help to understand the redox properties of CeO<sub>2-x</sub> at reduction conditions. Furthermore, the bulk and surface structures of Ce<sub>2</sub>O<sub>3</sub> nanoparticles are little known. There are debates on the presence of Ce<sub>2</sub>O<sub>3</sub> [141-143], which is due to the lack of atomic resolution study of the structure. Atomic resolution study can solve the puzzle. In addition,



$\text{Ce}_2\text{O}_3$  can have a bixbyite structure. The structural study of  $\text{Ce}_2\text{O}_3$  can help to understand the structures of other similar materials, such as transparent conductive oxides including  $\text{In}_2\text{O}_3$ .

$\text{Ce}_2\text{O}_3$  is a type of rare earth sesquioxides ( $\text{Re}_2\text{O}_3$ , Re is the rare earth elements including Ce, La, other lanthanides, Sc, and Y). Note that although Ce is called a rare earth element, the abundance of Ce is similar to Cu. The rare earth elements are usually dispersed geologically so that the concentrate minerals are very scarce, which results in the name “rare earth.” The rare earth sesquioxides were found to exhibit 5 distinct crystal structures [144-149]. Below 2273 K, there are three types of rare earth sesquioxides: the A-, B-, and C-type. The A-type is structurally hexagonal with one molecule in each unit cell. The B-type is structurally monoclinic with 6 molecules in each unit cell. The C-type is cubic with 16 molecules in each unit cell. For  $\text{Ce}_2\text{O}_3$ , the A-type type (hexagonal, space group P321) is a stable phase in atmosphere, while the C-type (bixbyite, space group Ia-3) is the unstable phase. Fig. 5.1 shows the structural comparison among the fluorite  $\text{CeO}_2$ , A-type  $\text{Ce}_2\text{O}_3$  and the C-type  $\text{Ce}_2\text{O}_3$  phases. Perrichon et al. have found that the C-type  $\text{Ce}_2\text{O}_3$  can form at 800-900 °C while the A-type  $\text{Ce}_2\text{O}_3$  is formed at temperatures higher than 1000 °C [150]. In terms of the O vacancy concentrations of the different  $\text{CeO}_{2-x}$  phases, the fluorite phase of the composition can be stable for the x value up to 0.15. The C-type phase is stable for the x with an upper limit of 0.34, while the A-type is stable for the x values ranging from 0.5 to 0.47 [140]. The structural similarity between the fluorite and bixbyite phases makes C-type  $\text{Ce}_2\text{O}_3$  more interesting than A-type for catalysis, as many studies indicate  $\text{CeO}_2$  nanoparticles have a portion of C-type  $\text{Ce}_2\text{O}_3$  in the near surface region under reducing conditions [141, 151]. And it is possible the formation of the C-type  $\text{Ce}_2\text{O}_3$  prevents the further reduction (or phase transformation) to the A-type  $\text{Ce}_2\text{O}_3$ .

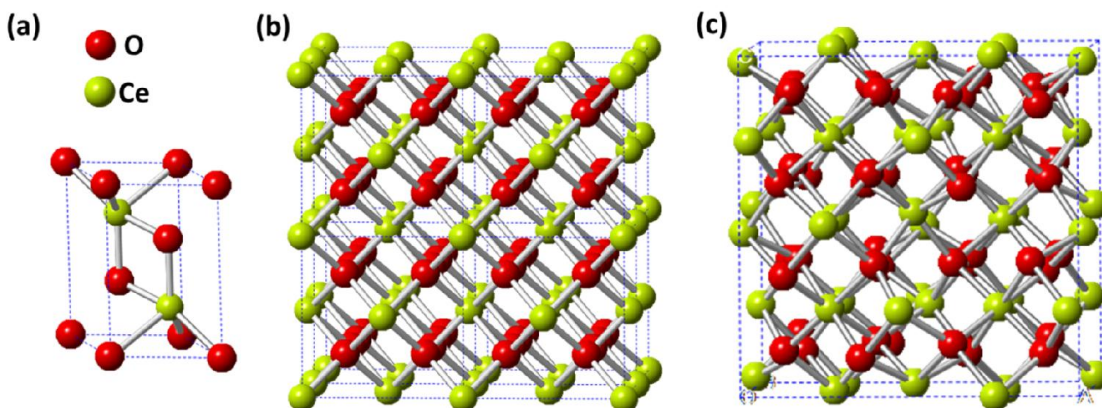


Figure 5.1 Structural models of cerium oxides. (a) The unit cell of A-type  $\text{Ce}_2\text{O}_3$ . (b) a  $2 \times 2 \times 2$  supercell of  $\text{CeO}_2$  unit cells. (c) The unit cell of C-type  $\text{Ce}_2\text{O}_3$ .

Understanding the b- and d-sites of Ce atoms is critical in understanding the bulk and surface structures of the C-type  $\text{Ce}_2\text{O}_3$ . Fig. 5.2 shows the atomic models of the bulk and surface structures of the C-type  $\text{Ce}_2\text{O}_3$ . The C-type  $\text{Ce}_2\text{O}_3$  can be obtained by creating 25% O vacancies in a certain ordering in a  $2 \times 2 \times 2$  fluorite  $\text{CeO}_2$  supercell, as shown in Fig. 5.2(a). The ordering of O vacancies breaks the original symmetry in the fluorite phase. The symmetry equivalent Ce atoms in the fluorite phase become two types of sites. Before relaxation, the Ce atoms are located in the body center of cubic cells made of O atoms and O vacancies, as shown in Fig. 5.2(b). The Ce atoms located in the body center with O vacancies occupying the face diagonal positions are the d-site Ce atoms. The second type of Ce atoms is in the cubic cells with O vacancies occupying the body diagonal positions. The corresponding Ce atoms are the b-site Ce atoms. After lattice relaxation, the b-site and d-site Ce atoms, as well as the O atoms and vacancies deviate from the original positions slightly. In the  $[100]$  direction, the crystal can be considered

as the alternative stacking of d-site Ce layer (Ce-d), O layer (O), and the mixed Ce atoms layer with both d-site and b-site Ce atoms (Ce-m), as shown in Fig. 5.2(c). Thus the (100) can have three distinct bulk truncated terminations, namely the Ce-d, Ce-m, and O terminations. In the [110] direction, the crystal are composed of repeating  $\text{Ce}_2\text{O}_3$  layers with d-site Ce atoms ( $\text{Ce}_2\text{O}_3(\text{Ce-d})$ ) and  $\text{Ce}_2\text{O}_3$  layer with mixed b- and d-site Ce atoms ( $\text{Ce}_2\text{O}_3(\text{Ce-m})$ ), as shown in Fig. 5.2(d). Hence the bulk truncated (110) surface can be  $\text{Ce}_2\text{O}_3(\text{Ce-d})$  or  $\text{Ce}_2\text{O}_3(\text{Ce-m})$  terminations. A significant feature which helps to identify the b- and d-site Ce atom columns in the Ce-d layer is wiggling while the Ce-m layer is flat viewing in the [110] direction, as shown in Fig. 5.2(d). Fig. 5.2(e) shows the atom model of the (111) surface. The bulk truncated (111) surface can have the O termination or mixed Ce termination (Ce-m).

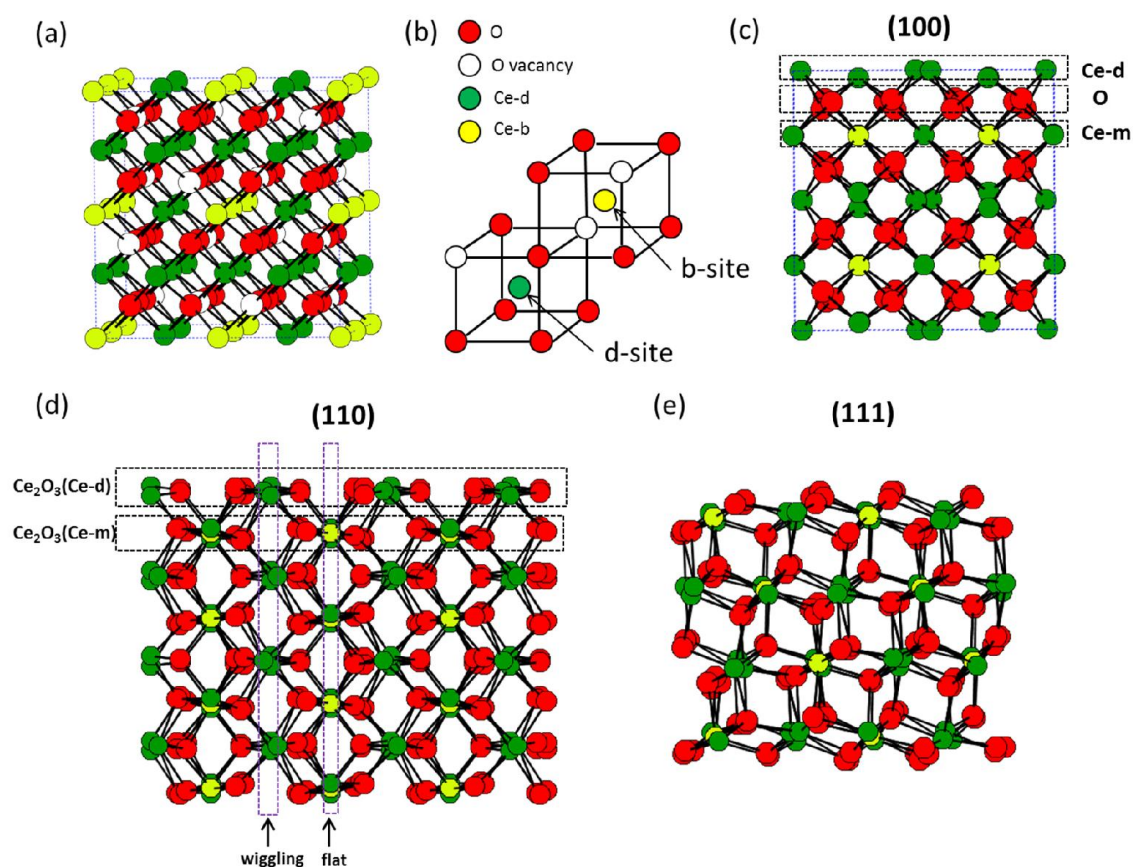


Figure 5.2 Illustration of phase transformation from fluorite  $\text{CeO}_2$  to bixbyite  $\text{Ce}_2\text{O}_3$ . (a) A  $2 \times 2 \times 2$  supercell with  $1/4$  of oxygen atoms missing. (b) The positions of d-site and b-site Ce atoms in C-type  $\text{Ce}_2\text{O}_3$ . (c) The unit cell and (100) surfaces of C-type  $\text{Ce}_2\text{O}_3$ , which is generated after a translation of the origin and relaxation from (a). (d) The atomic model of a (110) surface of C-type  $\text{Ce}_2\text{O}_3$ . (e) The atomic model of a (111) surface of C-type  $\text{Ce}_2\text{O}_3$ .

Similar to the surfaces of  $\text{CeO}_2$ , the stability of the three surfaces can be qualitatively understood using the electrostatic argument as well. The (100) is a polar surface. The O, Ce-d, or Ce-m terminations can lead to an unstable surface. Dipole moment compensation mechanisms such as surface reconstructions are expected to be present. Similar to the  $\text{CeO}_2(100)$ , a possible solution is to remove  $1/2$  O of the O-terminated (100) surface. However, the stability issue is more complicated as removing O atoms at the surface will further reduced the  $\text{Ce}^{3+}$ . The further

reduced Ce ion is an unstable oxidation state. The (110) surface with either  $\text{Ce}_2\text{O}_3(\text{Ce-d})$  or  $\text{Ce}_2\text{O}_3(\text{Ce-m})$  termination is a stable non-polar surface. For the (111) surface, the O terminated (111) surface is a non-polar surface, while the Ce-terminated surface is a polar surface.

## 5.2 Experiment

It has been shown that high temperature reduction [152-154], electron beam irradiation [126], and electric current [155] can all be used to stabilize the C-type  $\text{Ce}_2\text{O}_3$ . In this study, the C-type  $\text{Ce}_2\text{O}_3$  phase is obtained by electron beam irradiation of  $\text{CeO}_2$ . The preparation of  $\text{CeO}_2$  nanoparticles for TEM analysis is described in chapter 4. The operation of HREM imaging is similar to the HREM study on  $\text{CeO}_2$  nanoparticles except for the electron dose used. By increasing the electron dose from  $\sim 10^3 \text{ e}/\text{\AA}^2\text{s}$  to  $10^4 \text{ e}/\text{\AA}^2\text{s}$ , the  $\text{CeO}_2$  nanoparticles were readily transformed to the C-type  $\text{Ce}_2\text{O}_3$ . This process is reversible. Without the electron irradiation, the C-type  $\text{Ce}_2\text{O}_3$  can transform back to the fluorite phase rather quickly, probably by adsorbing the residual O in the TEM column. This is confirmed by other TEM studies. The increase of electron dose was achieved by changing the spot size. The structure of the C-type  $\text{Ce}_2\text{O}_3$  was confirmed by HREM, FFT of HREM, and EELS. The EELS measurement was performed in TEM diffraction mode. The beam was converged slightly to avoid the signals from other nanoparticles.

## 5.3 Results and Discussion

Fig. 5.3 shows the HREM and EELS results of a nanoparticle before and after phase transformation. In the HREM imaging mode, the d-spacing of the C-type  $\text{Ce}_2\text{O}_3$  {200} is lightly larger than that of the {100}  $\text{CeO}_2$ . The FFT mode of the HREM images shows the difference

more clearly. The additional spots in the FFT (the insets in Fig. 5.3 (a) and (b)) indicate the superlattice reflections of the C-type  $\text{Ce}_2\text{O}_3$ . In addition, the relative intensity of the M5 and M4 edges in EELS of  $\text{Ce}^{3+}$  and  $\text{Ce}^{4+}$  are distinct, as shown in Fig. 5.3(c), which can be used to identify the  $\text{Ce}^{3+}$  and  $\text{Ce}^{4+}$  [142]. For the  $\text{CeO}_2$  nanoparticles, the intensity of the M4 edge is larger than the M5 edge. In contrast, the M4 edge has a lower intensity than the M5 edge in the  $\text{Ce}_2\text{O}_3$  nanoparticles. With the lattice pattern, spacing, and the oxidation states confirmed in this TEM analysis, the presence of electron-induced C-type  $\text{Ce}_2\text{O}_3$  nanoparticles is confirmed. For simplicity, the  $\text{Ce}_2\text{O}_3$  will be referred to as the C-type  $\text{Ce}_2\text{O}_3$  without additional notice.

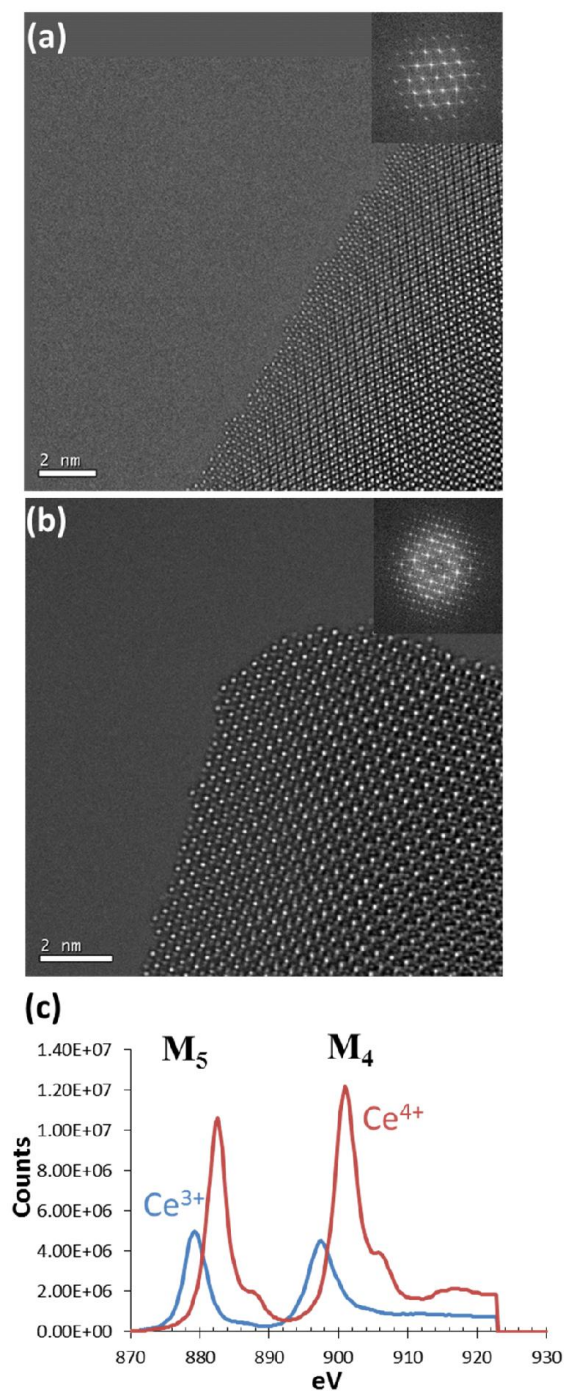


Figure 5.3 Phase transformation from  $\text{CeO}_2$  to C-type  $\text{Ce}_2\text{O}_3$ . (a) A HREM image of a  $\text{CeO}_2$  nanocube. The inset shows the power spectrum. (b) A HREM image of a C-type  $\text{Ce}_2\text{O}_3$  nanocube. The inset shows the power spectrum. (c) EELS shows the difference between  $\text{CeO}_2$  and  $\text{Ce}_2\text{O}_3$ .

### 5.3.1 (100) surface

Fig. 5.4 shows atomic resolution HREM images of a (100) surface of a  $\text{Ce}_2\text{O}_3$  nanoparticle under the [110] zone axis. Fig. 5.4(a) and (b) are successive images in a focal series with 2 nm focal step. Fig. 5.4(a) has a  $\sim 2\text{nm}$  more overfocus than Fig. 5.4(b). The contrast in the HREM are very similar to the  $\text{CeO}_2$  case. At the thin region (left side), both the Ce and O atoms are bright at a small overfocus condition. The Ce columns show up as strong bright spots while the relatively dim spots represent the O columns. Due to the electron channeling, the Ce columns show as black contrast at the thick regions (right side). The contrast of O columns is maintained, although the intensity is higher (brighter) at the thick regions (right side).

The Ce-d and Ce-m (100) layers can be differentiated by the wiggling and flat spot configurations in the HREM images, as indicated in Fig. 5.4(a). The wiggling layer, as indicated by the green line, corresponds to the Ce-d layer. The flat layer corresponds to the Ce-m layer. On the surface, O atoms can be observed clearly, as indicated by region 2 in Fig. 5.4(a). Region 2 can be considered as the  $\frac{1}{2}$  O removed reconstruction. The local surface stoichiometry is  $\sim \text{Ce}_4\text{O}_3$ . Fig. 5.4(c)-(e) show the simulated images using O-,  $\text{Ce}_4\text{O}_3$ - and Ce-terminated surface models, respectively. Fig. 5(d) matches the experimental contrast in region 2 well. Beneath the O layer is the Ce-m layer with a few dangling Ce-d atoms. However, the Ce-m termination can exist on other nanoparticles. This point will be discussed later. The surface O layer has a large amount of O vacancies, as indicated by region 1 in Fig. 5.4(a). The simulated image with an O-terminated surface (Fig. 5.4(c)) shows a very different contrast from that in the experimental image. In addition, there are dangling Ce atoms on the surface, as indicated by the yellow arrows. Moreover, the surface Ce atoms appear as bright spots while the bulk Ce atoms appear as black



spots at the thick regions. This is again similar to the (100) surface of CeO<sub>2</sub> nanoparticles. The large quantity of Ce vacancies on the surface results in the HREM contrast on an effective thin region. The comparison between the simulated HREM images with 50% occupied and 100% occupied surface models is shown in Fig. 5.5. The simulation from the 50% occupied surface matches with the experimental image much better. The large amount of O and Ce vacancies indicates the exposure of subsurface layer to the vacuum. Therefore, the (100) surface has multiple terminations.

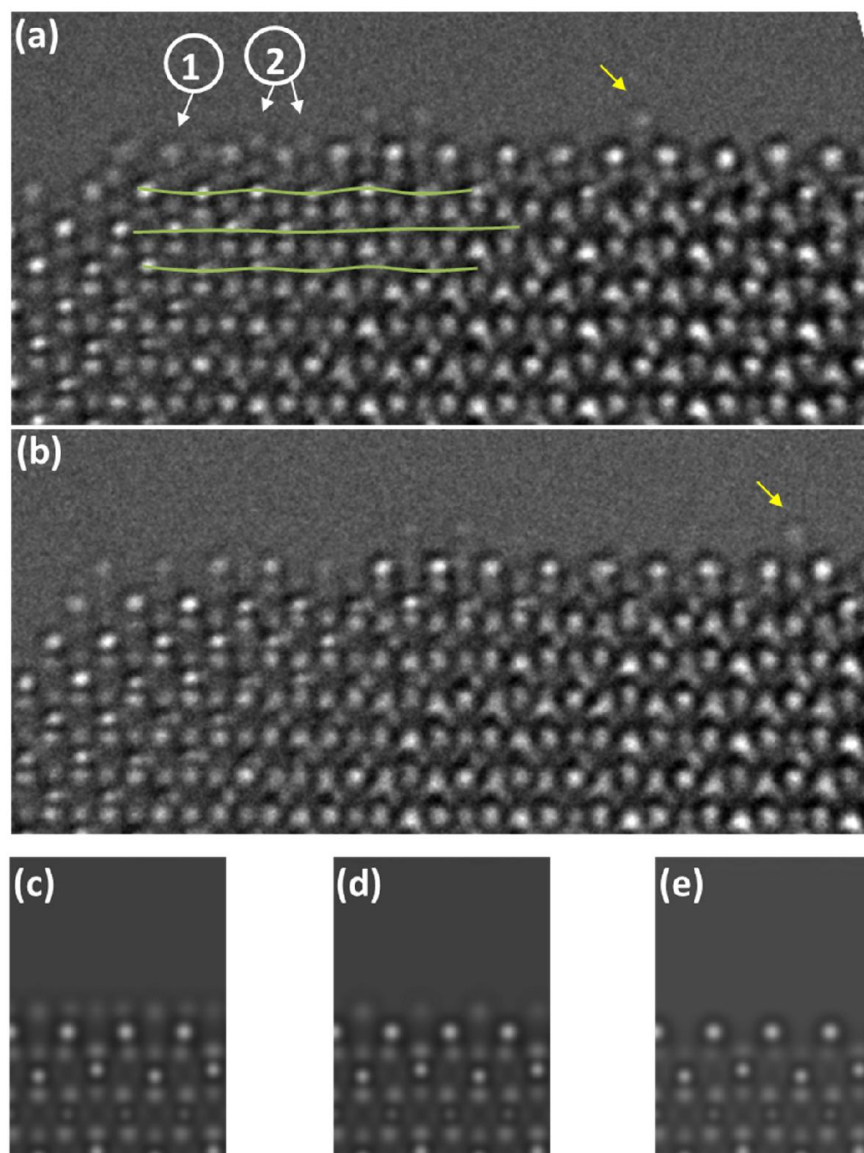


Figure 5.4 Experimental and simulated HREM images of a  $\text{Ce}_2\text{O}_3$  (100) surface. (a) and (b) Two experimental HREM images taken with a 2 nm difference in defocus. (c)-(e) The simulated HREM images using a O-,  $\text{Ce}_4\text{O}_3$ -, and Ce-terminated surface model respectively.

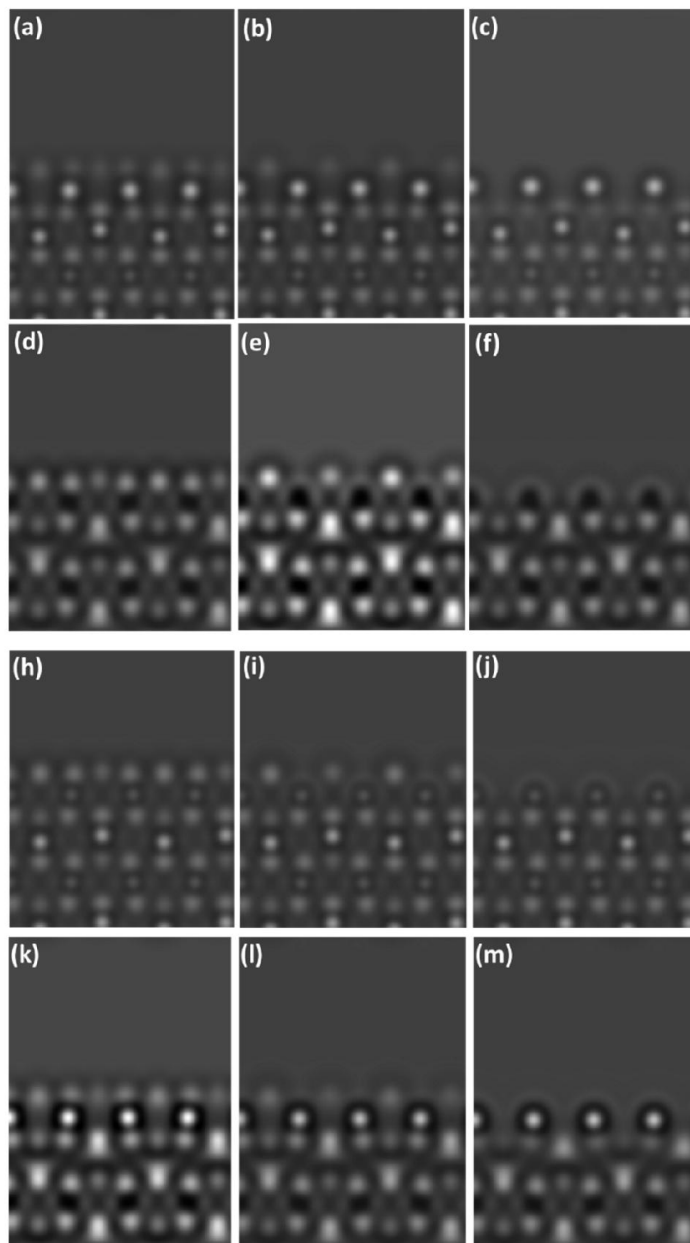


Figure 5.5 Comparison between the partially occupied and fully occupied surface contrast. (a), (d),(h),(k) Simulated HREM images using a O-terminated (100) surface model. (b),(e),(i),(l) Simulated HREM images using a  $\text{Ce}_4\text{O}_3$ -terminated model. (c),(f),(j),(m) Simulated HREM images using a Ce-terminated model. Imaging conditions: (a)-(f) Simulated HREM images with the specimen thickness of 6 nm and defocus of 1 nm. (h)-(m) Simulated HREM images with the specimen thickness of 12 nm and defocus of -2 nm. 50% atomic occupancies were used for the outmost two surface layers in images (a), (b), (c), (h), (i), and (j). 100% atomic occupancies were used for the outmost two surface layers in images (d), (e), (k), (k), (l), and (m).

Similar to the  $\text{CeO}_2$  (100) surface, the surface is rather mobile, especially for the dangling atoms. The surface atom positions in each time-series or focal series images with the 1s exposure time are different. In addition, the diffusion of surface atoms is random. Thus, the multiple surface terminations observed in Fig. 5.4 is representative.

The multiple surface terminations are expected to lower the surface energy. The  $\text{Ce}_2\text{O}_3$  (100) surface is a polar surface. In principle, the polarity is reduced by having a not well-defined (001) surface. In addition, the locally  $\frac{1}{2}$  O removed surface reconstruction is a simple way to maintain the stoichiometry of the whole  $\text{Ce}_2\text{O}_3$  crystal, as well as to compensate the dipole moment. However, the stoichiometry can be changed by the surrounding conditions. Although DFT studies on the surface energies of different terminations of  $\text{Ce}_2\text{O}_3$  are still not available, DFT studies on the similar material  $\text{In}_2\text{O}_3$  show the lowest surface energy structures depend on the O chemical potential [156]. The metallic (001) surface can exist in a wide range of reduction conditions [157]. Therefore, the presence of Ce terminated surfaces under the strong electron beam irradiation is reasonable. Moreover, the coexistence of different surface terminations increases the entropy of the surface, which can reduce the surface Gibbs free energy. The STM study on  $\text{In}_2\text{O}_3$  (001) also indicates the surface is rough under sputtering and annealing [158]. Both the Ce- and  $\text{Ce}_3\text{O}_4$ -terminated surface indicates there are surface Ce atoms with the oxidation state lower than 3+. The stable oxidation states of Ce are believed to be 3+ and 4+. Therefore, it is possible for a competing mechanism for lowering energies of the electronic and atomic structures.

The Ce-d and Ce-m surface terminations can coexist as well. Fig. 5.6 shows the HREM images on a different nanoparticle. Both the top and bottom surfaces show the termination surface is at

the Ce-d layer. This could be due to two reasons. There is only a slight difference between the two surface terminations. The energies of the two terminations should be similar, which can be indicated by the DFT calculations on the  $\text{In}_2\text{O}_3$  (100) surface [156]. Secondly, the Ce-d and Ce-m are defined in the bulk crystal based on the position of O vacancies. If the position of O vacancies changes, there should not be a well-defined Ce-d or Ce-m surface. The multiple surface terminations with a large amount Ce and O vacancies result in the exact Ce-d and Ce-m trivial.

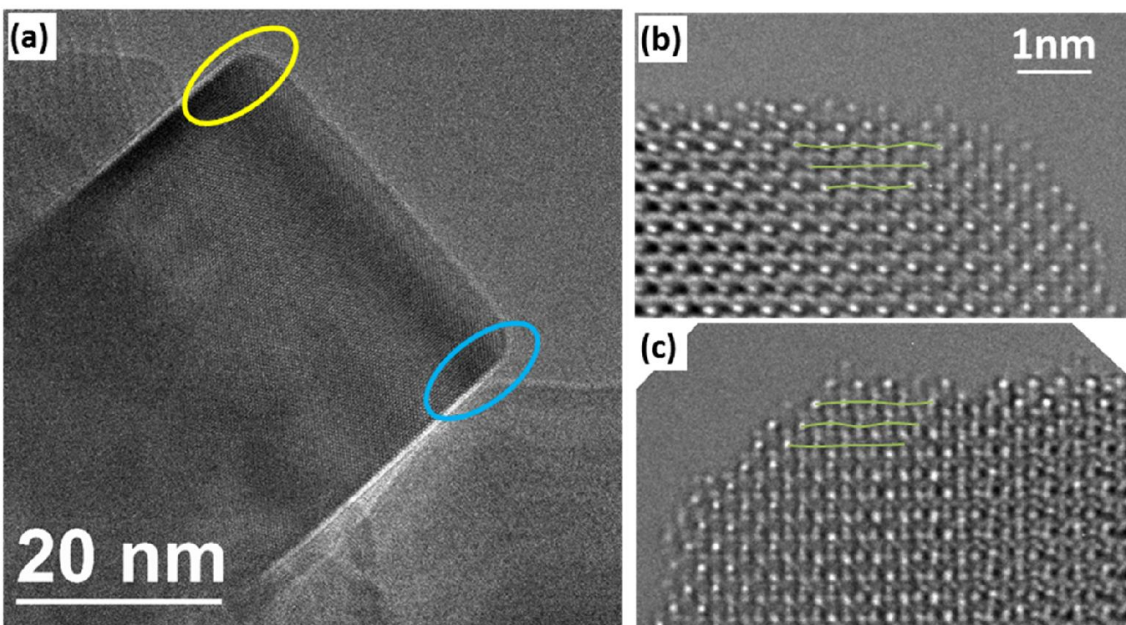


Figure 5.6 Surfaces of another  $\text{Ce}_2\text{O}_3$  nanoparticle with the surface cation layer as Ce-d.

### 5.3.2 (110) surface

Fig. 5.7(a) and (c) show experimental HREM images of the (110) surface of a  $\text{Ce}_2\text{O}_3$  nanocube taken at a small overfocus. As the (110) facet is very thin for the nanocubes, the weak phase object approximation (WPOA) is approximately valid. Therefore, both Ce and O atoms appear as white contrasts. Along the [001] direction, flat Ce layers, wiggling Ce layers and oxygen layers can be directly identified, the atomic model is overlaid in Fig. 5.7(a). As a result, the (110) surface of  $\text{Ce}_2\text{O}_3$  can be clearly interpreted. Initially, the surface contains a mixture of flat  $\text{Ce}_2\text{O}_3(\text{Ce-d})$  layer and “sawtooth-like” (111) nanofacets, as shown in Fig. 5.7(a). Fig. 5.7(b) shows a simulated HREM image of  $\text{Ce}_2\text{O}_3(\text{Ce-d})$  terminated (110) surface, which agrees with the corresponding experimental contrast well (the flat  $\text{Ce}_2\text{O}_3$  layer part). Under continuous electron beam irradiation, the surface atoms were hopping. Approximately 50 seconds after Fig. 5.7(a) was taken, the (110) surface was observed to be more flat. A typical image is shown in Fig. 5.7(c), which was taken 64s after Fig. 5.7(a) was taken. Although the “sawtooth-like” (111) nanofacets were still present, they mostly contained only a single dangling Ce column in comparison to the nanofacets with a width of  $\sim 1$  nm as in Fig. 5.7(a). In addition, the flat layer became predominantly terminated by a  $\text{Ce}_2\text{O}_3(\text{Ce-m})$  layer. A simulated HREM image with  $\text{Ce}_2\text{O}_3(\text{Ce-m})$  termination is shown in Fig. 5.7(d).

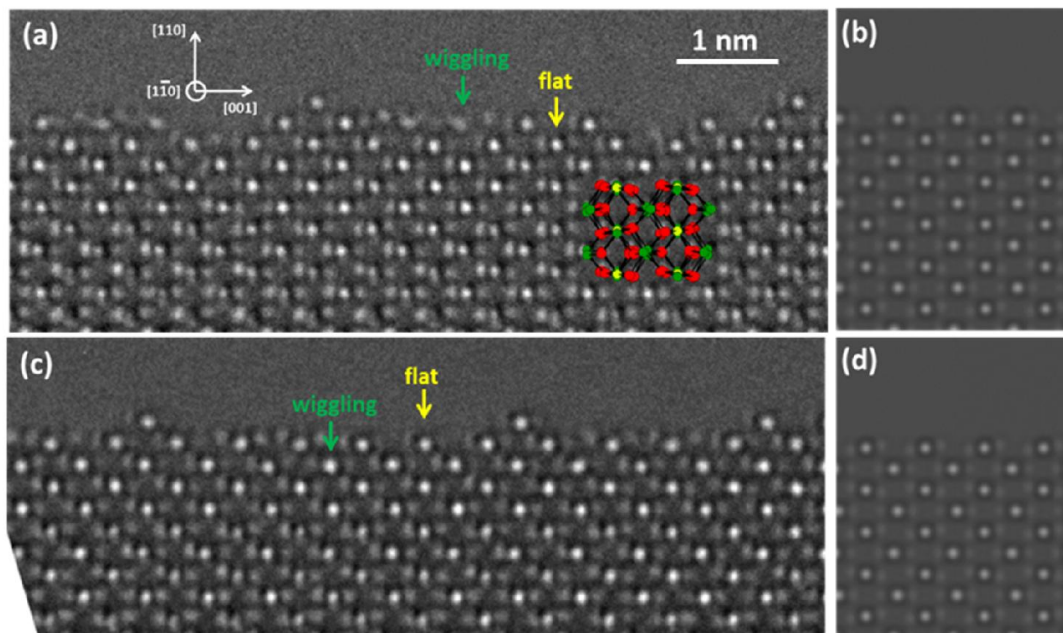


Figure 5.7 Atomic structures of the  $\text{Ce}_2\text{O}_3$  (110) surface. (a) The original HREM image of the  $\text{Ce}_2\text{O}_3$  (110) surface. (b) A simulated HREM image of (a) with a  $\text{Ce}_2\text{O}_3(\text{Ce-d})$  termination. (c) A HREM image after 64s of continuous electron beam irradiation since (a) was recorded. (d) A simulated HREM image of (c) with a  $\text{Ce}_2\text{O}_3(\text{Ce-m})$  termination.

The dynamical process was recorded by time-series images with a 1s exposure time. Fig. 5.8 shows a step-by-step diffusion of surface atoms, which results in the exposure of the subsurface. The surface Ce atom (column), as indicated by the yellow arrows at 33s and 34s, diffused away from the original position. At 35s and 36s, the Ce atom next to the vacant Ce position left by the first diffused Ce atom were migrating to an apex position to form a (111) nanofacet. The Ce atom at the apex position diffused away at 43s.

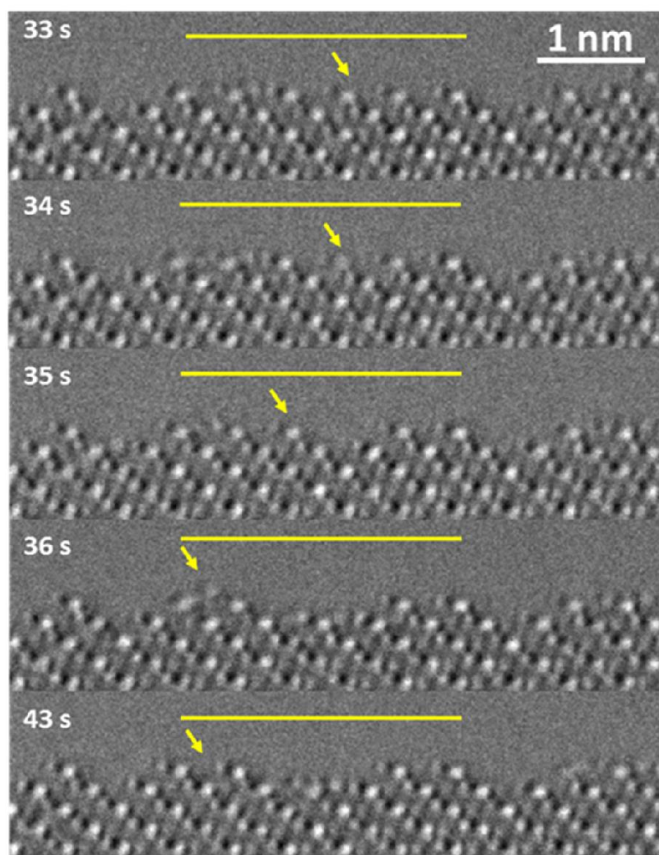


Figure 5.8 Evolution of C-type  $\text{Ce}_2\text{O}_3$  (110) surface from a  $\text{Ce}_2\text{O}_3(\text{Ce-d})$  layer termination to a  $\text{Ce}_2\text{O}_3(\text{Ce-m})$  layer termination. The images were selected from a time-series of 50 images with 1 s interval.

The step-by-step diffusion process can be understood better with O atoms clearly imaged. Fig. 5.9 shows two examples of the role of surface O vacancies in the surface diffusion process. At 55s, a surface Ce atom (column) was bonded to two surface O atoms. The O atoms were successively removed at 79s and 89s. The remaining Ce atom became unstable and diffused away. The images from 130s to 138s show a similar process. At 130s and 134s, the surface Ce



atom was bonded to a surface O. At 137s, the neighboring O atom diffused away. At 138s, the remaining Ce atom diffused away and the subsurface of the Ce atom became the surface.

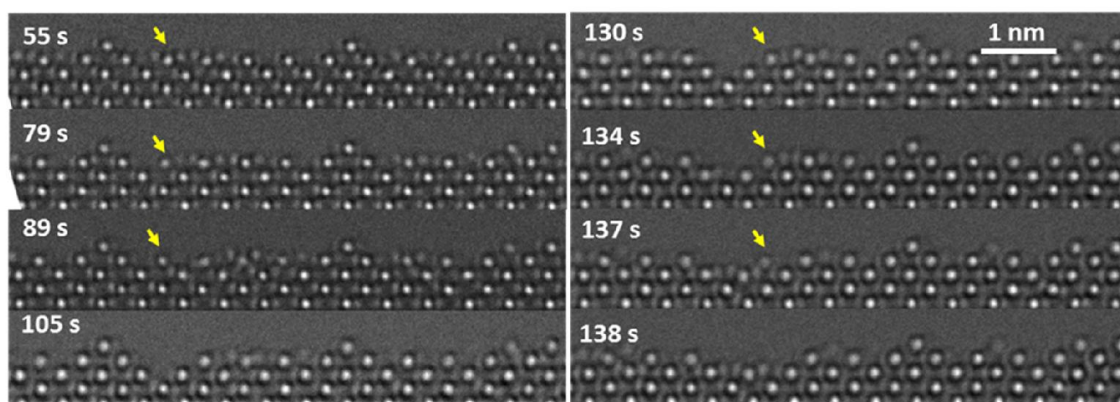


Figure 5.9 Evolution of C-type  $\text{Ce}_2\text{O}_3$  (110) surface from a  $\text{Ce}_2\text{O}_3(\text{Ce-m})$  termination to a  $\text{Ce}_2\text{O}_3(\text{Ce-d})$  layer termination. The images were selected from another time-series of 50 images with 1s interval.

The coexistence of the “saw-tooth” (111) facet and the flat  $\text{Ce}_2\text{O}_3$  terminations should be related to the surface energy and kinetics. Although no reports on the comparison of the surface energies of the (100), (110), and (111) could be found, DFT studies on similar materials such as  $\text{In}_2\text{O}_3$  or  $\text{CeO}_2$  suggest the (111) surface has a lower surface energy compared to that of the (110) surface. Thus, the formation of the (111) nanofaceting is reasonable. However, the apex atoms on the (111) usually lead to a higher surface energy. As the  $\text{Ce}_2\text{O}_3$  nanocube phase transformed from a  $\text{CeO}_2$  nanocube, it probably inherit the (111) nanofacets probably from the  $\text{CeO}_2$  (110) surface. It is possible the flat (110) surface has a slightly lower surface energy than the one with (111) nanofacets, as the flat configuration can last under intensive electron beam irradiation fairly long (~50s) in this study. Probably the flat (110) surface is energetically more favorable while the

(111) nanofacets are in metastable states. With enough activation energy, the flat (110) surface can be formed by eliminating the “saw-tooth” (111) facets. The morphology change of the (110) surface was observed by an environmental TEM study [152]. In the TEM study, a “rumpled”  $\text{CeO}_2$  (110) surface with (111) nanofacets was formed initially and the surface became flat after 600 °C annealing in 0.5 Torr of  $\text{H}_2$ .

The removal of the (110) surface in a layer-by-layer mode should be related to the similar surface energies of the  $\text{Ce}_2\text{O}_3(\text{Ce-m})$  and  $\text{Ce}_2\text{O}_3(\text{Ce-d})$  terminations. The initial termination of the  $\text{Ce}_2\text{O}_3(\text{Ce-m})$  was observed in other nanocubes, as shown in Fig. 5.10(a). In addition, the two surface structures of the two terminations indicate similar surface energies as well. Fig. 5.10(b) and (c) show the plan-view atomic models of the two terminations. Considering the unit area in the blue boxes, the coordination number of Ce atoms is exactly the same. The only obvious difference arises from the configuration of two oxygen atoms bonded to the Ce(4c) atoms. Thus, the energy difference of the two surface terminations should be small. Bond valance calculation was performed for the two bulk truncated surfaces and found the bond valance summation of surface atoms to be very similar. Although the  $\text{Ce}_2\text{O}_3(\text{Ce-m})$  termination is slightly better, deviation from a perfect bulk truncated surface (such as oxygen vacancies) can easily overcome the difference. DFT calculation on the similar material  $\text{In}_2\text{O}_3$  also show that the energy difference between the  $\text{In}_2\text{O}_3(\text{In-m})$  and  $\text{In}_2\text{O}_3(\text{In-d})$  is negligible [156]. Therefore, the observation of both initial terminations is expected.

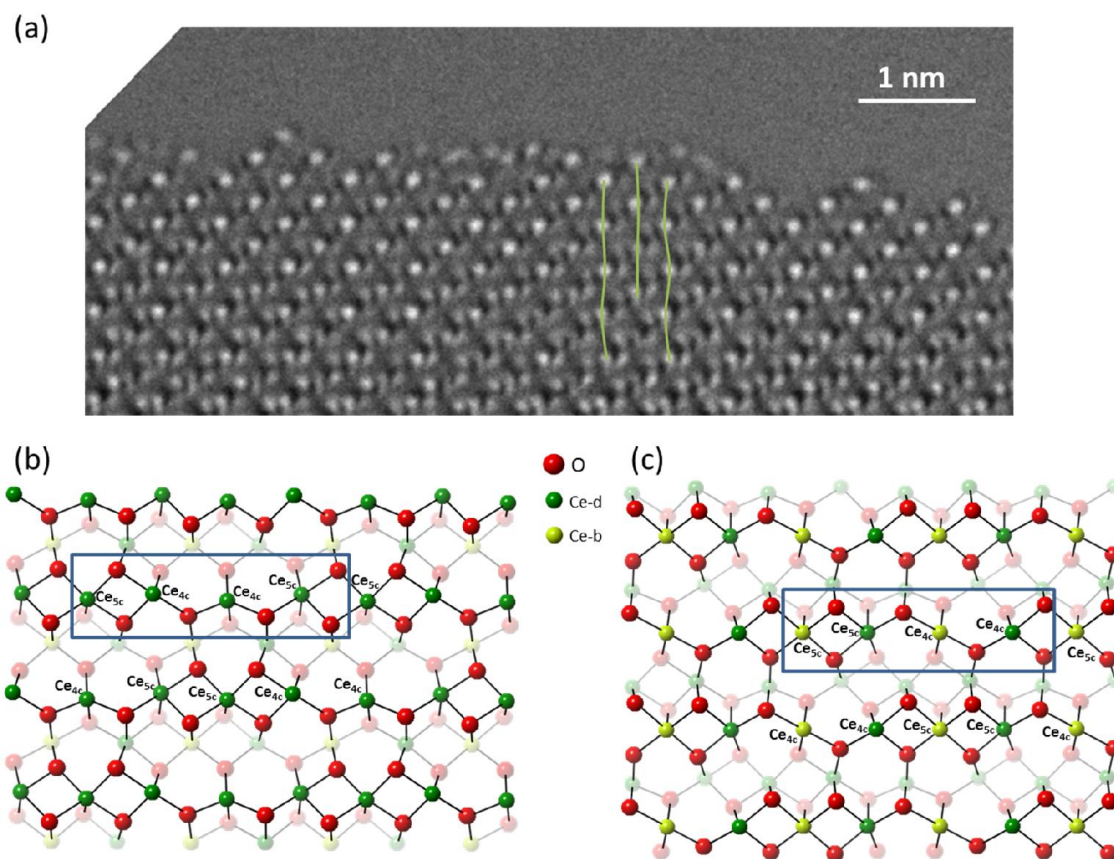


Figure 5.10 Comparison of  $\text{Ce}_2\text{O}_3$ (Ce-m) and  $\text{Ce}_2\text{O}_3$ (Ce-d) surface terminations. (a) A (110) surface shows an initial termination of the  $\text{Ce}_2\text{O}_3$ (Ce-m). (b) Surface structure of  $\text{Ce}_2\text{O}_3$ (Ce-d). (c) Surface structure of  $\text{Ce}_2\text{O}_3$ (Ce-m). The blue boxes indicate unit cells of the two surfaces. The coordinations of each Ce atoms in the unit cell is indicated.

It is reasonable for the O vacancies to be created before the diffusion of neighboring Ce atoms. The rows of atoms in Fig. 5. 10(b) and (c) are the atom columns in profile view under the [110] zone axis. For both terminations, the rows of Ce atoms are only bonded to surface and subsurface oxygen atoms. The surface Ce rows are relatively independent from other surface Ce rows. If the surface oxygen atoms bonded to the surface Ce atoms are removed, the dangling Ce atoms are unstable and can easily diffuse away. This is very similar to other diffusion processes, such as

dislocation. In most cases, it is energetically more favorable for successive atom-by-atom diffusion than the diffusion of a few atoms together. In this case, the diffusion of O atoms requires breaking fewer bonds than the diffusion of Ce and O atoms together, which corresponds to lower activation energy of diffusion.

The typical process of the (110) surface evolution has become clear. It can be considered as the surface is layer-by-layer removed by the electron beam. Oxygen vacancies are first created by the electrons. The surface Ce atoms not bonded to oxygen become mobile and induce additional (111) nanofacets. At later stages of irradiation, Ce atoms at the apex of the (111) nanofacets are unstable and diffuse away. The Ce atoms belonging to the initial outermost layer probably migrate to other facets that are not exposed to the electron beam. At the area without electron beam irradiation, the dangling Ce atoms can trap residual oxygen atoms in the TEM chamber and y app="EN" db-id="9p0rzvp05e, it is likely that the evolution of Ce<sub>2</sub>O<sub>3</sub> (110) is sustainable. However, owing to the shape of the nanocubes in this case, the area of the (110) subsurface is larger than that of the surface. The alternating exposure of Ce<sub>2</sub>O<sub>3</sub>(Ce-d) and Ce<sub>2</sub>O<sub>3</sub>(Ce-m) is expected to slow down with the increasing surface area.

### 5.3.3 (111) surface

Fig. 5.11(a) shows an experimental HREM image of Ce<sub>2</sub>O<sub>3</sub> (111). Due to the cubic shape of the Ce<sub>2</sub>O<sub>3</sub> nanoparticle, the (111) facet is very small and thin under the [110] zone axis. At a small overfocus condition, the bright spots in Fig. 5.11(a) are atoms. The Ce columns show up as strong bright spots while the relatively dim spots represent the O columns. Fig. 5.11(b) shows the simulated HREM image using an O-terminated (111) surface model, which matches with the experimental contrast reasonably well. The experimental contrast is very different from the

simulated image based on the Ce-terminated (111) surface model, as shown in Fig. 5.11(c). The experimental result is consistent with the electrostatic predictions. The O-terminated surface is a non-polar surface while the Ce-terminated (111) is a polar surface. Thus, the O-terminated surface is expected. The (111) surface is relatively more stable than the (100) and (110) surfaces under the intense electron beam irradiations. No significant changes can be observed during continuous imaging, which indicates the stability of this facet.

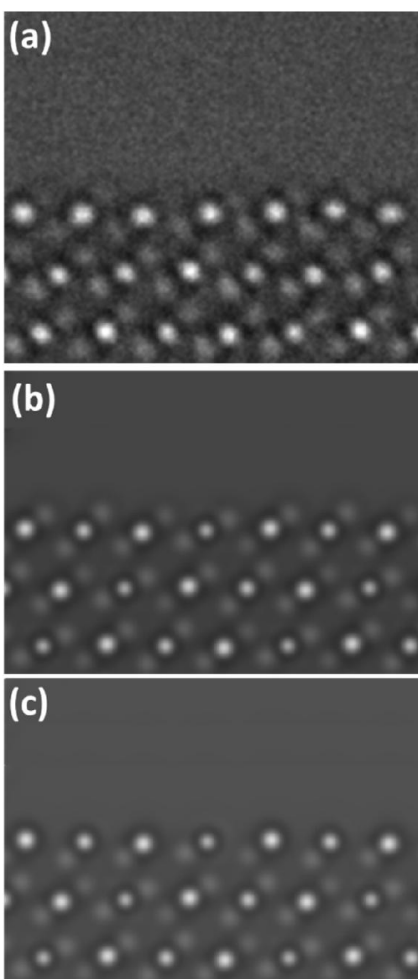


Figure 5.11 Experimental and Simulated HREM images of the (111) surface of a  $\text{Ce}_2\text{O}_3$  nanoparticle. (a) Experimental HREM image. (b), (c) Simulated HREM images using an O- and Ce-terminated (111) surface model respectively. Parameters for simulation: defocus 2 nm, thickness 3.2 nm.

## 5.4 Summary

In summary, the surface structure of the C-type  $\text{Ce}_2\text{O}_3$  nanoparticles is very similar to that of the  $\text{CeO}_2$  nanoparticles. The (100) surface is a polar surface, which results in a surface with a large amount of Ce and O vacancies. In terms of terminations, they can be O,  $\text{Ce}_4\text{O}_3$ , and Ce. The multiple surface structures are believed to lower the surface Gibbs free energy of the surface. The (110) surface has a coexistence of (111) nanofacets and flat  $\text{Ce}_2\text{O}_3$  terminations. In addition, there is a layer-by-layer removal of the surfaces by the intense electron beam. During the removal, O vacancies are created first. The Ce atoms next to the vacancies become unstable and diffuse away. The (111) surface is mostly O-terminated, which is in agreement with the electrostatic considerations. The C-type  $\text{Ce}_2\text{O}_3$  is usually considered as the completely reduced form of  $\text{CeO}_2$ . However, the surfaces of  $\text{Ce}_2\text{O}_3$  can be further reduced. The results in this study indicate the stabilities and redox properties of different facets of  $\text{CeO}_{2-x}$ -based nanostructures under strong reduction conditions.

## 6. Synthesis Dependent Atomic Surface Structures of SrTiO<sub>3</sub> Nanocuboids

### 6.1 Introduction

This chapter presents the atomic surface structures of as-prepared SrTiO<sub>3</sub> nanocuboids and the factors in the synthesis that can impact the surface structures. The catalytic properties of SrTiO<sub>3</sub> nanocuboids with different surface structures will also be discussed. The surface structures of SrTiO<sub>3</sub> single crystals have been extensively studied, especially for the (100) surface, as discussed in chapter 3. The atomic surface structures are found to be sensitive to the specimen treatments, such as annealing temperatures, oxygen vapor pressure, sputtering, and ion deposition [106, 159]. These factors significantly impact the thermodynamics and kinetics of surface structures. For instance, temperature not only is directly related to the Gibbs free energy of surface structures, but also can provide the activation energy to the overcoming of energy barriers toward forming a certain surface structure from an unstable one. In principle, the nanoparticles obtained by chemical syntheses have drastic different surface forming conditions compared to that of single crystals. The surfaces of the as-prepared nanoparticles are formed at the end of synthesis, which is usually in a solution phase and at a relatively lower temperature than the annealing temperature. In addition, the concentration of precursors and surfactants used in the synthesis may also impact the surface structures.

The choice of SrTiO<sub>3</sub> nanocuboids as a model system is based on three reasons: (1) As SrTiO<sub>3</sub> has a standard perovskite structure, which can be used as a prototype of studying surface structures of similar materials, understanding the surface structures of both single crystal and nanoparticles is of great interest in fundamental science. (2) The surfaces of nanoparticles can be

the active sites in catalysis. Therefore, understanding the factors that can impact the atomic surface structures of nanoparticles is crucial to understanding catalysis as well as to providing insights to improve catalytic properties of nanoparticles. (3) SrTiO<sub>3</sub> nanocuboids themselves are promising catalytic supports. The cuboid shape is thermally stable for SrTiO<sub>3</sub>, which enables catalysts to survive in rigorous catalytic conditions [160]. Moreover, the lattice parameter of SrTiO<sub>3</sub> is very close to that of the popular catalyst metals such as Pt, Pd and Au. The close lattice parameters enable a good epitaxy between the noble metal particles and SrTiO<sub>3</sub> nanocuboids. A good epitaxy, which is a similar concept of the coincidence site lattice (CSL) in the grain boundary research field, usually results in a stable interface. A strong metal-support interface should have a high catalytic stability [29].

## 6.2 Experiment

Three methods of synthesizing the SrTiO<sub>3</sub> nanocuboids were employed, as shown in Fig. 6.1. In a typical synthesis, NaOH and other agents are added to the solution containing Sr and Ti precursors to help control the morphology of the nanoparticles. The solution is then transferred to an autoclave with a Teflon liner. And the autoclave is then put into an oven for hydrothermal treatment for a certain amount of time. In particular, the first type of synthesis uses oleic acid as a capping agent as proposed by Hu et al. [161]. The end products are nanocuboids with a size of ~ 20 nm. The second hydrothermal route does not use oleic acid and results in nanocuboids with a size of ~ 65 nm [162]. During this synthesis, acetic acid was used to dissolve the Sr(OH)<sub>2</sub>, which was used as the Sr precursor. The third method is the same as the second one but uses a microwave oven instead of a conventional oven [41]. The apparent “benefit” of microwave synthesis is that it significantly reduces the hydrothermal treatment time from ~ 20 h to ~20 mins.



The microwave synthesis results in nanocuboids with a size of  $\sim 35$  nm. Typical TEM images are shown in Fig. 6.1 to demonstrate the general shapes of SrTiO<sub>3</sub> nanocuboids obtained by different preparation methods. The three methods will be referred to as oleic acid synthesis, acetic acid synthesis, and microwave synthesis, respectively. After being cleaned in water and ethanol thoroughly, the as-prepared nanocuboids were dry dried at 90°C for  $\sim 12$  hours.

The dry nanocuboids were dispersed in ethanol and deposited to a Cu TEM grid with lacey carbon coated. The grid was then transferred into a FEI-titan 80-300 TEM with Cc and Cs aberration correctors installed operating at 200 KeV. The Cc was tuned to be  $< 1$   $\mu\text{m}$  and the Cs corrected to  $\sim 0$   $\mu\text{m}$ . The other aberrations of the objective lens were tuned to an acceptable level on an amorphous area before image recording. After the sample was tilted to a (110) zone axis, a through-focal series of images were taken of the same area with 2 nm steps.

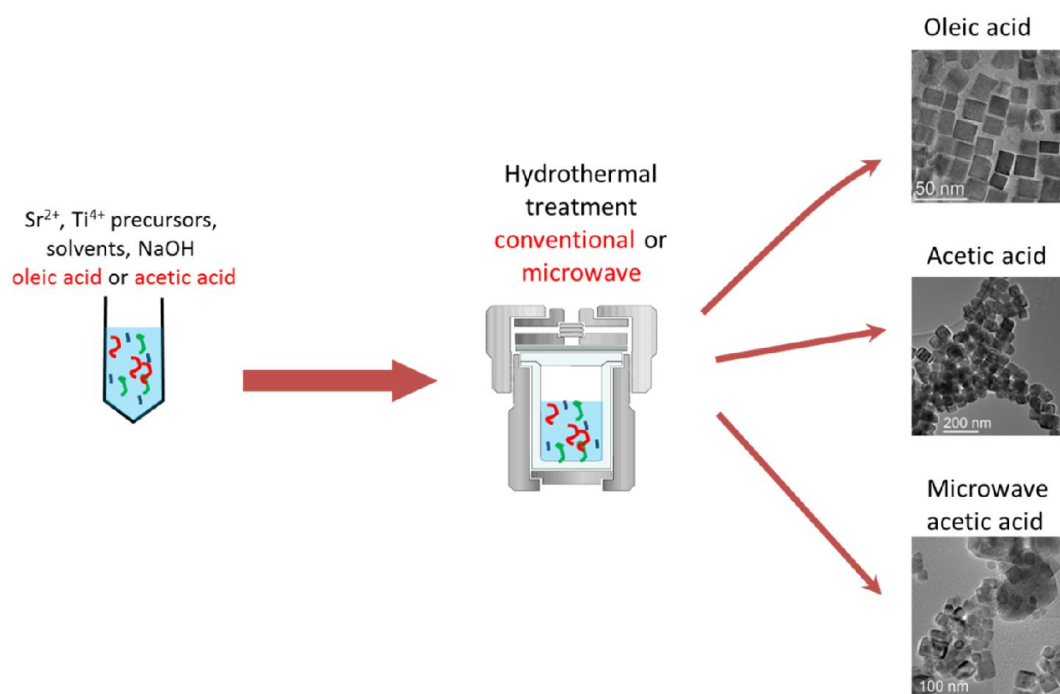


Figure 6.1 Schematic view of three different hydrothermal methods in synthesizing SrTiO<sub>3</sub> nanocuboids.

HREM simulation was performed using the MactempasX program based on multislice method [76] and conventional non-linear imaging theory [77]. Although the experiments were conducted using a Cc/Cs corrected TEM, residual aberrations unavoidably existed. The imaging parameters are measured before and after recording the HREM images. It was found the exact values of the parameters are continuously changing during the HREM experiment. The residual aberrations and specimen tilt were determined by maximizing the normalized cross-correlation coefficient (NCCC) between the experimental and simulated HREM images. The NCCC is defined as:

$$NCCC = \frac{\sum_i (I_1(i) - \bar{I}_1) \cdot (I_2(i) - \bar{I}_2)}{\sqrt{\sum_i (I_1(i) - \bar{I}_1)^2 \sum_i (I_2(i) - \bar{I}_2)^2}}$$

, where the sum is over the pixels in an image motif and the contrast of the experimental and simulated images is normalized to zero mean. If the NCCC = 1, the experiment matches “exactly” with the simulated image. If NCCC= 0, the contrast in experimental and simulated images has no relevance. If NCCC= -1, then there is a contrast reversal between the experimental and simulated images. It is known that there is an absolute contrast match problem between simulated and experimental HREM images [132]. To simplify the comparison, NCCC normalizes the image intensities by subtracting the mean and dividing by the standard deviation. Hence if NCCC = 1, it indicates the experimental and simulated images are linearly related.

The surface structures used in the multislice simulation are all relaxed by the DFT calculation. The DFT calculation is performed using the WIEN2K code [163], which is implemented based on all-electron augmented plane wave + local orbitals. The surface in-plane lattice parameters were set to those for the corresponding DFT optimized bulk cell, and an  $N \times N \times 10$  supercell for an  $N \times N$  surface reconstruction was used with  $\sim 1.6$  nm of vacuum to avoid errors within the DFT calculations as well as in the image simulations. Muffin-tin radii were set to 1.6, 2.45 and 1.8 Bohr for O, Sr and Ti respectively, as well as a  $\min(\text{RMT}) \cdot K_{\text{max}}$  of 7.5 and a  $16/N \times 16/N \times 1$  k-point grid.

## 6.3 Result and Discussion

### 6.3.1 Oleic Acid Synthesis

Fig. 6.2(a) shows a low magnification HREM image of a  $\text{SrTiO}_3$  nanocuboids synthesized by oleic acid method in  $[110]$  zone axis. The (100) surface structures are present on the edge, as indicated by the yellow arrow. The FFT of Fig. 6.2(a) is shown in Fig. 6.2(b). Fig. 6.2(c) shows an atomic resolution HREM image of the (100) facet. In this image, the sample thickness is

increasing from the left side to the right side. On the left side, all the bright spots are atoms. The contrast matches with the previous Cs-corrected HREM studies on SrTiO<sub>3</sub> single crystal with similar imaging conditions: as at small overfocus on a very thin specimen [164]. With the thickness increase, the intensity of Sr columns becomes black, which is consistent with the electron channeling contrast for HREM. The Sr atoms are heavier than the Ti and O columns, hence the intensity modulation of Sr columns are more obvious than that of Ti and O columns.

Fig. 6.2(d) shows the simulated HREM image of Fig. 6.2(c) using a SrO-terminated surface model. It is a spliced image of three separated images using changing thickness and defocus. Both the contrast on the bulk and surface regions match with the experiment well. It is worth noting that the thickness change will also result in a defocus change, as the defocus is defined as the focal distance between the exit wave plane and the focal plane of the objective lens.

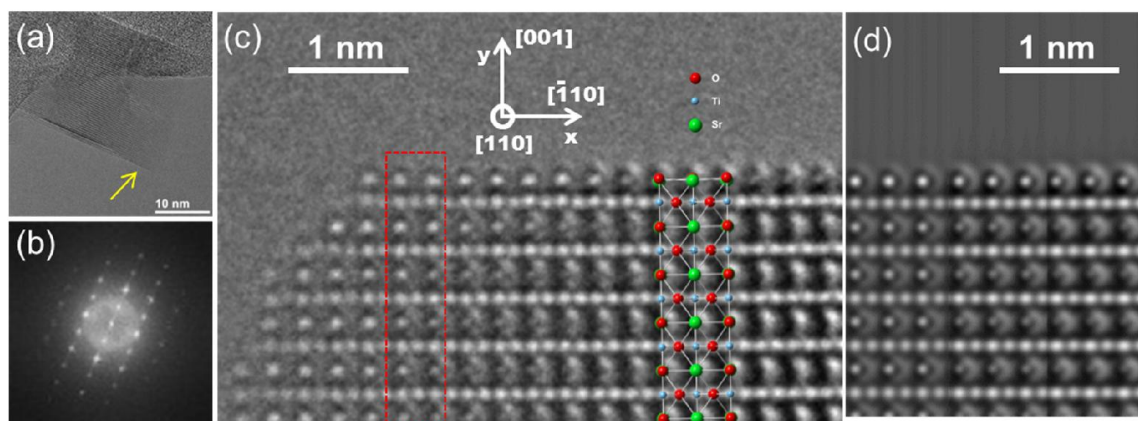


Figure 6.2 HREM results of SrTiO<sub>3</sub> nanocuboids synthesized by the oleic acid assisted process.

(a) Low magnification experimental HREM image of SrTiO<sub>3</sub> nanocuboid in [110] viewing direction. (b) The power spectrum of (a). (c) High magnification image of (a), where the bright spots can be interpreted as atoms. (d) Simulated HREM image of (c). In (c), due to the cuboid nature of the sample, the sample thickness and defocus are increasing from left to right.

Therefore, (d) is generated using 3 images simulated with continual changing defocus and thickness, which are increasing from left to right.

As profile-view imaging shows a 1-dimensional projection of a 2-dimensional surface structure, it is possible that some reconstructions can show  $1\times 1$  periodicity edge-on contrast under the  $[110]$  zone axis. To further confirm the simple  $1\times 1$  SrO termination, HREM simulations using other surface models have been performed and compared to the experimental image. Among all the tested surface models, the SrO termination best matches the experiment, as shown in Fig. 6.3. Eight surface structure candidates: SrO( $1\times 1$ ), TiO<sub>2</sub>( $1\times 1$ ), ( $2\times 1$ ) [47], ( $2\times 2$ ) [79], ( $3\times 3$ ) [82],  $c(4\times 2)$  [81],  $(\sqrt{13}\times\sqrt{13})R33.7^\circ$  [82],  $(\sqrt{2}\times\sqrt{2})R45^\circ$  [79] and  $(\sqrt{5}\times\sqrt{5})R26.6^\circ$  [82] on (100) surfaces are considered. Although the ( $2\times 1$ ),  $c(4\times 2)$ ,  $(\sqrt{13}\times\sqrt{13})R33.7^\circ$ ,  $(\sqrt{2}\times\sqrt{2})R45^\circ$ , and  $(\sqrt{5}\times\sqrt{5})R26.6^\circ$  surface reconstruction can all show the ( $1\times 1$ ) surface contrast along  $[110]$  direction, the bulk registry of the surface bright spots are quite different from the experimental image. The common feature of the surface reconstructions is that the surface Ti atoms are bonded to the subsurface O atoms while the surface O atoms are bonded to the subsurface Ti atoms. And the Ti columns show higher intensity than the O columns at the present HREM imaging condition. Thus in the reconstructions, the brighter spots are Ti atoms on top of subsurface O atoms, while in the SrO termination, the brighter spots are SrO columns on the top of Ti columns.

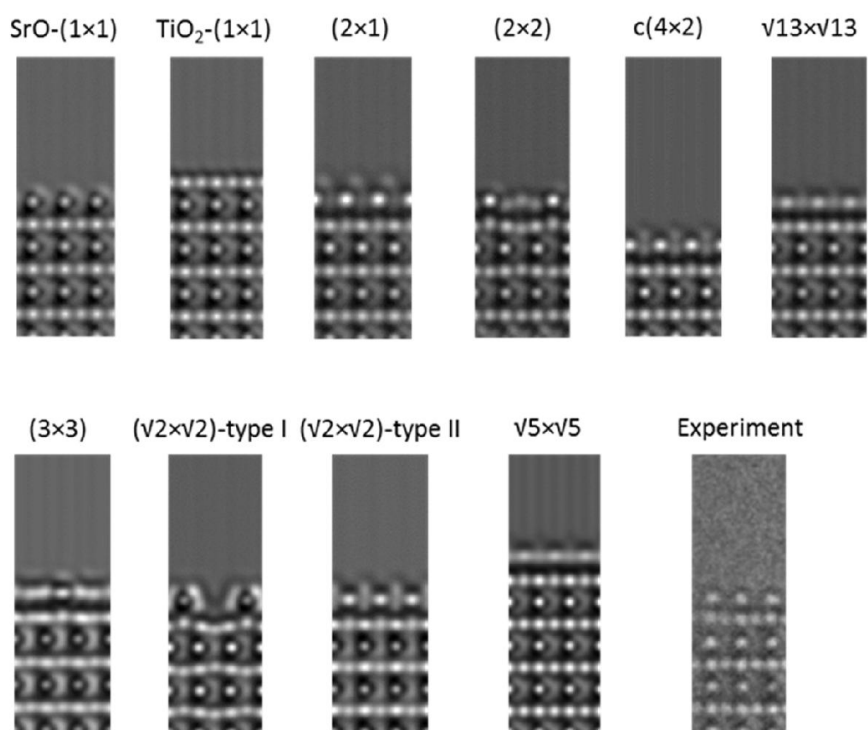


Figure 6.3 Simulated and experimental HREM images using different surface structural models under the same imaging conditions. Clearly the SrO-(1 $\times$ 1) matches with the experiment best (image dimension: 8.3 $\times$ 24.5  $\text{\AA}^2$  for all).

Lattice spacing measurement shows the SrO-terminated surface is relaxed. Fig. 6.4(a) shows the measured average lattice spacing from the surface to the bulk in the region marked with the red box in Fig. 6.2. To understand the lattice relaxation, the spacing measurement was also conducted on the simulated HREM images using unrelaxed and DFT relaxed surfaces structures using PBEsol0 [65] and PBE [64] functionals. According to the spacing measurement, the DFT relaxed structures match with the experiment surface spacing much better than the unrelaxed surface. Both the experiment and DFT relaxation show a strong inward contrast of the first SrO

surface layer. The second layer is slightly expanded. No significant surface relaxation is present after the third surface layer. The DFT calculations with PBE and PBEsol0 functionals both result in good matches with the experiment. A careful check of the absolute positions relative to the bulk shows that the result from the PBE functional has a slightly larger systematic error, as shown in 3.4(b). This is due to the 8<sup>th</sup> layer contracts too much towards the bulk in the DFT calculation using the PBE functional. It is generally agreed that the PBE functional is too covalent and overbonds the surface atoms while the hybrid functional (PBEsol0) overcomes this shortcoming somewhat by correcting the exchange term for the strongly correlated d-electrons of Ti.

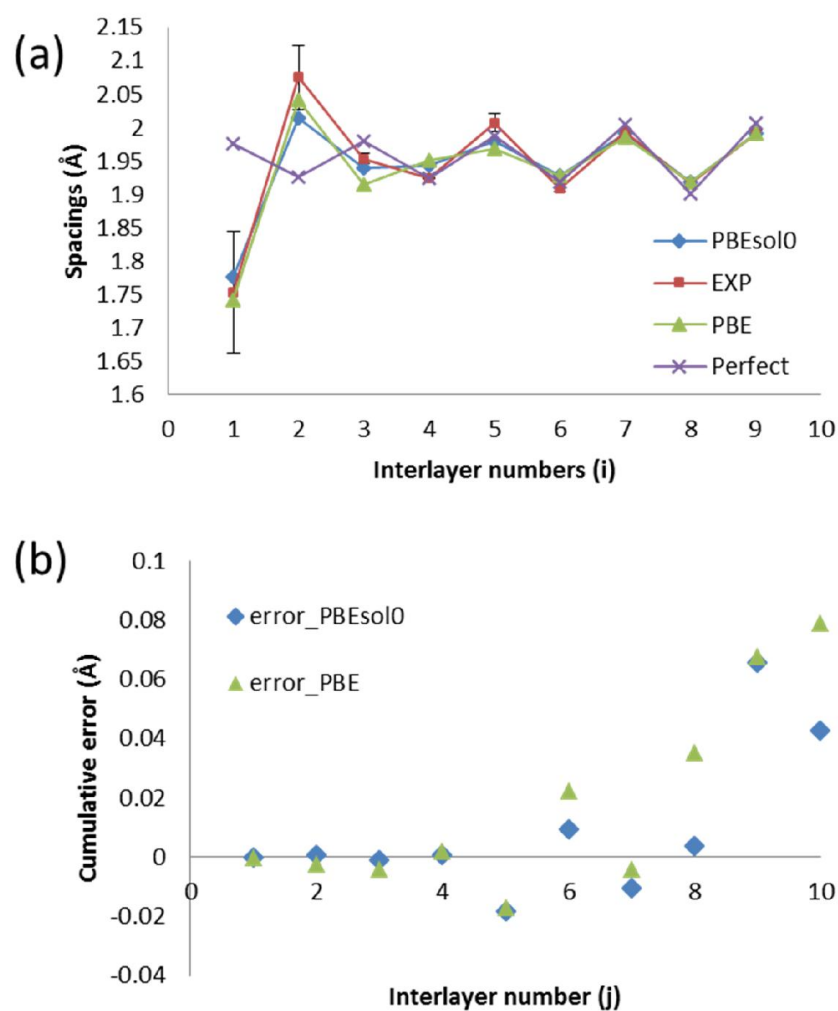


Figure 6.4 Comparison of the surface relaxation by using different DFT functionals. (a) Interlayer spacing comparison of the experimental image and simulated images for unrelaxed and DFT relaxed structures. The comparison is based on the area marked in the red box in Fig. 6.2(c). The interlayer spacings (i) are measured from Gaussian fits to the peak positions of the SrO-Ti atomic columns from the surface into the bulk. The error bars indicate the experimental deviation with respect to the mean values. (b) Cumulative error comparison between the DFT calculation using the PBE and the PBEsol0 functional. The base line was chosen as the 10th layer in the bulk from the surface ( $j=1$  is the 10<sup>th</sup> interlayer spacing from the surface).

The oscillations of  $\sim 50$  pm in the lattice spacing after the interlayer number 4 are due to the TEM artifacts, as the perfect structure without any lattice relaxation shows a continuous



oscillation around the spacing of 1.95 Å. Specifically, the non-symmetric aberrations, such as 3-fold astigmatism and coma, as well as the specimen tilt can affect the magnitude of the oscillation. Fig. 6.5 shows the change of the lattice spacing oscillation with respect to the change of coma and thickness. Note that the tilt can show a larger impact on HREM images with a thicker specimen. The cause of the distortion-dependent oscillation is rather simple: the peak intensity of the Ti column is higher than the SrO column. A homogeneous distortion to the HREM image will distort the weak intensity spots (SrO) more than the high intensity spots (Ti). As a result, the distances between the alternating Ti and SrO peak positions become oscillating.

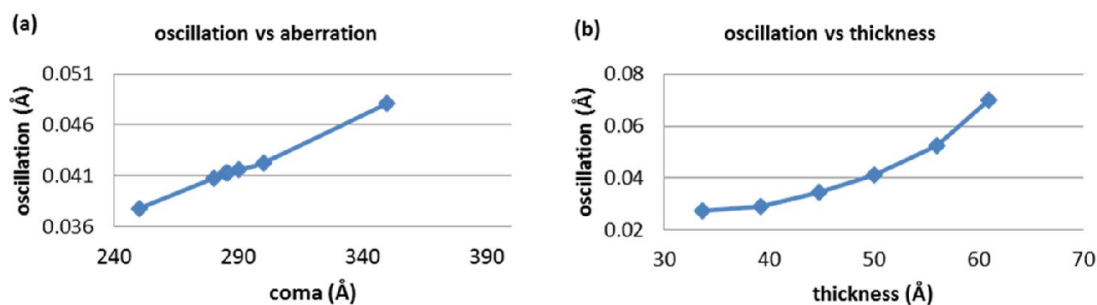


Figure 6.5 Interlayer spacing oscillation is dependent on the thickness and coma. (a) At defocus=2nm, thickness=5nm, the best coma is at around 286Å. (b) By setting the aberrations fixed (coma at 286Å), changing the thickness, the best thickness is found at 50Å.

### 6.3.2 Acetic Acid Synthesis

Fig. 6.6(a) shows a typical SrTiO<sub>3</sub> nanocuboid from the acetic acid synthesis viewing in a [110] zone axis. The yellow arrow indicates a (100) surface. Fig. 6.6(b) shows an experimental profile-view HREM image at atomic resolution. Although the imaging condition is very similar to the oleic acid synthesis case, the surface contrast is very different. The surface layer is not a SrO layer. The simulated HREM image using a ( $\sqrt{13} \times \sqrt{13}$ )R33.7° surface structure is shown in Fig.

6.6(c), which matches with the experimental image reasonably well. The atomic model is overlaid on Fig. 6.6(b).

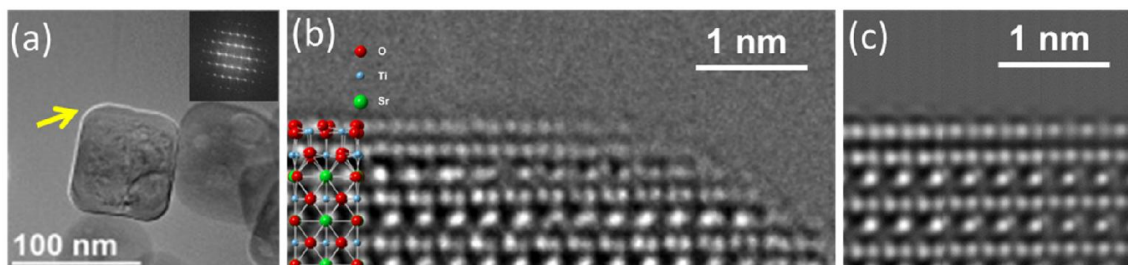


Figure 6.6 HREM images from the acetic acid synthesis. (b) Experimental HREM image of a  $\text{SrTiO}_3$  nanocuboid along  $[110]$ . (a) Low magnification image of (b). The inset shows the power spectrum. (c) A simulated image using a RT13 reconstructed surface. The RT13 atomic surface structures along the  $[110]$  viewing direction is overlaid in (b). In (b), owing to the nature of the sample, the sample thickness and defocus are increasing from right to left. Therefore, (c) was generated using 3 images simulated with different defocus and thickness, increasing from right to left.

To further confirm the surface structures, multiple surface structure candidates are simulated using the same imaging condition, as shown in Fig. 6.7. The  $(1 \times 1)$   $\text{TiO}_2$  and  $\text{SrO}$  terminations can be excluded. Moreover, the locally-ordered  $(3 \times 3)$ ,  $(\sqrt{13} \times \sqrt{13})R33.7^\circ$ , and  $(\sqrt{5} \times \sqrt{5})R26.6^\circ$  best match with the experimental contrast. The well-ordered  $(2 \times 1)$ ,  $c(4 \times 2)$  and other structures are obviously different from the experiment. The difference among the  $(3 \times 3)$ ,  $(\sqrt{13} \times \sqrt{13})R33.7^\circ$ , and  $(\sqrt{5} \times \sqrt{5})R26.6^\circ$  is rather small. In addition, previous DFT calculation shows the energy difference among the three surfaces is very small [82]. Therefore, it is possible that the three surfaces can co-exist on the  $(100)$  surface of  $\text{SrTiO}_3$  nanocuboids.

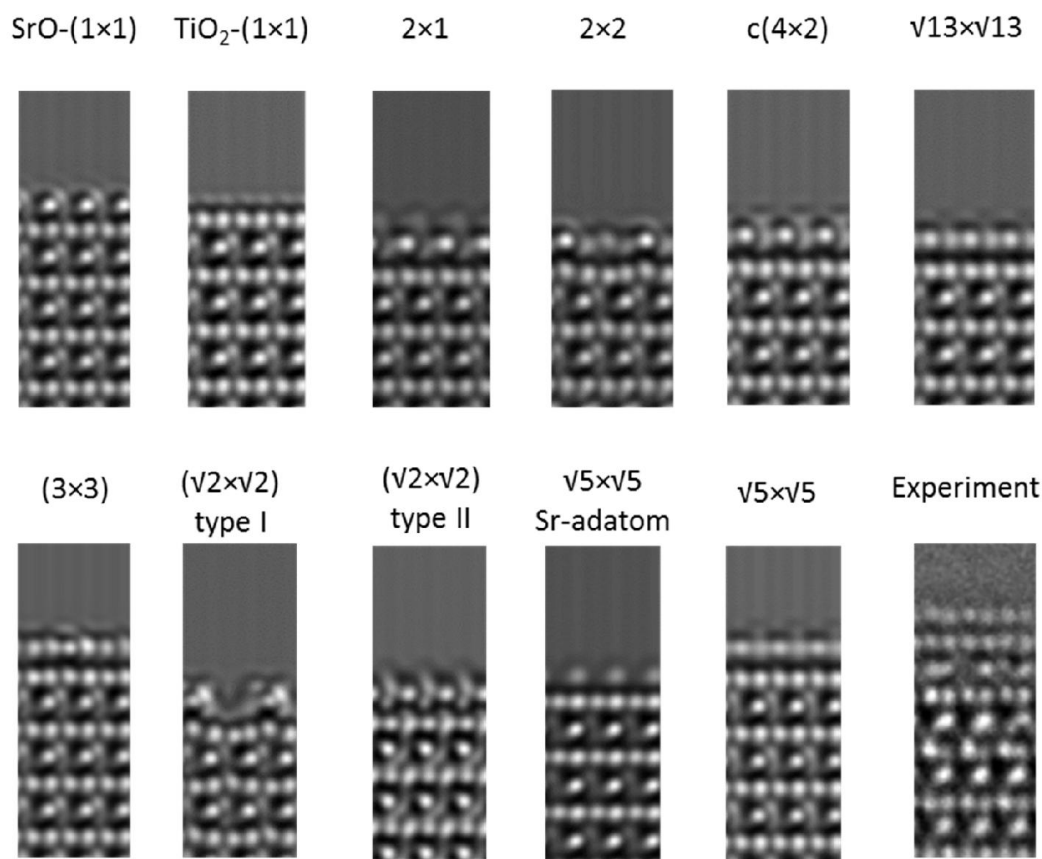


Figure 6.7 Simulated images using different surface reconstructions with the same imaging conditions. Clearly the locally ordered  $(\sqrt{13}\times\sqrt{13})R33.7^\circ$ ,  $(\sqrt{5}\times\sqrt{5})R26.6^\circ$  and  $(3\times3)$  reconstructions match with the experiment better than the well-ordered ones (image dimension:  $8.3\times 23.0 \text{ \AA}^2$  for all).

### 6.3.3 Microwave Synthesis

Fig. 6.8(a) shows a HREM profile-view image on a  $\text{SrTiO}_3$  nanocuboid from the microwave synthesis in  $[110]$  zone axis. Fig. 6.8(b) shows an atomic resolution HREM image on the surface region of the nanocuboid, as indicated by the yellow arrow in Fig. 6.8(a). The atomic surface structure of  $\text{SrTiO}_3$  nanocuboids from the microwave synthesis is different from the other two syntheses. The surface has an obvious mixture of SrO and double- $\text{TiO}_2$ -layer terminations. Fig.

6.8(c) shows a simulated HREM image of 3.8(b) using mixed (3×3) and SrO-terminated surface models, which matches with the experimental contrast reasonably well.

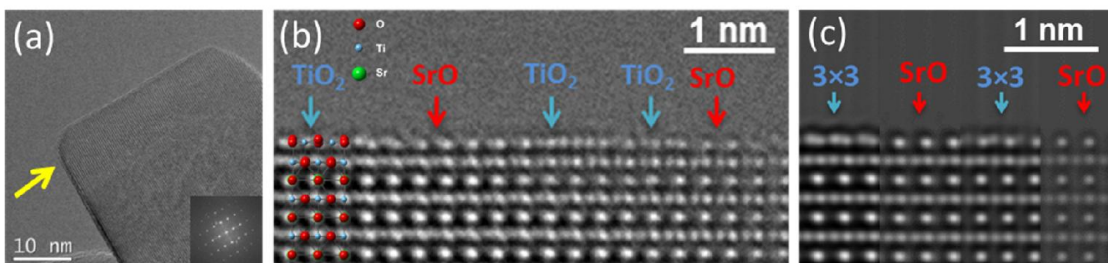


Figure 6.8 HREM images of SrTiO<sub>3</sub> nanocuboids obtained by the MA-HT synthesis. (b) Experimental HREM image of a SrTiO<sub>3</sub> nanocuboid along [110]. (a) Low magnification image of (b). The inset show the power spectrum of (a). (c) A simulated image using a SrO terminated surface (areas with red arrows) and a layered structure model consisting of 50% of SrO and 50% of (3×3) surface terminations (areas with blue arrows). The (3×3) and SrO atomic surface structures along [110] is overlaid in (b). In (b), owing to the nature of the sample, the sample thickness and defocus are increasing from right to left. Therefore, (c) was generated using 4 images simulated with different defocus and thickness, increasing from right to left.

Extensive HREM simulations indicate the TiO<sub>2</sub>-rich surface contrast cannot be explained by SrO-termination and the well-ordered surface reconstructions, as shown in Fig. 6.9. Again, locally-ordered (3×3), ( $\sqrt{13}\times\sqrt{13}$ )R33.7°, and ( $\sqrt{5}\times\sqrt{5}$ )R26.6° match with the experimental results much better. Exactly which surface reconstructions are present is difficult to determine. It is possible that in the viewing direction, there can be a mixture of TiO<sub>2</sub>-rich and SrO terminations too. By constructing a layered structural model with 50% SrO and 50% (3×3) reconstruction in the viewing direction, the simulated image matches with the experiment better

than using a single surface reconstruction, as shown in Fig. 6.10. Quantitatively, the NCCC between the experimental image and the simulated image with a pure  $(3\times 3)$  reconstruction is 0.85. The NCCC between the experimental image and simulated image with 50% SrO and 50%  $(3\times 3)$  surface is 0.91. Fig.3.8(c) is an image spliced together by the simulated images using a SrO surface model and layered surface models of  $(3\times 3)$  and SrO terminations.

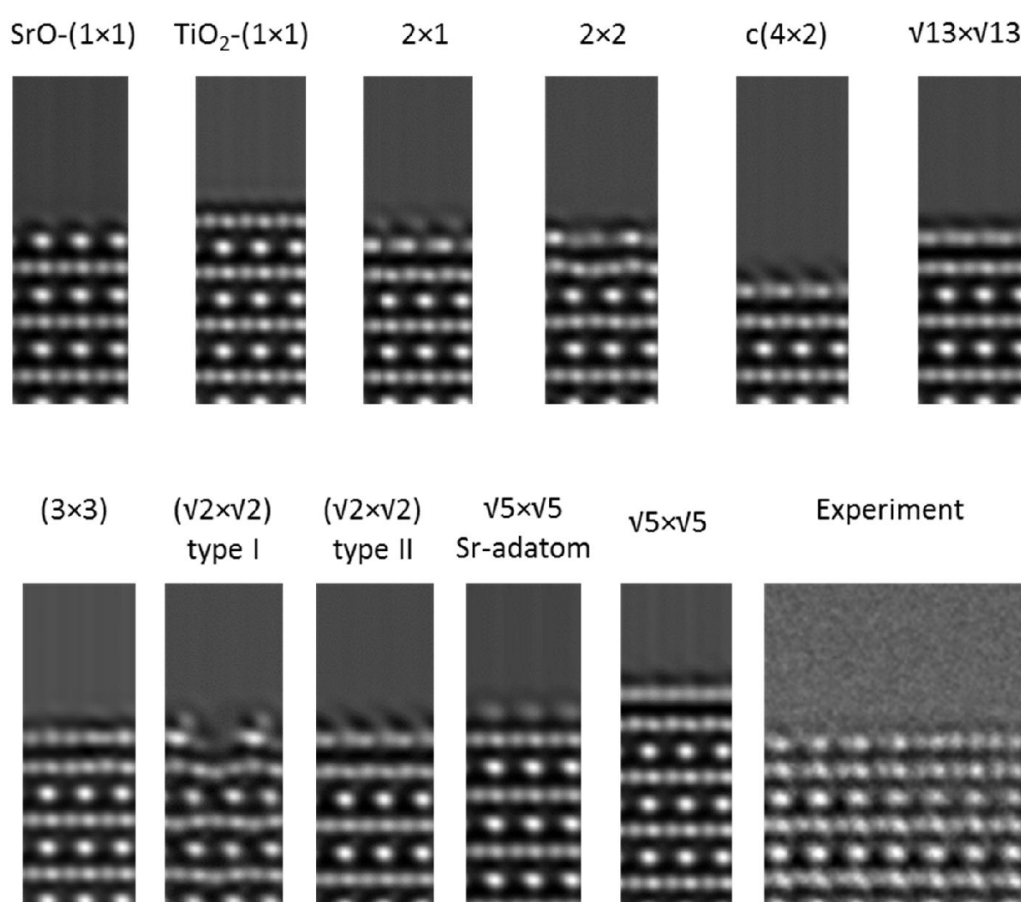


Figure 6.9 Simulated images using different surface reconstructions with the same imaging conditions. (image dimension:  $8.3\times 23.3 \text{ \AA}^2$  for the simulated images,  $19.7\times 23.3 \text{ \AA}^2$  for the experimental image).

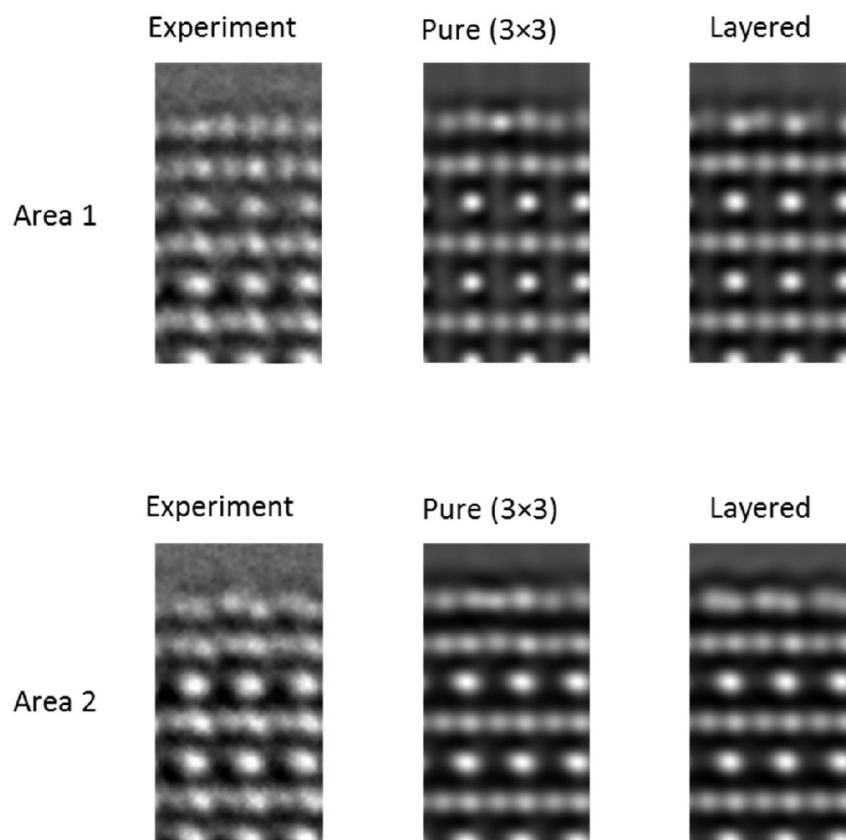


Figure 6.10 Comparison of the experimental images, simulated images with the pure (3×3) reconstructed surface structure, and the layered structure with 50% of SrO and 50% of (3×3) surface (image dimension:  $8.3 \times 14.9 \text{ \AA}^2$  for all).

### 6.3.4 Surface Formation Mechanisms

The different surface structures should be related to the synthetic procedures. The key differences are whether or not to use the oleic acid and whether or not to use the microwave oven. Oleic acid is often used in synthetic chemistry to control the size and morphology of nanoparticles. The in-situ SAXS study during the nanocuboid synthesis performed by our group shows oleic acid (or oleate) molecules can form a liquid crystal-like microemulsion [161]. The microemulsion has a lamellar texture which controls the cuboid shape and the size of the  $\text{SrTiO}_3$

nanocuboids. Moreover, the oleate molecules are found to bond to the surfaces of nanocuboids rather tightly, which is confirmed in the IR spectroscopy, as shown in Fig. 6.11. The vibration absorbance peaks at  $1555\text{cm}^{-1}$  and  $1466\text{ cm}^{-1}$  were assigned to asymmetric and symmetric stretching vibration of  $\text{COO}^-$  of oleic acid. The peaks in the region around  $3000\text{ cm}^{-1}$  should be assigned to the CH stretching bands of the oleic acid, with comparable intensity to the peaks at  $1555\text{cm}^{-1}$  and  $1466\text{ cm}^{-1}$ . On the other hand, the bonding between  $\text{Sr}^{2+}$  and oleate ions is more favorable than the bonding between  $\text{Ti}^{4+}$  and oleate ions, which is probably due to the acidity. The Sr is an alkaline earth metal while the Ti is a transition metal. The Sr should be more basic than the Ti metals. Indeed, studies have demonstrated the  $\text{TiO}_2$ -terminated  $\text{SrTiO}_3$  surface has a higher acidity than the SrO-terminated surface [165, 166]. It is reasonable for the preferential bonding between the  $\text{Sr}^{2+}$  and oleate ions, as shown in Fig. 6.13. As the as-prepared  $\text{SrTiO}_3$  nanocuboids are covered by a layer (or more) of oleic acid, there is a strong driving force for a SrO termination.

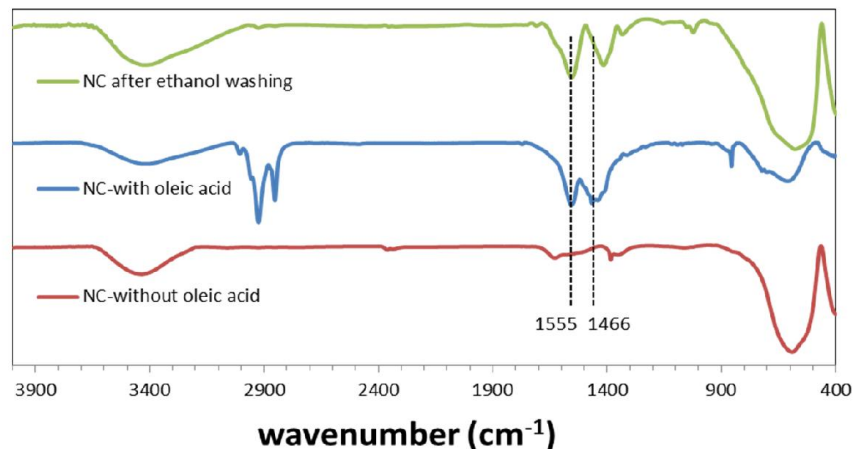


Figure 6.11 Comparative FT-IR study on the fresh SrTiO<sub>3</sub> nanocuboids (NC-with oleic acid), the ones after ethanol washing (NC after ethanol washing) and the ones after 600°C air annealing (NC-without oleic acid). The vibration absorbance peaks at 1555cm<sup>-1</sup> and 1466 cm<sup>-1</sup> were assigned to asymmetric and symmetric stretching vibration of COO<sup>-</sup> of oleic acid. The peaks in the region around 3000 cm<sup>-1</sup> should be assigned to the CH stretching bands of the oleic acid, with comparable intensity to the peaks at 1555cm<sup>-1</sup> and 1466 cm<sup>-1</sup>.

The oleate ions cannot be seen in the HREM images, which is partially because the nanocuboids for imaging are thoroughly washed in ethanol. The oleate ions were intentionally removed for HREM imaging (sharp surface contrast). The IR spectroscopy on the nanocuboids after thorough ethanol washing is also shown in Fig. 6.11. The same IR experiment was conducted on the SrTiO<sub>3</sub> nanocuboids after annealing at 600°C. The high temperature annealing should burn off all the organic ligands. The IR spectroscopy is used as a reference signal for the clean SrTiO<sub>3</sub> nanocuboids, as shown in Fig. 6.11. For both the ethanol washed and annealed nanocuboids, there is almost no signal in the CH stretching region around 3000 cm<sup>-1</sup>. There are other evidence for the oleic acid coverage on the surface of as-prepared SrTiO<sub>3</sub> nanocuboids. Fig. 6.12 (a) and (b) show the well-assembled arrays of nanocuboids with the separation close to the length of an



oleic acid molecule. After ethanol wash, the oleate ions dissolve and the nanocuboids are randomly positioned, as shown in Fig. 6.12(c) and (d). In addition, thermogravimetric analysis (TGA) was conducted on the as-prepared nanocuboids in O<sub>2</sub>, as shown in Fig. 6.12(e). The weight starts to decrease as the temperature increases and become stable at 300°C. Based on the weight loss, the amount of oleate ions are enough to have a full coverage on the nanoparticles, assuming the oleate ions are only bonded to the surface Sr ions. Therefore, a homogenous SrO-termination is possible.

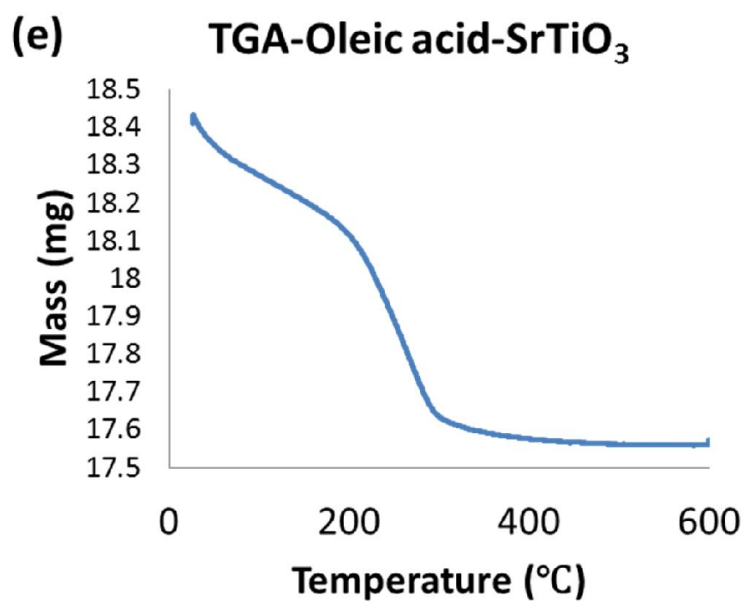
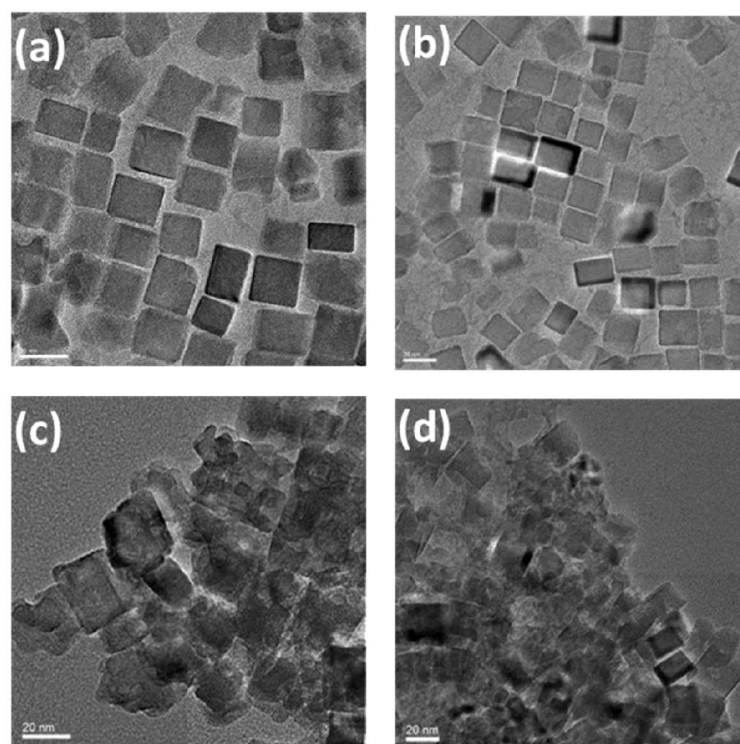
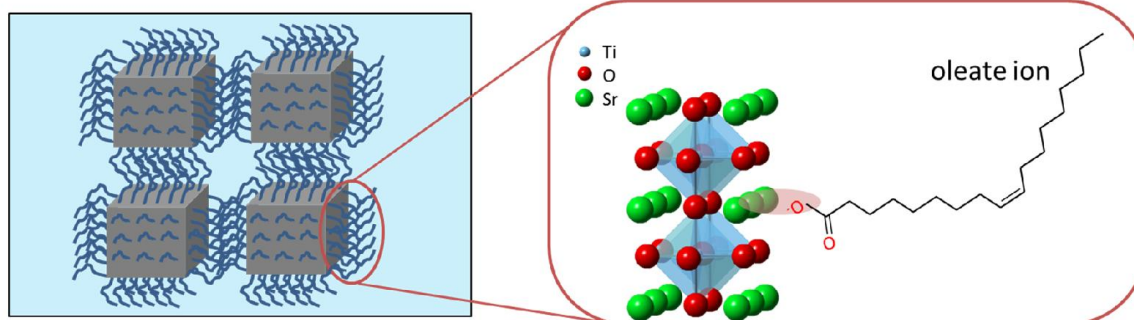


Figure 6.12 Evidence of oleate covered on the surface. (a),(b) TEM images of as-prepared SrTiO<sub>3</sub> nanocuboids with oleate covered. (c),(d) TEM images of SrTiO<sub>3</sub> nanocuboids washed in ethanol. (e) TGA result shows the decrease of the mass of SrTiO<sub>3</sub> nanocuboids with the increases of temperature.

The environment of nanoparticle growth in the acetic acid syntheses is very different, as shown in Fig. 6.13. The acetic acid is soluble in both water and ethanol. No liquid crystal-like emulsion is formed during the syntheses. The nanocuboids are exposed to a homogeneous solution containing  $\text{Sr}^{2+}$  and  $\text{Ti}^{4+}$  ions. The shape of the nanocuboids is mostly controlled by thermodynamic Wulff construction as there is no confinement due to the acetate. At the final stage of the nanocuboid growth, the amount of metal precursors is depleted. Thermodynamically, low energy surface configuration is favored under such environment. The locally-ordered reconstructions are located on the convex hull, according to the previous DFT study [82]. The reconstructions formed in solution are similar to the surface reconstructions on single crystals formed in air when the surfaces are fully oxidized [82]. A big difference is the wet condition in the solution. However, a previous DFT study have demonstrated that for a wet surface of  $\text{SrTiO}_3$  (001), the stable surface structure is the pure reconstructed  $\text{SrTiO}_3$  surface with water molecules rather weakly chemisorbed [103, 167]. Therefore, it is possible that the as-prepared  $\text{SrTiO}_3$  nanocuboids from the acetic acid synthesis are covered with water molecules. However, these water molecules desorb during the drying process and the electron-irradiation in HREM imaging.

### Oleic Acid Synthesis



### Acetic Acid Synthesis

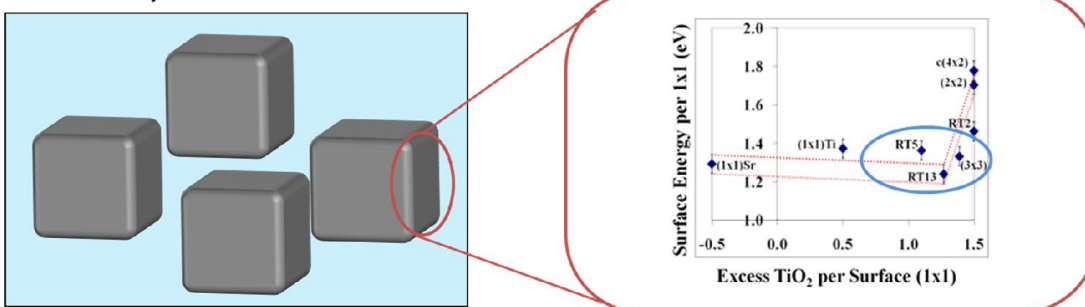


Figure 6.13 Mechanisms of the formation of different surface structures.

The role of microwave in the chemical synthesis is not completely clear [168]. The microwave treatment can induce effects other than generating heat. In addition to reaction temperature, it has been demonstrated that the microwave irradiation frequency and bandwidth sweep time can influence the phase and size of BaTiO<sub>3</sub> nanoparticles [169]. It is possible that the electric field couple with the dielectric constant of the precursors and the end products, which may affect the atomic surface structures of the nanocuboids. Exactly why the microwave irradiation can enhance the SrO termination and make the surface more stoichiometric (similar amount of surface SrO and TiO<sub>2</sub>) require further study.

## 6.4 Summary

The atomic surface structures of SrTiO<sub>3</sub> nanocuboids are synthesis-dependent. The oleic acid synthesis results in the nanocuboids with SrO-terminated surface. In contrast, the nanocuboids obtained by acetic acid synthesis are terminated by locally-ordered TiO<sub>2</sub>-rich surface reconstructions. The microwave synthesis results in a mixed surface with both SrO termination and TiO<sub>2</sub>-rich reconstructions. The SrO termination of the nanocuboids from the oleic acid synthesis is probably due to the preferential bonding between oleate and Sr ions. Without oleic acid, the locally-ordered TiO<sub>2</sub>-rich surface reconstructions are formed, which is probably because of the intrinsic low energies associated with the structures in the solution. The mechanism of forming mixed surface terminations in the microwave synthesis is not clear, which requires further studies. The discoveries in this study may be qualitatively extendable to other perovskite or mixed metal oxide materials.

## 7. Electron-induced Ti-rich Surface Segregation on SrTiO<sub>3</sub> Nanocuboids

### 7.1 Introduction

This chapter presents the surface features of SrTiO<sub>3</sub> other than reconstructions. In addition to the flat surface reconstructions, step-terrace structures [8, 170], ridges [171], canyon-like features [172], and islands [173] on SrTiO<sub>3</sub> (001) surfaces have been revealed by microscopic techniques. These surface features can be Sr-rich or Ti-rich, depending on the annealing condition. It is generally accepted that the Ti-rich surface features can be formed after prolonged annealing at reduction conditions [174-176]. In contrast, the Sr-rich surface features are formed after prolonged annealing at oxidation conditions [174-176]. The surface chemistry can be different or more complicated on metal doped SrTiO<sub>3</sub> and other perovskite materials [177, 178]. In this study, the Ti-rich surface islands are formed with intense electron irradiation on SrTiO<sub>3</sub> nanocuboids.

Understanding the surface chemistry of SrTiO<sub>3</sub> is of great interest in both fundamental science and technological applications. The surface chemistry is strongly-related to the surface structures. Usually, surface reconstructions are formed on SrTiO<sub>3</sub> after ion-milling (or acid etching) and annealing at a high temperature [47, 81-83, 95, 179]. The solved surface reconstructions are found to be TiO<sub>2</sub>-rich [47, 81, 82]. The excess surface Ti should be one of the driving forces of forming TiO<sub>2</sub>-rich surface reconstructions. For the ion-milled or sputtered surfaces, it is usually believed the source of excess surface Ti is from the bulk crystal. On the other hand, the surface of acid-etched specimen is believed to be TiO<sub>2</sub>-rich, as the acid can preferentially dissolve the SrO layer [25]. Therefore, it is possible to control the surface structures by inducing a certain amount of excess Ti or Sr on the surface. In this study, direct evidence of excess surface Ti

species will be provided and the possible mechanism of the surface Ti enrichment will be proposed under electron beam irradiation. This is not only a beam damage study as understanding the mechanisms of the surface chemistry of SrTiO<sub>3</sub> is the goal.

## 7.2 Experiment

The ethanol washed SrTiO<sub>3</sub> nanocuboids from oleic acid synthesis [161] were dispersed in ethanol. The suspension was deposited to a Cu TEM grid coated with a lacey carbon film. The grid was then transferred into a FEI-titan 80-300 TEM with Cc and Cs aberration correctors installed and operating at 200 KeV. The base pressure of the specimen column was  $\sim 1 \times 10^{-7}$  Torr. All the aberrations up to C5 were tuned to an acceptable level (Cc $\sim$ 1 $\mu$ m, Cs $\sim$ 0 $\mu$ m, astigmatisms and coma  $\sim$ 0  $\mu$ m, C5 $\sim$ -1 mm) before recording the HREM images. After the nanocuboids were tilted to [100] or [110] zone axes, time-series images were taken with the interval of 1s. The electron dose was measured as  $\sim 4 \times 10^6$  e/nm<sup>2</sup>s for the HREM imaging. When the electron beam was converged to a  $\sim$ 2nm probe, the dose can be two orders larger. The high flux electron probe was applied to SrTiO<sub>3</sub> nanocuboids to study the beam damage. The EELS measurement was conducted in TEM diffraction mode. The beam was converged to a  $\sim$ 2 nm area to enhance the spatial resolution. HREM simulation was performed using the MactempasX program based on multislice simulation and conventional non-linear imaging theory. The simulation parameters for simulated images are listed in the figure captions.

## 7.3 Results and Discussion

As discussed in Chapter 6, the surface of SrTiO<sub>3</sub> nanocuboids formed in the oleic acid synthesis is SrO terminated [41]. Fig. 7.1 shows another HREM image of SrTiO<sub>3</sub> nanocuboids with a SrO surface termination in the [110] zone axis. The atoms show black contrast at the left part in Fig.

7.1(a). The black contrast can be obtained at the slight underfocus condition (several nms) on a thin specimen (several nms). As the thickness increases, the intensity of the atom columns starts to modulate. Therefore, the atoms show white contrast in the middle part of the Fig. 7.1(a). Nevertheless, the surface of the nanocuboids is atomically flat, which is in agreement with the results of Chapter 5. With an intense electron beam (by converging the beam to a  $\sim 2$ nm spot) applied to the bulk region of the nanocuboid for several seconds, additional surface materials show up, as indicated by the arrow in Fig. 7.1(b).

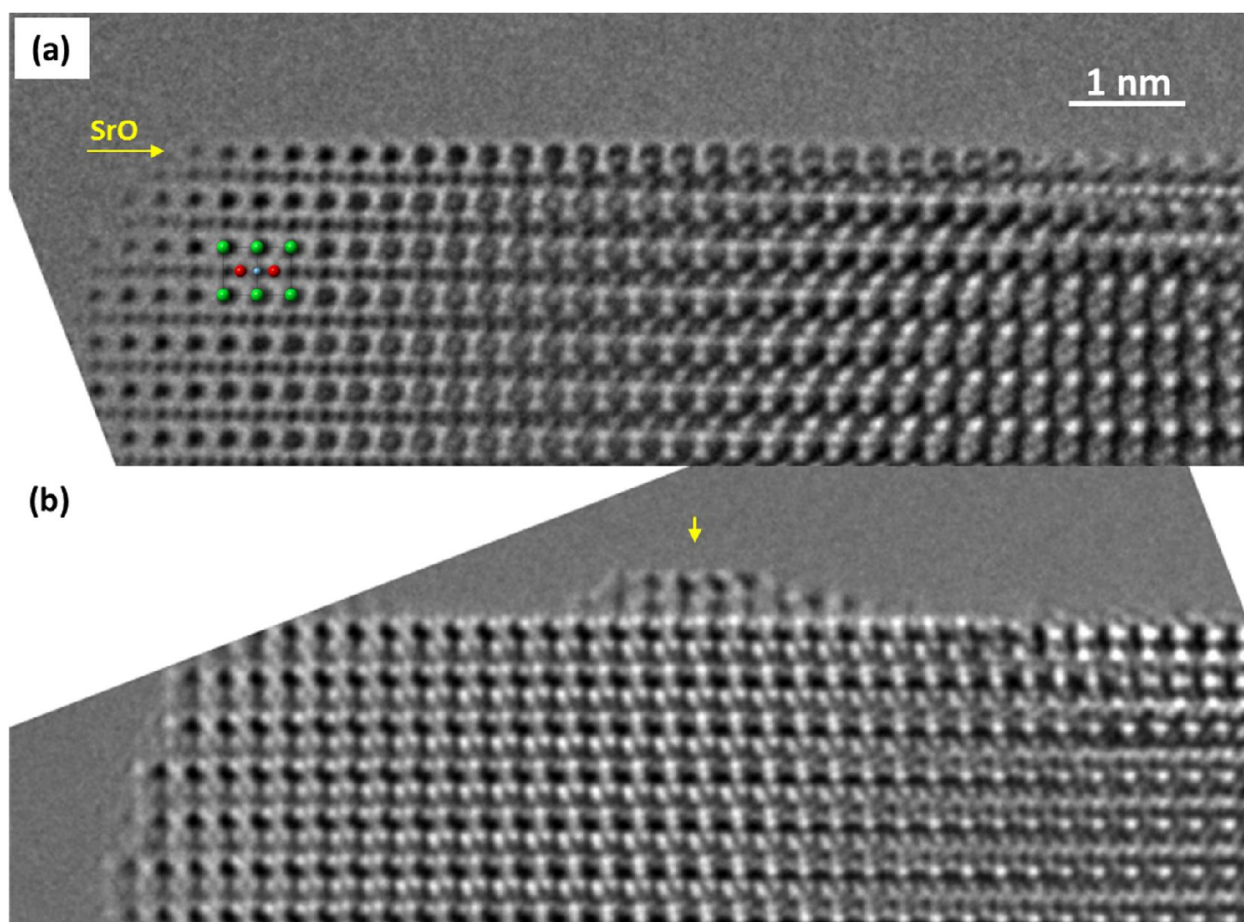


Figure 7.1 Formation of surface islands on SrTiO<sub>3</sub> nanocuboids under electron beam irradiation. (a) A HREM image in [110] zone axis showing a flat (001) surface was observed initially, and was assigned to be the intrinsic surface. (b) With a  $\sim 2$  nm converged electron probe applied on



the nanocuboids for  $\sim 5$ s, an additional island can be observed clearly, as indicated by the yellow arrow.

This beam damage phenomenon is very reproducible. The evolution of surface islands has been recorded, as shown in Fig. 7.2. The three images Fig. 7.2(a), (b), and (c) are obtained by applying an intense converged electron probe on the nanocuboid for approximately 3s, 6s, and 9s, respectively. In Fig. 7.2(a), additional surface layers start to form. At the later stage, surface islands are formed, as shown in Fig. 7.2(c). It seems that the left part of the surface is flatter in Fig. 7.2(c) than the surface in Fig. 7.2(b). It is possible that the atoms migrated to the right part to form islands. The lattice spacing measurement shows the islands have a square lattice pattern with the spacing of  $2.1 \text{ \AA}$ , which is  $\sim 8\%$  larger than the spacing of the (200) planes of  $\text{SrTiO}_3$ . By searching all the reported strontium oxides, titanium oxides, and Ruddlesden-Popper phases, only the  $\text{TiO}$  with a rocksalt structure can match the experimental lattice pattern and lattice parameters.  $\text{SrO}$  also has a rocksalt structure, however, the lattice parameter is  $\sim 5.1 \text{ \AA}$ , which is significantly different from the experiment.

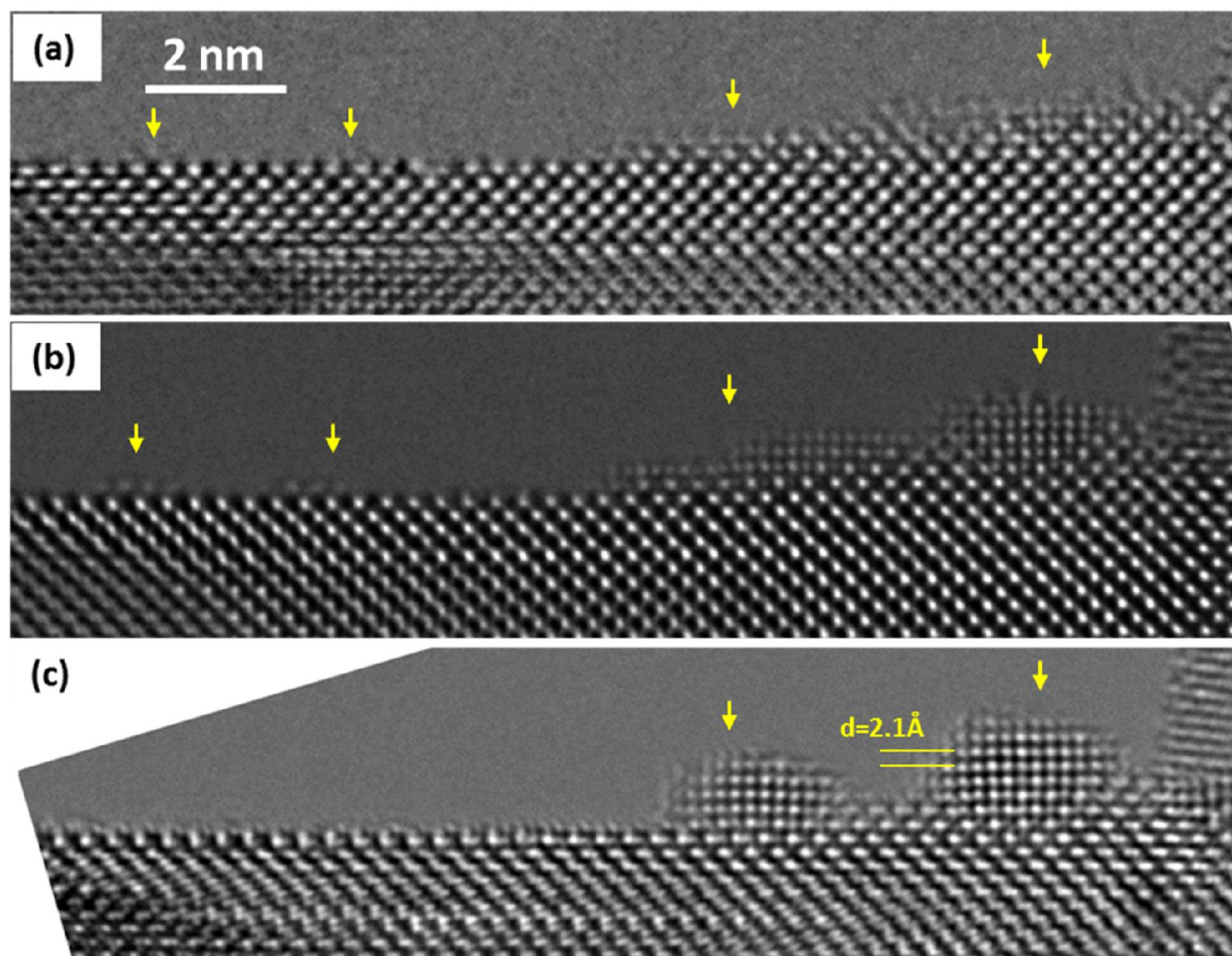


Figure 7.2 Evolution of the SrTiO<sub>3</sub> (001) surface under electron beam irradiation. (a), (b) and (c) HREM images obtained by focusing the beam on the nanocuboids for ~ 3 s, 6 s, and 9 s, respectively. In (a), beam induced additional layers start to form. In (c), TiO islands formed. The lattice spacing is 2.1 Å, as indicated by the yellow lines.

Fig. 7.3(a) shows another beam damaged SrTiO<sub>3</sub> nanocuboid. An atomic resolution image of the region highlighted by the yellow ellipse in Fig. 7.3(a) is shown in Fig. 7.3(b). Fig. 7.3(c) is a cropped image of Fig. 7.3(b) and Fig. 7.3(d) is the simulated image of Fig. 7.3(c). As the image was taken at the underfocus condition, the atoms show black contrast. In the HREM simulation, a structural model with rocksalt TiO thin film on a SrO-terminated SrTiO<sub>3</sub> substrate is used. For

simplicity, the thickness of the TiO and SrTiO<sub>3</sub> regions are set to the same. In addition, the lattice spacing of TiO region was set to match that of the SrTiO<sub>3</sub> substrate. Therefore, no lattice strain can be observed in the simulation as well as an absolute contrast mismatch between the simulated and experimental images. Nevertheless, the good match between the experimental and simulated HREM images confirms the surface island is rocksalt TiO.

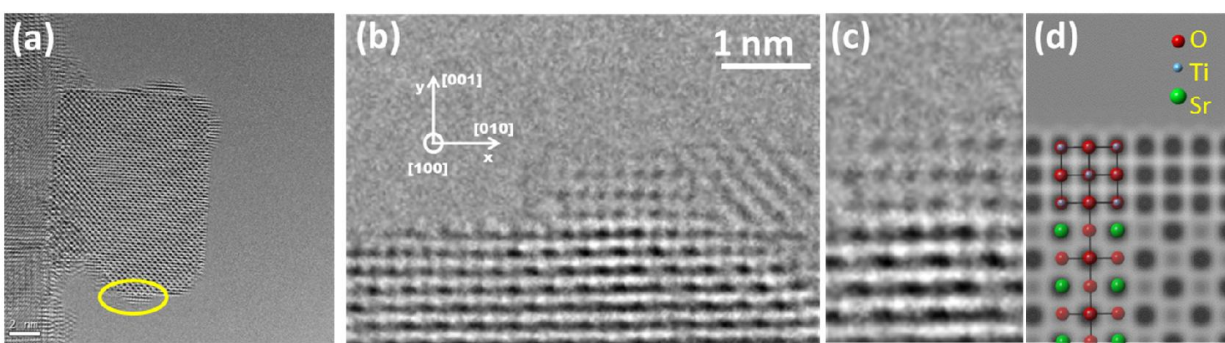


Figure 7.3 Atomic resolution HREM images showing the interfacial structure of TiO and SrO-terminated SrTiO<sub>3</sub>. (a) An experimental HREM image taken at a small underfocus condition. (b) A cropped and magnified images of (a). (c) A cropped and magnified image of (b). (d) The simulated HREM image of (c). The simulation parameters are thickness=3 nm, defocus=-2 nm, Cs=-5  $\mu\text{m}$ , convergence angle = 0.3 mrad, focal spread = 3.5 nm, vibration = 0.4  $\text{\AA}$  in both x and y directions. No astigmatisms, coma, and sample tilt were considered in the simulation. The lattice spacing for SrTiO<sub>3</sub> and TiO are all set to 4.1  $\text{\AA}$ , thus no lattice strain can be seen in the simulation.

In addition to the imaging characterization, EELS was conducted on the islands area to study the chemical composition, as shown in Fig. 7.4. The strongest Sr signal is at the low loss region (Sr-N<sub>2,3</sub> edge) while the strongest Ti signal is at the core loss region (Ti-L<sub>2,3</sub> edge). As the quantification for the low loss region is rather difficult (low signal-to-noise ratio and less well-

defined background models [180]), the ratio of Sr to Ti is not available. To overcome this obstacle, the EELS measurement was also conducted on the bulk SrTiO<sub>3</sub> part to obtain a reference. Compared to the SrTiO<sub>3</sub> bulk region (region 1 in Fig. 7.4(a)), the island region (region 2 in Fig. 7.4(a)) has much less Sr, as shown in Fig. 7.4(b). Owing to the smaller thickness, the absolute counts of the Ti-L<sub>2,3</sub> edge at the island region are fewer than that at the SrTiO<sub>3</sub> bulk region, as shown in Fig. 7.4(c). However, the EELS quantification shows there is a significant increase of Ti to O ratio at the island region.

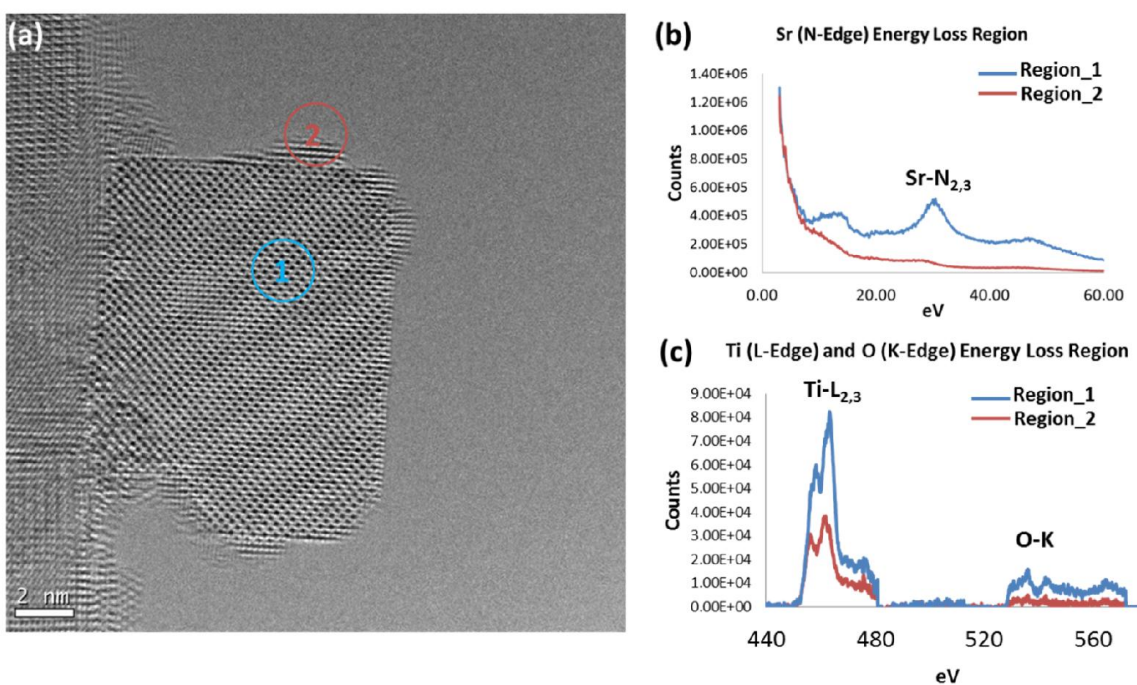


Figure 7.4 EELS results on the islands and bulk regions of beam-damaged SrTiO<sub>3</sub> nanocuboids. (a) Illustration of the regions conducted EELS measurements. (b) and (c) are EELS results showing the difference of Sr N-edge, Ti L-edge, and O K-edge of the two regions as indicated in (a).

A small portion of the islands have other structures while the majority of islands have a rocksalt TiO phase. Fig. 7.5(a) and (b) are magnified images of the top and bottom parts of Fig. 7.4(a). In Fig. 7.5(a), all the islands have a rocksalt TiO structure, as indicated by the yellow arrows. In this image, it is clear that the islands have a larger lattice spacing than that of the SrTiO<sub>3</sub>. In 7.5(b), the right island has a lattice spacing of  $\sim 3.3\text{\AA}$ , which is significantly smaller than the spacing of  $\{100\}$  planes of TiO and SrTiO<sub>3</sub>. In addition, the island has a checkerboard style lattice pattern, which is different from the cub-on-cube pattern of the TiO islands. After checking all the strontium oxides, titanium oxides, and Ruddlesden-Popper phases, only the bcc-type Ti can have the lattice pattern and lattice parameter. Fig. 7.5(c) and (d) show the simulated HREM images with different focus and thickness. Although the contrasts are changing because of the different thickness and defocus, the lattice pattern does not change. Therefore, the checkerboard style lattice pattern is intrinsic, not due to the HREM artifacts. By investigating the Ti-O binary phase diagram [181], the bcc-Ti is found to be stable with a small amount O dissolved in to form a solid solution. Therefore, strictly speaking the bcc-Ti islands are TiO<sub>x</sub> island, with the  $x < \sim 0.08$ . The presence of bcc-Ti islands may a result of further reduction of TiO islands.



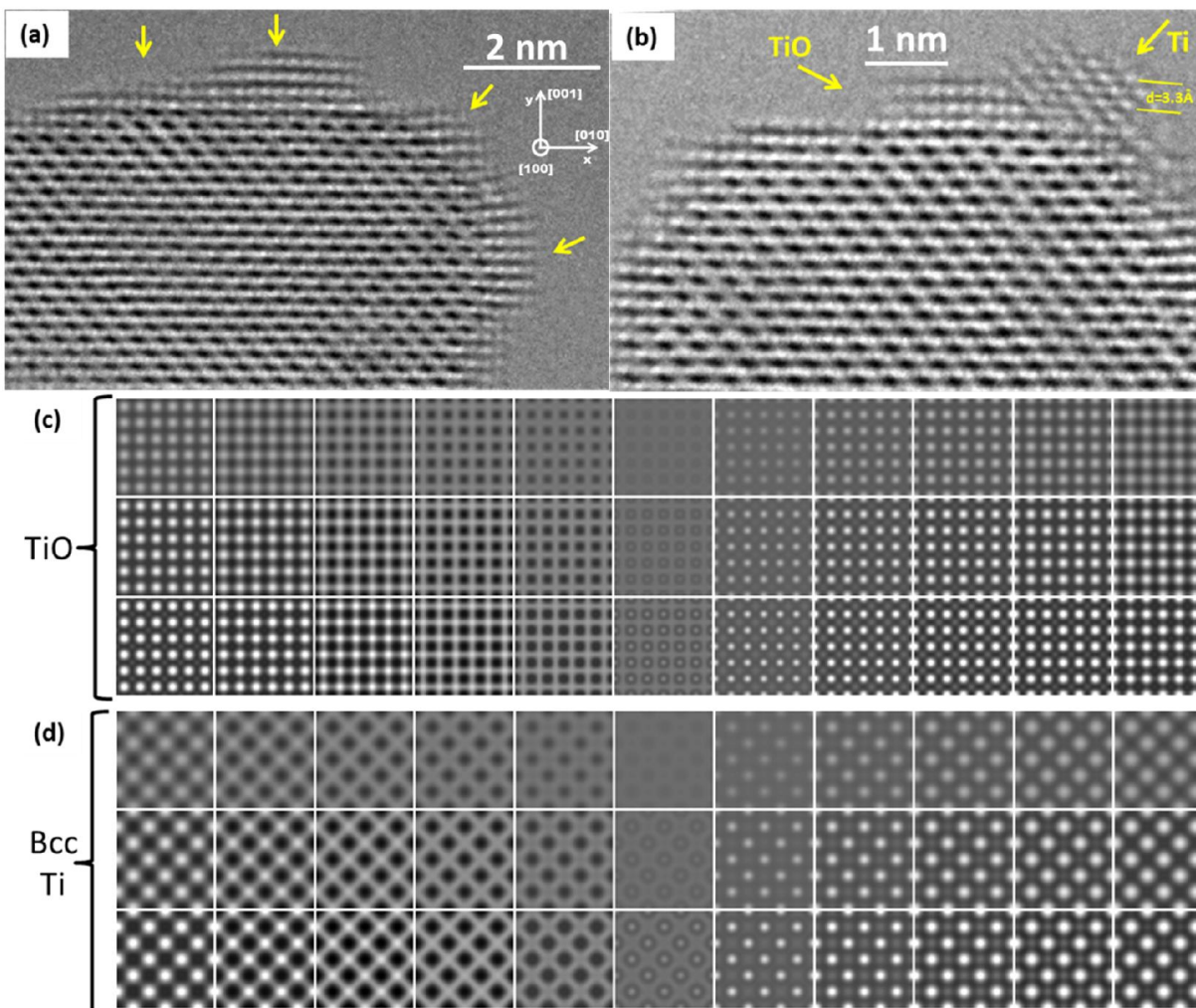


Figure 7.5 Comparison between TiO and Ti islands. (a) An experimental image showing TiO islands on the SrTiO<sub>3</sub> surfaces. (b) A Ti island beside a TiO island. (c) A series of simulated HREM images with thickness changes vertically from 1 nm on top to 3 nm on the bottom and defocus changes horizontally from -10 nm on the left to 10 nm on the right. Each image represents a 3×3 cell in the [100] zone axis. (d) The simulated HREM images with the same setting of (c) except using a bcc-Ti model. The simulation parameters other than the thickness and defocus are the same as the ones used in Fig. 7.3.

### 7.3.1 Beam damage

The Ti-rich surface segregation in this study is very similar to that in previous high temperature annealing studies done on SrTiO<sub>3</sub> surfaces under reduction conditions [173-176]. The high vacuum of TEM column as well as the electron beam irradiation can almost for certain create a

strong reduction environment. However, the estimated temperature increase due to beam induced heating using the inelastic scattering model is only a few degrees [182]. The predominating electron beam impact on the surface segregation is not beam induced heating, but radiolysis (ionization damage). Radiolysis in transition oxides can be qualitatively understood by the Knotek-Feibelman mechanism [183-185]. The electron irradiation excites a core level electron of the metal and creates a core level hole. The electrons at the valence level of the oxygen atoms transit to occupy the core hole, leaving the O atoms neutral or positively charged. This is an Auger process. The neutral or positive O atoms can then be ejected to the vacuum rather easily.

In addition to the surface segregation, other types of beam damage such as hole-drilling have been observed. The hole-drilling in this study is a direct result of applying a converged beam on the nanocuboids. Fig. 7.6 shows an example of the areas where the converged beam was applied. Usually SrTiO<sub>3</sub> is a rather robust material under the TEM electron beam, the severe electron induced surface segregation should be due to the high electron flux as well as the clean surface of the nanocuboids. The high flux can be avoided in careful TEM experiments. In a previous study, it was shown that surface segregation occurred after the removal of amorphous carbon film contamination [173]. It is known that a thin coating such as an amorphous film on a surface will reduce radiolytic damage by an order of magnitude [186]. The nanocuboids in this study, which are washed thoroughly in ethanol in this study, are usually very clean [41].

To obtain intrinsic surface structures, beam damage should be avoided. Beam damage is more severe in the recent aberration corrected TEM where high dose electron beam is often used. For the present SrTiO<sub>3</sub> case, it is now clear that the damaged sample has islands formation on the surface. For reducible oxides, such as WO<sub>3</sub> [187] and Ti<sub>2</sub>Nb<sub>10</sub>O<sub>29</sub> [188], the damaged material

can show thin metallic layers on the surfaces. For some the oxide supported metal catalyst systems, such as Au-TiO<sub>2</sub>, the Au particles can be encapsulated or pillared by the support oxides with electron beam irradiation [189]. For a more comprehensive review of beam damage, Dr. Rebecca Ai and Mary Buckett's theses at Northwestern University are good references. To reduce the beam damage, the acceleration voltage or total electron dose can usually be tuned for different materials. The higher voltage can reduce the ionization damage, while knock-on damage is more severe. In contrast, the lower voltage can alleviate the knock-on damage, while the ionization damage is more severe. An alternative approach is to reduce the total dose. The signal-to-noise ratio in the low dose imaging is low; however, the technique exit wave reconstruction (EWR) [190, 191] can numerically enhance the signal-to-noise ratio by utilizing a set of low dose images.



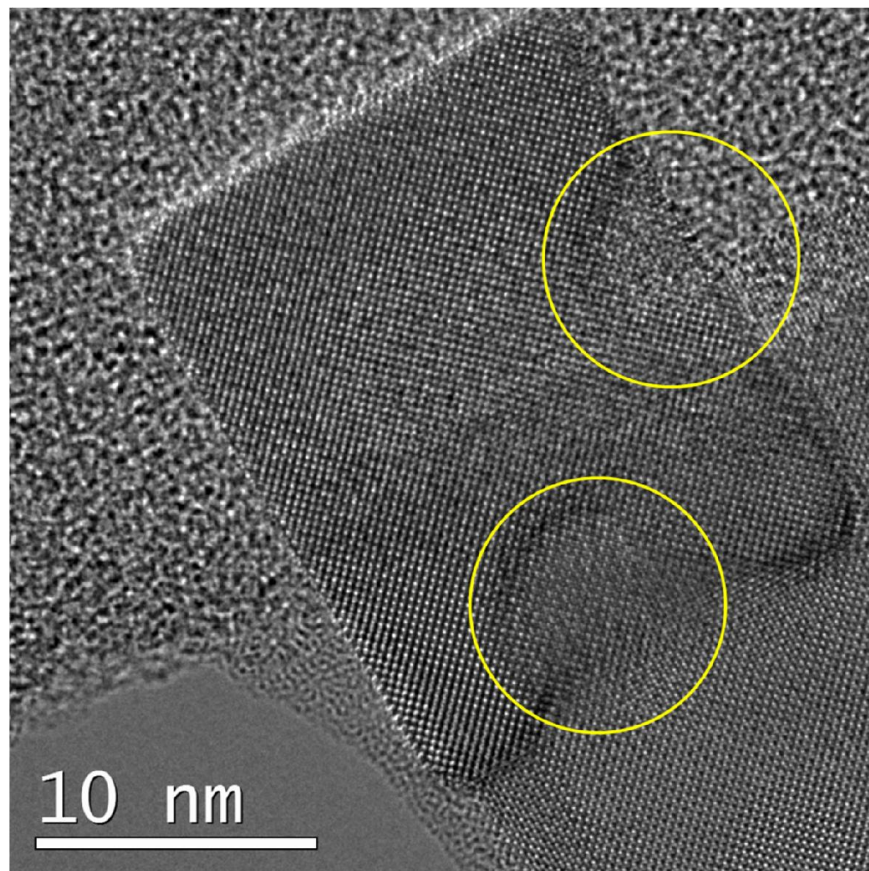


Figure 7.6 Illustration of the beam damage on a SrTiO<sub>3</sub> nanocuboid. The two yellow circles indicate the hole-drilling effect by a converged electron probe.

### 7.3.2 Mechanisms for the Surface Segregation

The Ti- or Sr-rich surface segregations are usually attributed to the diffusion of point defects under oxidation and reduction conditions. However, the mechanisms of the segregations are not clear. Herein, possible mechanisms are proposed in this study, as shown in Fig. 7.7.

It has been shown that the Sr and O vacancies ( $V_{\text{O}}^{\bullet\bullet}$  and  $V_{\text{Sr}}^{\prime\prime}$ ) are the predominant vacancies in SrTiO<sub>3</sub>. Moreover, the  $V_{\text{O}}^{\bullet\bullet}$  and  $V_{\text{Sr}}^{\prime\prime}$  should be localized in a complex form [192, 193]. Otherwise, an electron-hole pair should be created to balance the charge. As SrTiO<sub>3</sub> is an insulator with a

band gap of 3.7eV, the energy required to create an electron-hole pair is rather high. Creating complexes of  $V_O^{\bullet\bullet}$  and  $V_{Sr}^{\prime\prime}$  requires much lower energy, which has been confirmed by experiments and DFT calculations. This argument is equivalent to the Columbic attraction between the  $V_O^{\bullet\bullet}$  and  $V_{Sr}^{\prime\prime}$ , as they are positively and negatively charged. The Columbic attraction can drive them to form complexes.

Under oxidation conditions, the surface  $V_O^{\bullet\bullet}$  vacancies are eliminated. The remaining surface  $V_{Sr}^{\prime\prime}$  is not stable and will diffuse into the bulk or form clusters on the surface. As the  $V_{Sr}^{\prime\prime}$  diffuse away, the Sr atoms diffuse in, which results in the local surface Sr-rich cluster or islands. Under reduction conditions, large amount of surface  $V_O^{\bullet\bullet}$  and  $V_{Sr}^{\prime\prime}$  are created. The enrichment of  $V_O^{\bullet\bullet}$  and  $V_{Sr}^{\prime\prime}$  results in the enrichment of surface Ti species. The equilibrium concentration and diffusion rate of thermally-activated point defects at room temperature are exceedingly low. The concentration and diffusion are much higher with high temperature or assisted by the electron irradiation. The exact shape of the segregation, such as islands, layers, and needles, should be attributed to the surface energy of the islands and the interface energy between the islands and substrates.

A key factor controlling the enriched surface species to form reconstructions or islands is the chemical potential. For the well-documented  $TiO_2$  double layer surface reconstructions, the Ti surface enrichment is probably relatively low. For the higher surface Ti enrichment, formation of islands is more likely to occur. It seems that additional layers are present locally at the early stages of electron beam irradiation on the surface, as indicated by the arrows in Fig. 7.3(a) and (b). As the Ti-rich surface species increase, the atoms at the local additional layer agglomerate

and form islands. The DFT study performed by Heifetz et al. confirms the formation of Ti-rich precipitates at low O pressure and high temperature is energetically favorable [194].

This study may explain the rich family of surface structures of SrTiO<sub>3</sub>. For the surface reconstructions observed by TEM, the samples are usually argon ion milled [45, 47, 81, 95]. Similar to electrons, the argon ion irradiation can also create point defects in SrTiO<sub>3</sub>. The exact condition of ion milling, such as the energy and the angle of ion milling, may cause different amounts of surface Ti enrichment. The coverage of excessive Ti compared to the intrinsic SrTiO<sub>3</sub> surface may result in different surface structures. For the STM experiments, the SrTiO<sub>3</sub> specimen are usually etched in buffered NH<sub>4</sub>F solution or sputtered by argon ions, which will also alter the surface chemistry of SrTiO<sub>3</sub> [25]. If the explanation is correct, surface structures of SrTiO<sub>3</sub> and other materials can be controlled precisely by inducing a certain amount of excess material, which is very useful for technological applications.

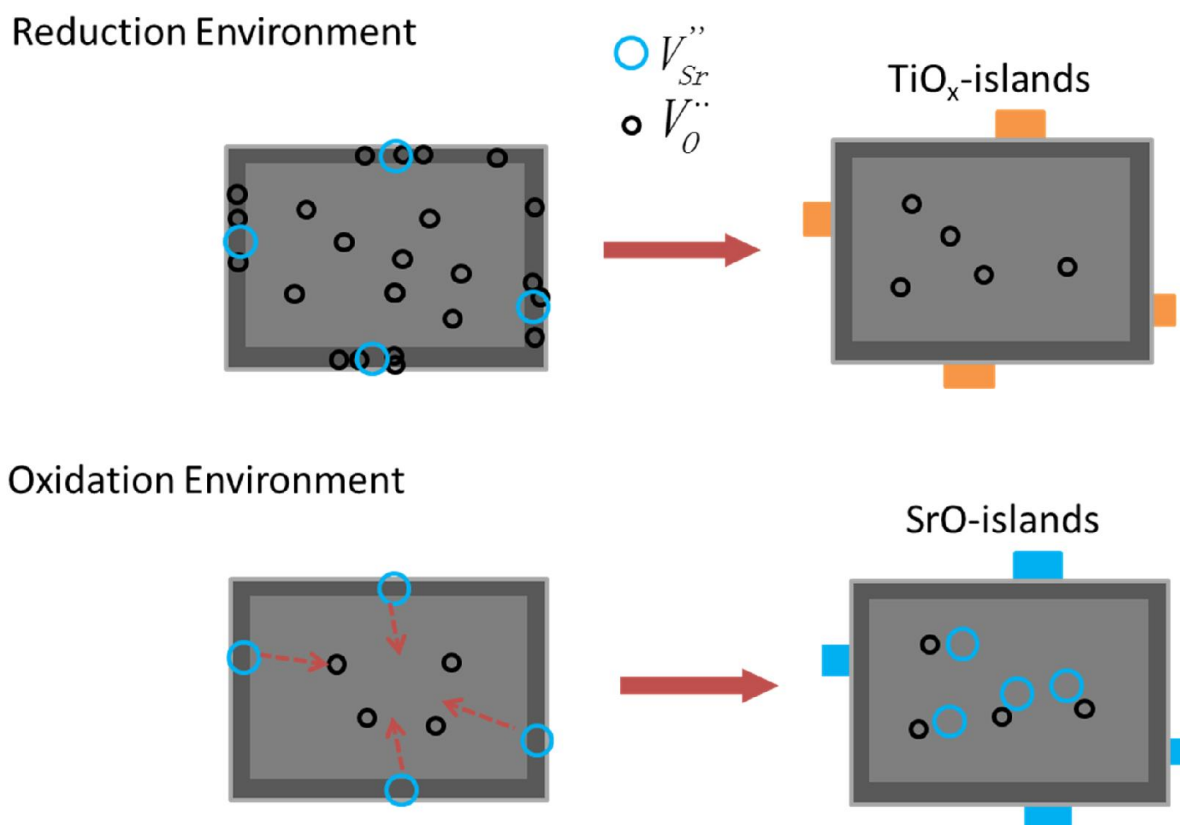


Figure 7.7 Mechanisms of the formation of Sr- and Ti-rich surface segregations under reduction and oxidation environment.

#### 7.4 Summary

Under electron beam irradiation, Ti-rich surface islands are formed. The Ti-rich islands are determined by HREM and EELS. The majority of the islands have a rocksalt TiO phase. A small portion of them are bcc-type Ti islands. The electron beam irradiation readily creates a large amount of O vacancies, which is a standard beam damage and can be qualitatively understood by the Knotek-Feibelman mechanism. The surface segregation can be explained by the diffusion of point defects. The  $V_O''$  and  $V_{Sr}''$  are predominant vacancies in SrTiO<sub>3</sub> and are in a complex form. The enrichment of  $V_O''$  and  $V_{Sr}''$  result in Ti-rich surfaces. The concentration and diffusion of the

point defects are enhanced by the electron beam irradiation. The formation of island type Ti-rich surfaces instead of double  $\text{TiO}_2$  layer reconstructions are related to the excess amount of surface Ti and surface energies. This study may explain the rich surface phenomena of  $\text{SrTiO}_3$ . The reported surface reconstructions of  $\text{SrTiO}_3$  are usually after argon ion irradiation or acid etching. The surface reconstructions are sensitive to argon irradiation or acid etching. The argon ion irradiation can create point defects and generate different amounts of surface excess Ti. The annealing conditions further complicate the surface chemistry, which results in a variety of surface reconstructions. This study may be qualitatively extendable to the surfaces of other materials.

## 8. Ongoing Projects and Future Directions

### 8.1 Ongoing Projects

#### 8.1.1 On the Plan-view HREM Surface Imaging

Plan-view HREM imaging for surface is usually not as convenient as profile-view imaging. However, it is almost impossible to solve a complex surface reconstruction based on the edge-on contrast in profile-view surface imaging. The ideal scenario for plan-view surface imaging is that there is a one-to-one correspondence of the spots in HREM image and the surface atom position. This ideal scenario is not easy to obtain. The most difficult issue is the convolution of the signals of the top and bottom surfaces as well as that of the bulk structure [195]. The deconvolution requires extensive image processing and simulation. In this study, the procedures of plan-view surface imaging are investigated. Furthermore, the validity of plan-view HREM surface imaging is tested with different specimen thickness.

In this study, an artificial atomic model of  $\text{SrTiO}_3(111)-(3 \times 3)$  reconstruction with a  $p3m1$  symmetry is used as a study system. Fig. 8.1(a) shows the atomic model of the artificial surface. Fig. 8.1(b) shows the atomic model of a realistic  $\text{SrTiO}_3$  specimen, in which there is a top and bottom surfaces with bulk  $\text{SrTiO}_3$  between them. In addition, there is a relative planar translation between the top and bottom surfaces, as it is not necessary for the two surfaces to have a zero translation.

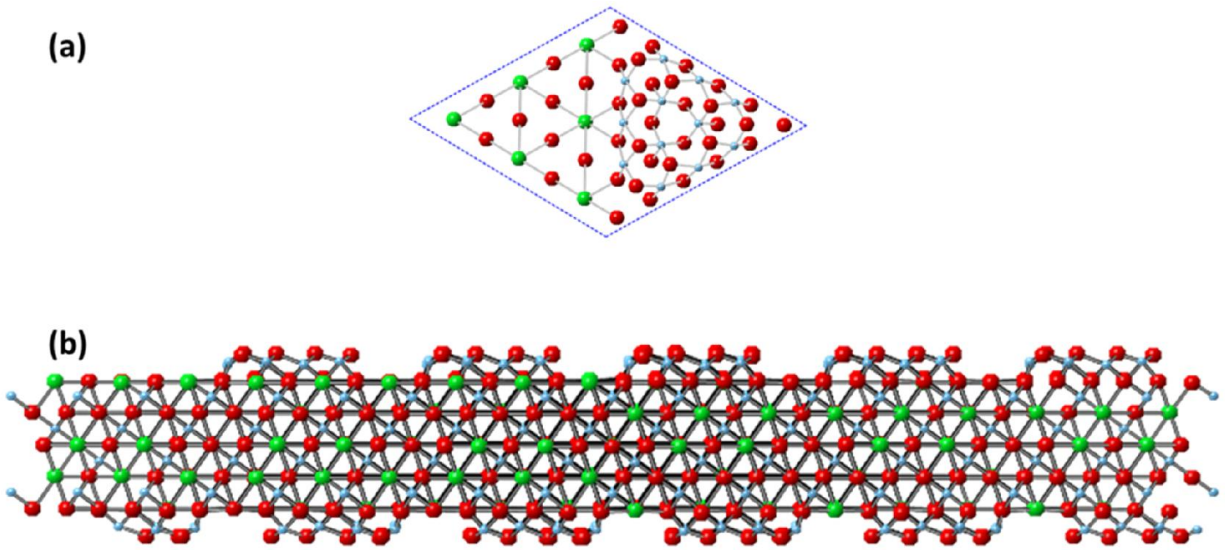


Figure 8.1 Atomic models of an artificial (3×3) surface reconstruction on SrTiO<sub>3</sub>(111).

Fig. 8.2 shows a typical process of image processing for the plan-view HREM surface images. The most important assumption is that the surface structures of the top and bottom surfaces are the same except for the relative translation. Owing to the p3m1 symmetry of the surface reconstruction, there is an 180° rotation between the top and bottom surfaces. In addition, the bulk registry indicates 27 (4 independent ones due to the p3m1 symmetry) possible translations. This is calculated by the surface reconstruction area (9 bulk unit cells) times by the 3 possible stackings along the [111] direction (the ABCABC stacking). In Fig. 8.1, only the (1/3, 1/3) translation is illustrated. A translation ( $\mathbf{t}$ ) in real space indicates a phase shift in reciprocal space.

$$I(\mathbf{r} + \mathbf{t}) + I(-\mathbf{r}) \xrightarrow{FT} I(\mathbf{u}) \cdot \exp(i2\pi\mathbf{u} \cdot \mathbf{t}) + I(\mathbf{u})$$

If an individual reflection from a single surface is written as

$$e_{\mathbb{I}} = A_{\mathbb{I}} \exp(i\phi_{\mathbb{I}}),$$

where  $A_{IJ}$  is the amplitude and  $\varphi_{IJ}$  is the phase.

An individual reflection from an overlapped surface is then written as

$$e_{ij}=A_{IJ}\{\exp(-i\varphi_{IJ}+2\pi i\mathbf{d}\cdot\mathbf{g})+\exp(i\varphi_{IJ}+2\pi i(\mathbf{d}+\mathbf{t})\cdot\mathbf{g})\},$$

where  $\mathbf{t}$  is the relative translation between the top and bottom surfaces,  $\mathbf{d}$  is the origin position which maximizes the p3m1 symmetry of image, and  $\mathbf{g}$  is the reciprocal vector of each reflections.

The amplitude and phase of  $e_{ij}$  can be measured from the FFT of the image. Moreover, there is a symmetry requirement of the phases and amplitudes of the reflections from a single surface layer.

The equation can be solved by optimizing  $d$  to obtain the lowest R1 factor of the symmetry equivalent spots. R1 is defined as

$$R1 = \frac{\sum_{IJ} |e_{IJ} - m_I|}{\sum_{IJ} |e_{IJ}|}$$

where  $m_I$  is the averaged reflection of the symmetry equivalent reflections. With the correct phases and amplitudes of the reflections from a single layer surface available, the real space image can be obtained by performing the inverse FFT. Fig. 8.2 shows the image after the inverse FFT is very similar to the processed image with 170 reflections. This indicates the algorithm works for an overlapped surface with a planar translation.



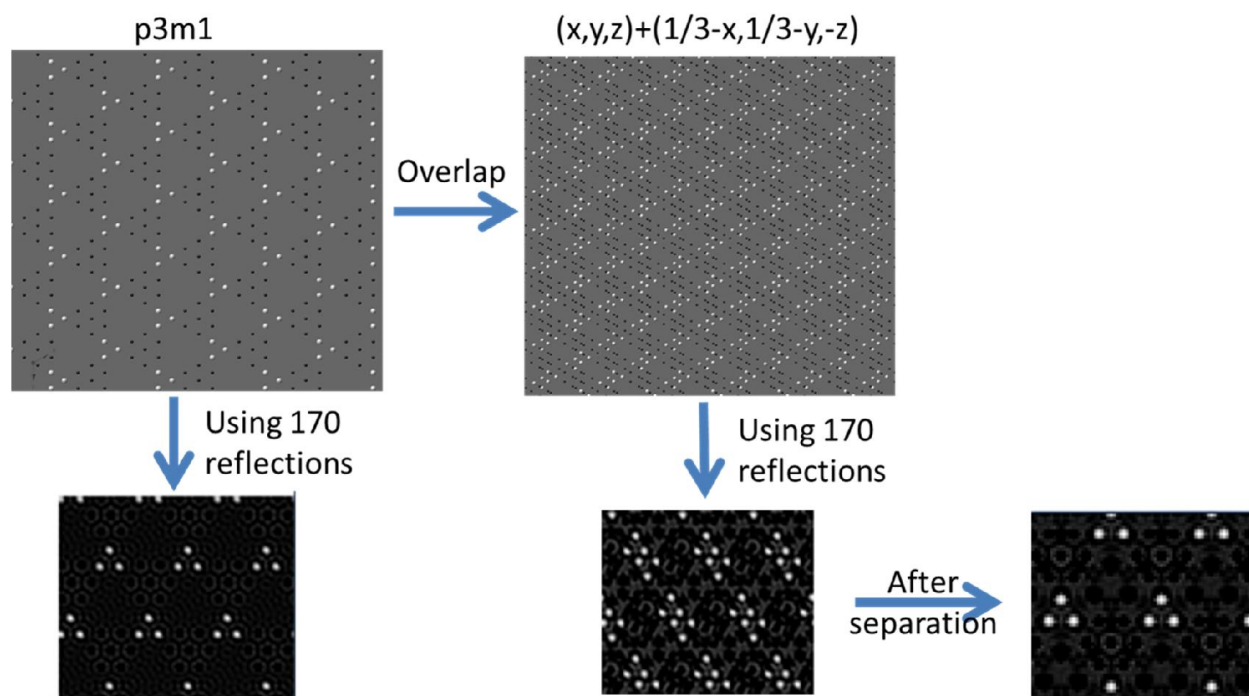


Figure 8.2 Illustration of the imaging processing in plan-view HREM surface imaging.

However, the above test case does not take the HREM imaging contrast into account. As the top and bottom surfaces are separated with a finite distance in the  $z$  direction and the bulk material is filled between them, the assumption of the same contrast between the top and bottom surfaces can be very wrong in HREM images. Fig. 8.3 shows the simulated HREM images of a single  $(3 \times 3)$  surface layer in a focal series. There is a one-to-one correspondence of the spots in the images to the atom position. However, there is a contrast reversal of the image with 0 nm and 20 nm defocus. As a result, the top and bottom surfaces cannot have the same HREM contrast with too much separation in the  $z$  direction. This is an essentially an effect of defocus.

In addition, the bulk material may also have an impact on the validity of plan-view images. The bulk material provides the channels for the transmitting electrons. Whether or not the channeling

effect [71] will induce a different contrast on the top and bottom surfaces is unknown. In order to take the impact of bulk material into account, HREM simulation was performed using the atomic models similar to Fig. 8.2(b) with changes in the thickness of the bulk material.

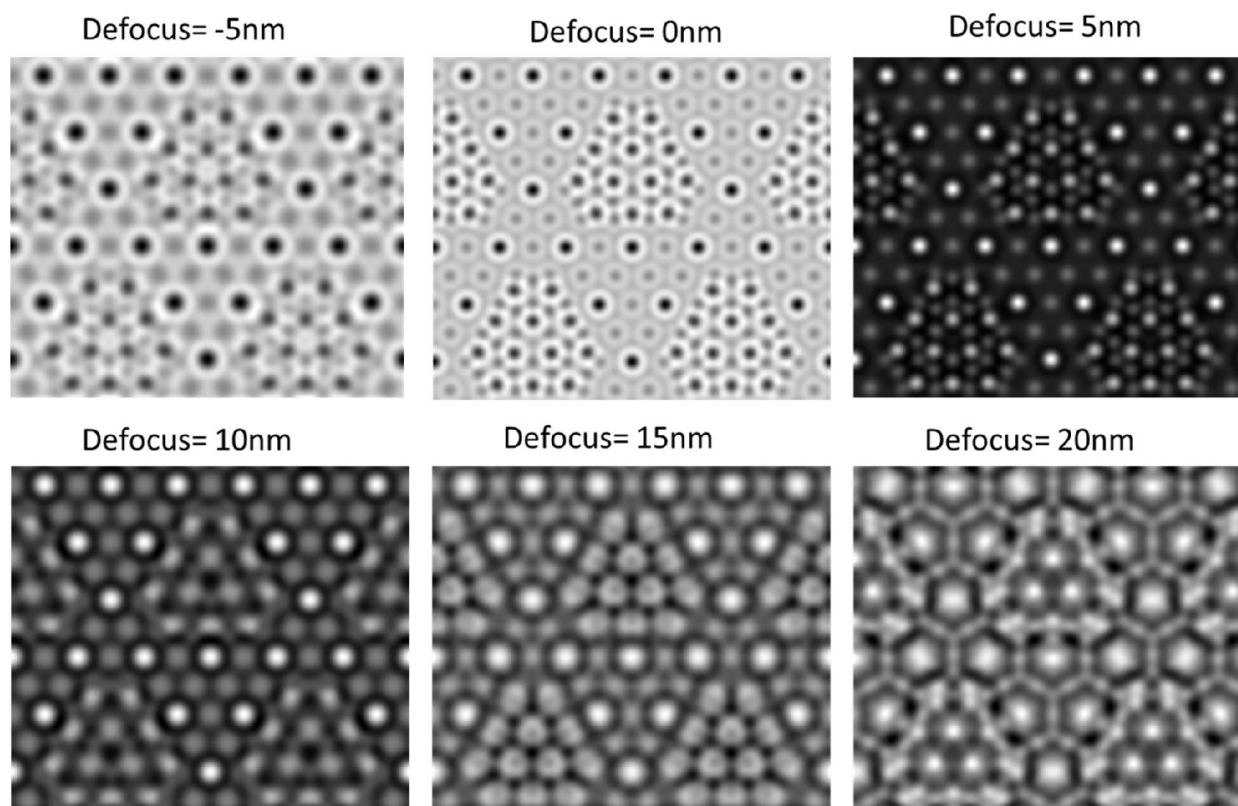


Figure 8.3 Simulated HREM images of a single layer artificial  $\text{SrTiO}_3(111)-(3 \times 3)$ . The atomic structure is shown in 8.1(a).

Fig. 8.4 shows the results of the processed HREM image. The process images are able to retrieve the single surface signals with the thickness up to 13 nm. If the thickness is higher than 13 nm, the algorithm does not work, which indicates the assumption of the same contrast of the top and bottom surfaces does not hold. It is worth noting that the critical thickness for valid plan-view HREM surface imaging is obtained with the defocus of the entire specimen at 5 nm. By

decreasing the defocus, the critical thickness can be decrease to 7 nm. Therefore, the thickness coupled with the defocus play an important role in the HREM contrast of the top and bottom surfaces.

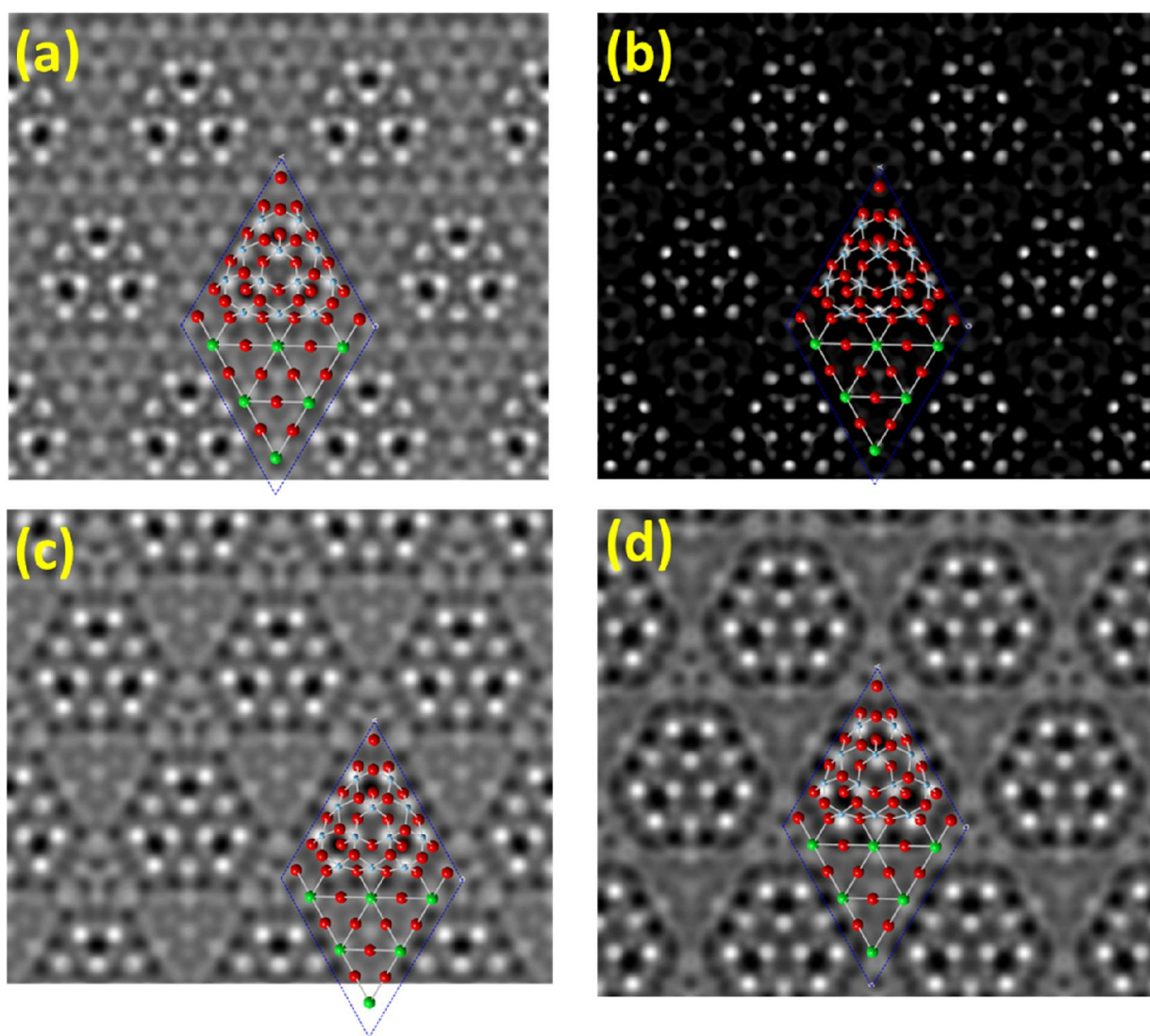


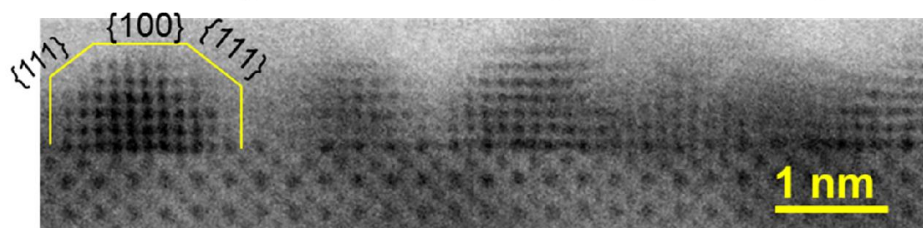
Figure 8.4 The HREM images obtained after the separation of the top and bottom surfaces. (a)-(d) Separated single surface images from the models with bulk thickness of 1 nm, 5 nm, 9 nm, and 13 nm.

### 8.1.2 From Atomic Surface Structures to Catalytic Properties—Pt on SrTiO<sub>3</sub> Nanocuboids

As discussed in chapter 6, different hydrothermal synthetic methods can control the atomic surface structures of SrTiO<sub>3</sub> nanocuboids [41]. If oleic acid was added during the synthesis, the surface of SrTiO<sub>3</sub> nanocuboids is SrO terminated. In contrast, if the acetic acid was added, the surface of the nanocuboids is terminated by TiO<sub>2</sub>-rich reconstructions. If the hydrothermal process was conducted in a microwave oven instead of a traditional oven, the surface has both TiO<sub>2</sub>-rich reconstructions and SrO terminations.

In principle, the TiO<sub>2</sub> and SrO terminations can play important roles in catalysis. A study on SrTiO<sub>3</sub> single crystal surface suggested that the exposed facets of Pt nanoparticles grown on TiO<sub>2</sub> or SrO termination of SrTiO<sub>3</sub> (100) surface are different [23]. A TiO<sub>2</sub> termination results in a cube-on-cube epitaxial growth of Pt nanoparticles with a WinterBottom shape [160]. A SrO termination can cause a rotation of the Pt nanoparticle with a [111] epitaxial growth direction [23]. The TiO<sub>2</sub> termination should result in the Pt nanoparticles with a higher {100} to {111} ratio compared to that from the SrO termination. Catalytic studies have shown the activity and selectivity of many reactions are different on Pt (100) and (111) surfaces [44, 196]. The Pt nanoparticles can be deposited on SrTiO<sub>3</sub> nanocuboids with different surface terminations using atomic layer deposition (ALD), as details in Ref [197]. The shapes and structures of Pt nanoparticles deposited on SrTiO<sub>3</sub> surfaces were discussed in refs [23, 160, 198]. Fig. 8.5 shows atomic resolution STEM images of the Pt-SrTiO<sub>3</sub> systems. Clearly, the shapes and epitaxial directions of the Pt nanoparticles are very different on the SrO-rich and TiO<sub>2</sub>-rich SrTiO<sub>3</sub> nanocuboids.

### Pt on SrTiO<sub>3</sub> nanocuboids (TiO<sub>2</sub> surface)



### Pt on SrTiO<sub>3</sub> nanocuboids (SrO surface)

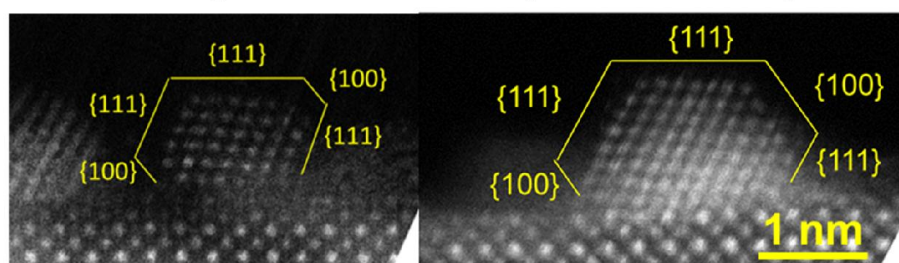


Figure 8.5 Atomic resolution STEM images of Pt on SrTiO<sub>3</sub> nanocuboids with different terminations. Top: An ABF image shows the Winterbottom shapes of Pt with a cube-on-cube epitaxy on a SrTiO<sub>3</sub> nanocuboid with a SrO termination. Bottom: Top: A HAADF image shows the Winterbottom shapes of Pt with a rotated epitaxy direction on a SrTiO<sub>3</sub> nanocuboid with TiO<sub>2</sub>-rich surfaces.

We have performed a preliminary catalytic test of CO oxidation reaction at O-rich condition, as shown in Fig. 8.6. The SrO termination has approximately 100% more activity than that of TiO<sub>2</sub> terminated SrTiO<sub>3</sub> nanoparticles using the same amount of Pt. The different activities indicate the shape of Pt and the atomic surface structures of the supports can have important impacts on the catalytic properties. For a comprehensive understanding of the catalytic mechanism, more studies should be conducted.

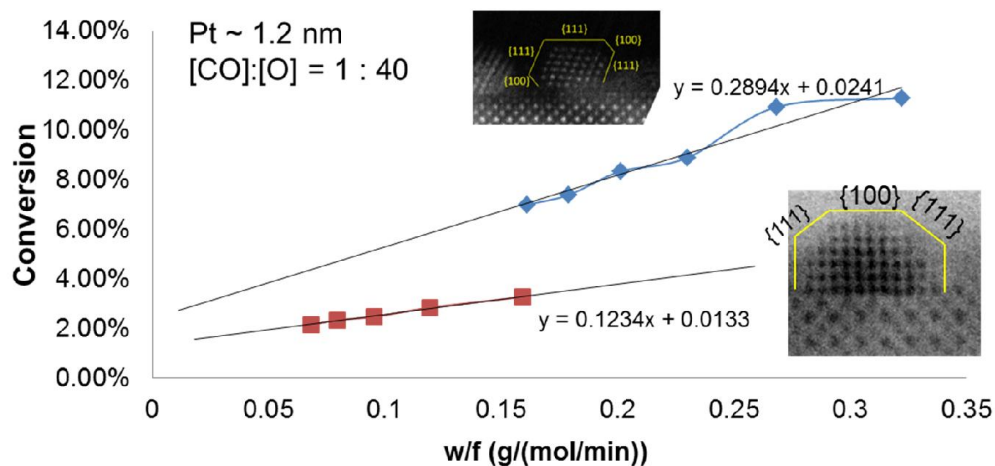


Figure 8.6 Catalytic results of Pt on SrTiO<sub>3</sub> nanocuboids with different surface terminations. The Pt on SrO-terminated SrTiO<sub>3</sub> nanocuboids demonstrates higher activity in CO oxidation in an O-rich condition ([CO]: [O]=1: 40).

## 8.2 Future Directions

### 8.2.1 Catalysts with Well-defined Shapes

As the atomic surface structures of CeO<sub>2</sub> are clearly observed in this study, it would be very interesting to investigate the catalytic properties of CeO<sub>2</sub> nanostructures. The Au on CeO<sub>2</sub> nanocubes, nanorods, and nanooctahedra are good model systems to start with. The three systems often show different catalytic properties in different reactions [199]. It is very important to understand the catalysis from the atomic structures. Obtaining the CeO<sub>2</sub> nanostructures are relatively easy by using the hydrothermal methods. The Au nanoparticles supported on the CeO<sub>2</sub> nanostructures can be obtained by the deposition-precipitation method. The shape of Au and the interface between the Au and CeO<sub>2</sub> can be clearly imaged by aberration corrected STEM. The microscopic studies can also be compared to the structures derived by some spectroscopic studies such as FT-IR. In addition to the atomic structure, XPS and other techniques can be used

to understand the electronic structures. With both atomic and electronic structures obtained, the catalysis can be understood comprehensively.

### **8.2.2 Bimetallic Catalysts**

The bimetallic system opens a door for future studies of catalysis. The bimetallic catalysts have multiple advantages such as to reduce the usage of expensive material, enhance stability, and improve catalytic activity or selectivity [200]. For example, some bimetallic catalysts have a core-shell structure [201, 202]. The shell materials can have the thickness of only a few atom layers, which still preserves the majority of the catalytic properties. This helps to reduce the cost by only using the shell material as the catalyst. Moreover, the catalytic properties of the shell materials can be tuned by the core materials based on the different lattice spacings or structures. The underlying mechanism is the d-band theory which was developed by Norskov et al. using DFT [203-205]. A compressive strain on the shell materials can result in a downward shift of the center of the d-band, which can reduce the adsorption of reactants [203-206]. An expansive strain would do the opposite. This may or may not improve the overall catalysis depending on whether or not the adsorption or desorption is the rate determining step [207, 208]. Therefore, catalysts in the future are not limited by the metals with single elements, but can be further developed by tuning the configurations with different metals.

### **8.2.3 Single Atom Catalysts**

The single atom catalysts have been studied on metal organic frameworks, oxide supports and metals [209]. The extremely low loading of catalysts not only reduces the cost, but some single atom catalysts also show significantly enhanced activities for some reactions while the atoms can still be well-separated after hundreds of reaction cycles [210, 211]. The strong anchoring sites

provided by the support can be attributed to the stabilization. The enhanced catalytic activities are attributed to the electron transfer between the metal atoms and supports. Many metal-support systems have demonstrated that the strong anchored metal atoms are positively charged [211-219]. The impact of support on the electronic structures is more significant due to the extremely small dimension. Therefore, by designing the support surfaces for single atom materials, further development of catalysis is expected. On the characterization side, electron microscopy, particularly the Z-contrast HAADF-STEM enables the confirmation of single atom dispersion as well as visualization of the anchoring sites.



## Reference

1. Takei, T., T. Akita, I. Nakamura, T. Fujitani, M. Okumura, K. Okazaki, J. Huang, T. Ishida, and M. Haruta, in *Advances in catalysis*, C.G. Bruce and C.J. Friederike, Editors. 2012, Academic Press. p. 1-126.
2. Liu, X.Y., A. Wang, T. Zhang, and C.-Y. Mou, *Nano Today*, 2013. **8**(4): p. 403-416.
3. Linsebigler, A.L., G. Lu, and J.T. Yates, *Chemical Reviews*, 1995. **95**(3): p. 735-758.
4. Nakata, K. and A. Fujishima, *Journal of Photochemistry and Photobiology C: Photochemistry Reviews*, 2012. **13**(3): p. 169-189.
5. Trovarelli, A., *Catalysis Reviews*, 1996. **38**(4): p. 439-520.
6. Hu, L., K. Sun, Q. Peng, B. Xu, and Y. Li, *Nano Research*, 2010. **3**(5): p. 363-368.
7. Xie, X., Y. Li, Z.-Q. Liu, M. Haruta, and W. Shen, *Nature*, 2009. **458**(7239): p. 746-749.
8. Sum, R., R. Lüthi, H.P. Lang, and H.J. Güntherodt, *Physica C: Superconductivity*, 1994. **235–240, Part 1**(0): p. 621-622.
9. Ohtomo, A., D.A. Muller, J.L. Grazul, and H.Y. Hwang, *Nature*, 2002. **419**(6905): p. 378-380.
10. Thiel, S., G. Hammerl, A. Schmehl, C.W. Schneider, and J. Mannhart, *Science*, 2006. **313**(5795): p. 1942-1945.
11. Jia, C.-L., V. Nagarajan, J.-Q. He, L. Houben, T. Zhao, R. Ramesh, K. Urban, and R. Waser, *Nature Materials*, 2007. **6**(1): p. 64-69.
12. Jia, C.-L., S.-B. Mi, K. Urban, I. Vrejoiu, M. Alexe, and D. Hesse, *Nature Materials*, 2008. **7**(1): p. 57-61.
13. Madsen, B.D., W. Kobsiriphat, Y. Wang, L.D. Marks, and S.A. Barnett, *Journal of Power Sources*, 2007. **166**(1): p. 64-67.

14. Chueh, W.C., Y. Hao, W. Jung, and S.M. Haile, *Nature Materials*, 2012. **11**(2): p. 155-161.
15. Matsuda, T., Y. Yoshida, K. Mitsuhashi, and Y. Kido, *The Journal of Chemical Physics*, 2013. **138**(24): p. 244705-10.
16. Kobsiriphat, W., B.D. Madsen, Y. Wang, L.D. Marks, and S.A. Barnett, *Solid State Ionics*, 2009. **180**(2-3): p. 257-264.
17. Makar, G.L. and J. Kruger, *International Materials Reviews*, 1993. **38**(3): p. 138-153.
18. Lu, W.-K., R.L. Elsenbaumer, and B. Wessling, *Synthetic Metals*, 1995. **71**(1-3): p. 2163-2166.
19. Conway, B.E., *Progress in Surface Science*, 1995. **49**(4): p. 331-452.
20. Cook, L.M., *Journal of Non-Crystalline Solids*, 1990. **120**(1-3): p. 152-171.
21. Feng, X., D.C. Sayle, Z.L. Wang, M.S. Paras, B. Santora, A.C. Sutorik, T.X.T. Sayle, Y. Yang, Y. Ding, X. Wang, and Y.-S. Her, *Science*, 2006. **312**(5779): p. 1504-1508.
22. Batzill, M. and U. Diebold, *Progress in Surface Science*, 2005. **79**(2-4): p. 47-154.
23. Polli, A.D., T. Wagner, T. Gemming, and M. Rühle, *Surface Science*, 2000. **448**(2-3): p. 279-289.
24. Kawasaki, M., A. Ohtomo, T. Arakane, K. Takahashi, M. Yoshimoto, and H. Koinuma, *Applied Surface Science*, 1996. **107**: p. 102-106.
25. Kawasaki, M., K. Takahashi, T. Maeda, R. Tsuchiya, M. Shinohara, O. Ishiyama, T. Yonezawa, M. Yoshimoto, and H. Koinuma, *Science*, 1994. **266**(5190): p. 1540-1542.
26. Muller, D.A., L.F. Kourkoutis, M. Murfitt, J.H. Song, H.Y. Hwang, J. Silcox, N. Dellby, and O.L. Krivanek, *Science*, 2008. **319**(5866): p. 1073-1076.
27. Ramirez, A.P., *Science*, 2007. **315**(5817): p. 1377-1378.

28. Ahn, C.H., K.M. Rabe, and J.-M. Triscone, *Science*, 2004. **303**(5657): p. 488-491.
29. Enterkin, J.A., W. Setthapun, J.W. Elam, S.T. Christensen, F.A. Rabuffetti, L.D. Marks, P.C. Stair, K.R. Poepelmeier, and C.L. Marshall, *ACS Catalysis*, 2011. **1**(6): p. 629-635.
30. Ratnasamy, C. and J.P. Wagner, *Catalysis Reviews*, 2009. **51**(3): p. 325-440.
31. Beckers, J. and G. Rothenberg, *Green Chemistry*, 2010. **12**(6): p. 939-948.
32. Vivier, L. and D. Duprez, *ChemSusChem*, 2010. **3**(6): p. 654-678.
33. Turner, S., S. Lazar, B. Freitag, R. Egoavil, J. Verbeeck, S. Put, Y. Strauven, and G. Van Tendeloo, *Nanoscale*, 2011. **3**(8): p. 3385-3390.
34. Namai, Y., K.-I. Fukui, and Y. Iwasawa, *Catalysis Today*, 2003. **85**(2-4): p. 79-91.
35. Ta, N., J. Liu, S. Chenna, P.A. Crozier, Y. Li, A. Chen, and W. Shen, *Journal of the American Chemical Society*, 2012. **134**(51): p. 20585-20588.
36. Ulrike Diebold, S.-C.L. and M. Schmid, *Annual Review of Physical Chemistry*, 2010. **61**: p. 129-148.
37. Claudine, N., *Journal of Physics: Condensed Matter*, 2000. **12**(31): p. R367.
38. Diebold, U., *Surface Science Reports*, 2003. **48**(5-8): p. 53-229.
39. Kienzle, D.M. and L.D. Marks, *CrystEngComm*, 2012. **14**(23): p. 7833-7839.
40. Yu, R., L.H. Hu, Z.Y. Cheng, Y.D. Li, H.Q. Ye, and J. Zhu, *Physical Review Letters*, 2010. **105**(22): p. 226101.
41. Lin, Y., J. Wen, L. Hu, R.M. Kennedy, P.C. Stair, K.R. Poepelmeier, and L.D. Marks, *Physical Review Letters*, 2013. **111**(15): p. 156101.

42. Lin, Y., Z. Wu, J. Wen, K.R. Poeppelmeier, and L.D. Marks, *Nano Letters*, 2014. **14**(1): p. 191-196.
43. Imbihl, R. and G. Ertl, *Chemical Reviews*, 1995. **95**(3): p. 697-733.
44. Kliewer, C.J., M. Bieri, and G.A. Somorjai, *Journal of the American Chemical Society*, 2009. **131**(29): p. 9958-9966.
45. Chiamonti, A.N., C.H. Lanier, L.D. Marks, and P.C. Stair, *Surface Science*, 2008. **602**(18): p. 3018-3025.
46. Enterkin, J.A., A.K. Subramanian, B.C. Russell, M.R. Castell, K.R. Poeppelmeier, and L.D. Marks, *Nature Materials*, 2010. **9**(3): p. 245-248.
47. Erdman, N., K.R. Poeppelmeier, M. Asta, O. Warschkow, D.E. Ellis, and L.D. Marks, *Nature*, 2002. **419**(6902): p. 55-58.
48. Yin, H., C. Wang, H. Zhu, S.H. Overbury, S. Sun, and S. Dai, *Chemical Communications*, 2008(36): p. 4357-4359.
49. Xie, H., J. Lu, M. Shekhar, J.W. Elam, W.N. Delgass, F.H. Ribeiro, E. Weitz, and K.R. Poeppelmeier, *ACS Catalysis*, 2012. **3**(1): p. 61-73.
50. Wen, L., J.-K. Fu, P.-Y. Gu, B.-X. Yao, Z.-H. Lin, and J.-Z. Zhou, *Applied Catalysis B: Environmental*, 2008. **79**(4): p. 402-409.
51. Moses-DeBusk, M., M. Yoon, L.F. Allard, D.R. Mullins, Z. Wu, X. Yang, G. Veith, G.M. Stocks, and C.K. Narula, *Journal of the American Chemical Society*, 2013. **135**(34): p. 12634-12645.
52. Wu, Z., M. Li, J. Howe, H.M. Meyer, and S.H. Overbury, *Langmuir*, 2010. **26**(21): p. 16595-16606.
53. Wu, Z., M. Li, D.R. Mullins, and S.H. Overbury, *ACS Catalysis*, 2012. **2**(11): p. 2224-2234.
54. Marks, L.D. and P.M. Voyles, *Microscopy Today*, 2014. **22**(01): p. 65-65.

55. Pennycook, S.J., *Ultramicroscopy*, 1989. **30**(1–2): p. 58-69.
56. Pennycook, S.J. and P.D. Nellist, *Scanning transmission electron microscopy: Imaging and analysis*. 2011, New York: Springer.
57. Hartel, P., H. Rose, and C. Dinges, *Ultramicroscopy*, 1996. **63**(2): p. 93-114.
58. Batson, P.E., *Nature Materials*, 2011. **10**(4): p. 270-271.
59. Cowley, J.M., *Applied Physics Letters*, 1969. **15**(2): p. 58-59.
60. Muller, D.A. and J. Silcox, *Ultramicroscopy*, 1995. **59**(1–4): p. 195-213.
61. Chen, J.G., *Surface Science Reports*, 1997. **30**(1–3): p. 1-152.
62. Hohenberg, P. and W. Kohn, *Physical Review*, 1964. **136**(3B): p. B864.
63. Kohn, W. and L.J. Sham, *Physical Review*, 1965. **140**(4A): p. A1133.
64. Perdew, J.P., K. Burke, and M. Ernzerhof, *Physical Review Letters*, 1996. **77**(18): p. 3865.
65. Marks, L.D., *Ultramicroscopy*, 1992. **45**(1): p. 145-154.
66. Blaha, P. and et al., (Technical Univ. Vienna, 2001).
67. Enterkin, J.A., A.E. Becerra-Toledo, K.R. Poepelmeier, and L.D. Marks, *Surface Science*, 2012. **606**(3–4): p. 344-355.
68. Bardeen, J., *Physical Review Letters*, 1961. **6**(2): p. 57.
69. Tersoff, J. and D.R. Hamann, *Physical Review B*, 1985. **31**(2): p. 805.
70. Marshall, M.S.J., A.E. Becerra-Toledo, L.D. Marks, and M.R. Castell, *Physical Review Letters*, 2011. **107**(8): p. 086102.

71. Van Dyck, D. and M. Op de Beeck, *Ultramicroscopy*, 1996. **64**(1–4): p. 99-107.
72. Yu, Z., D.A. Muller, and J. Silcox, *Journal of Applied Physics*, 2004. **95**(7): p. 3362-3371.
73. LeBeau, J.M., A.J. D'Alfonso, S.D. Findlay, S. Stemmer, and L.J. Allen, *Physical Review B*, 2009. **80**(17): p. 174106.
74. Findlay, S.D., N. Shibata, H. Sawada, E. Okunishi, Y. Kondo, and Y. Ikuhara, *Ultramicroscopy*, 2010. **110**(7): p. 903-923.
75. Okunishi, E., H. Sawada, and Y. Kondo, *Micron*, 2012. **43**(4): p. 538-544.
76. Cowley, J.M. and A.F. Moodie, *Acta Crystallographica*, 1957. **10**(10): p. 609-619.
77. O'Keefe, M.A. in *Proceedings of the 37th Annual Electron Microscopy Society of America Meeting*. 1979. San Antonio, TX: Claitor's.
78. Silly, F., D.T. Newell, and M.R. Castell, *Surface Science*, 2006. **600**(17): p. 219-223.
79. Warschkow, O., M. Asta, N. Erdman, K.R. Poeppelmeier, D.E. Ellis, and L.D. Marks, *Surface Science*, 2004. **573**(3): p. 446-456.
80. Herger, R., P.R. Willmott, O. Bunk, C.M. Schlepütz, B.D. Patterson, and B. Delley, *Physical Review Letters*, 2007. **98**(7): p. 076102.
81. Erdman, N., O. Warschkow, M. Asta, K.R. Poeppelmeier, D.E. Ellis, and L.D. Marks, *Journal of the American Chemical Society*, 2003. **125**(33): p. 10050-10056.
82. Kienzle, D.M., A.E. Becerra-Toledo, and L.D. Marks, *Physical Review Letters*, 2011. **106**(17): p. 176102.
83. Zhu, G.-z., G. Radtke, and G.A. Botton, *Nature*, 2012. **490**(7420): p. 384-387.
84. Cord, B. and R. Courths, *Surface Science*, 1985. **162**(1-3): p. 34-38.

85. Castell, M.R., Surface Science, 2002. **505**: p. 1-13.
86. Johnston, K., M.R. Castell, A.T. Paxton, and M.W. Finnis, Physical Review B, 2004. **70**(8): p. 085415.
87. Andersen, J.E.T. and P.J. Moller, Applied Physics Letters, 1990. **56**(19): p. 1847-1849.
88. Jiang, Q.D. and J. Zegenhagen, Surface Science, 1995. **338**(1-3): p. L882-L888.
89. Møller, P.J., S.A. Komolov, and E.F. Lazneva, Surface Science, 1999. **425**(1): p. 15-21.
90. Nishimura, T., A. Ikeda, H. Namba, T. Morishita, and Y. Kido, Surface Science, 1999. **421**(3): p. 273-278.
91. Silly, F. and M.R. Castell, Applied Physics Letters, 2005. **87**(5): p. 053106-3.
92. Ohsawa, T., K. Iwaya, R. Shimizu, T. Hashizume, and T. Hitosugi, Journal of Applied Physics, 2010. **108**(7): p. 073710-6.
93. Kubo, T. and H. Nozoye, Surface Science, 2003. **542**(3): p. 177-191.
94. Jiang, Q.D. and J. Zegenhagen, Surface Science, 1999. **425**(2-3): p. 343-354.
95. Lanier, C.H., A. van de Walle, N. Erdman, E. Landree, O. Warschkow, A. Kazimirov, K.R. Poepelmeier, J. Zegenhagen, M. Asta, and L.D. Marks, Physical Review B, 2007. **76**(4): p. 045421.
96. Tanaka, H., T. Matsumoto, T. Kawai, and S. Kawai, Surface Science, 1994. **318**(1-2): p. 29-38.
97. Martín González, M.S., M.H. Aguirre, E. Morán, M.Á. Alario-Franco, V. Perez-Dieste, J. Avila, and M.C. Asensio, Solid State Sciences, 2000. **2**(5): p. 519-524.
98. Kubo, T. and H. Nozoye, Physical Review Letters, 2001. **86**(9): p. 1801.

99. Newell, D.T., A. Harrison, F. Silly, and M.R. Castell, *Physical Review B*, 2007. **75**(20): p. 205429.
100. Naito, M. and H. Sato, *Physica C*, 1994. **229**(1-2): p. 1-11.
101. Hiroyuki, T., M. Takuya, K. Tomoji, and K. Shichio, *Japanese Journal of Applied Physics*, 1993. **32**(3S): p. 1405.
102. Liborio, L.M., C.G. Sánchez, A.T. Paxton, and M.W. Finnis, *Journal of Physics: Condensed Matter*, 2005. **17**(23): p. L223-L230.
103. Becerra-Toledo, A.E., J.A. Enterkin, D.M. Kienzle, and L.D. Marks, *Surface Science*, 2012. **606**(9–10): p. 791-802.
104. Matsumoto, T., H. Tanaka, T. Kawai, and S. Kawai, *Surface Science*, 1992. **278**(3): p. L153-L158.
105. Matsumoto, T., H. Tanaka, K. Kouguchi, T. Kawai, and S. Kawai, *Surface Science*, 1994. **312**(1-2): p. 21-30.
106. Newell, D.T. 2007, University of Cambridge.
107. Christopher, R.S., H.H.T. Averyl, L.O. Scott, and W.G. Robin, *Journal of Materials Science*, 2008.
108. Kašpar, J., P. Fornasiero, and M. Graziani, *Catalysis Today*, 1999. **50**(2): p. 285-298.
109. Ikarashi, N., K. Kobayashi, H. Koike, H. Hasegawa, and K. Yagi, *Ultramicroscopy*, 1988. **26**(1–2): p. 195-203.
110. Esch, F., S. Fabris, L. Zhou, T. Montini, C. Africh, P. Fornasiero, G. Comelli, and R. Rosei, *Science*, 2005. **309**(5735): p. 752-755.
111. Wang, H.-F., X.-Q. Gong, Y.-L. Guo, Y. Guo, G.Z. Lu, and P. Hu, *The Journal of Physical Chemistry C*, 2009. **113**(23): p. 10229-10232.



112. Wang, H.-F., H.-Y. Li, X.-Q. Gong, Y.-L. Guo, G.-Z. Lu, and P. Hu, *Physical Chemistry Chemical Physics*, 2012. **14**(48): p. 16521-16535.
113. Tang, Y., H. Zhang, L. Cui, C. Ouyang, S. Shi, W. Tang, H. Li, J.-S. Lee, and L. Chen, *Physical Review B*, 2010. **82**(12): p. 125104.
114. Barton, B., B. Jiang, C. Song, P. Specht, H. Calderon, and C. Kisielowski, *Microscopy and Microanalysis*, 2012. **18**(05): p. 982-994.
115. Wu, Z., V. Schwartz, M. Li, A.J. Rondinone, and S.H. Overbury, *The Journal of Physical Chemistry Letters*, 2012. **3**(11): p. 1517-1522.
116. Chang, S., M. Li, Q. Hua, L. Zhang, Y. Ma, B. Ye, and W. Huang, *Journal of Catalysis*, 2012. **293**(0): p. 195-204.
117. Désaunay, T., G. Bonura, V. Chiodo, S. Freni, J.P. Couzinié, J. Bourgon, A. Ringuedé, F. Labat, C. Adamo, and M. Cassir, *Journal of Catalysis*, 2013. **297**(0): p. 193-201.
118. Sun, C., H. Li, and L. Chen, *Energy & Environmental Science*, 2012. **5**(9): p. 8475-8505.
119. Ta, N., J. Liu, and W. Shen, *Chinese Journal of Catalysis*, 2013. **34**(5): p. 838-850.
120. Agarwal, S., L. Lefferts, B.L. Mojet, D.A.J.M. Ligthart, E.J.M. Hensen, D.R.G. Mitchell, W.J. Erasmus, B.G. Anderson, E.J. Olivier, J.H. Neethling, and A.K. Datye, *ChemSusChem*, 2013. **6**(10): p. 1898-1906.
121. Tasker, P.W., *Journal of Physics C: Solid State Physics*, 1979. **12**(22): p. 4977.
122. Murgida, G.E. and M.V. Ganduglia-Pirovano, *Physical Review Letters*, 2013. **110**(24): p. 246101.
123. Torbrügge, S., M. Reichling, A. Ishiyama, S. Morita, and Ó. Custance, *Physical Review Letters*, 2007. **99**(5): p. 056101.
124. Shidahara, Y., K. Aoki, Y. Tanishiro, H. Minoda, and K. Yagi, *Surface Science*, 1996. **357-358**(0): p. 820-824.

125. Nörenberg, H. and G.A.D. Briggs, *Surface Science*, 1999. **433–435**(0): p. 127-130.
126. Haigh, S.J., N.P. Young, H. Sawada, K. Takayanagi, and A.I. Kirkland, *ChemPhysChem*, 2011. **12**(13): p. 2397-2399.
127. Bhatta, U.M., I.M. Ross, T.X.T. Sayle, D.C. Sayle, S.C. Parker, D. Reid, S. Seal, A. Kumar, and G. Möbus, *ACS Nano*, 2011. **6**(1): p. 421-430.
128. Chen, J.H., H.W. Zandbergen, and D.V. Dyck, *Ultramicroscopy*, 2004. **98**(2–4): p. 81-97.
129. Hojo, H., T. Mizoguchi, H. Ohta, S.D. Findlay, N. Shibata, T. Yamamoto, and Y. Ikuhara, *Nano Letters*, 2010. **10**(11): p. 4668-4672.
130. A, H., *Ultramicroscopy*, 2004. **98**(2-4): p. 73-79.
131. Zhang, Z., W. Sigle, F. Phillipp, and M. Rühle, *Science*, 2003. **302**(5646): p. 846-849.
132. Hýtch, M.J. and W.M. Stobbs, *Ultramicroscopy*, 1994. **53**(3): p. 191-203.
133. Siegel, D.A., W.C. Chueh, F. El Gabaly, K.F. McCarty, J. de la Figuera, and M. Blanco-Rey, *The Journal of Chemical Physics*, 2013. **139**(11): p. 114703.
134. Nolan, M., S. Grigoleit, D.C. Sayle, S.C. Parker, and G.W. Watson, *Surface Science*, 2005. **576**(1–3): p. 217-229.
135. Branda, M.a.M., R.M. Ferullo, M. Causà, and F. Illas, *The Journal of Physical Chemistry C*, 2011. **115**(9): p. 3716-3721.
136. Baghbanzadeh, M., L. Carbone, P.D. Cozzoli, and C.O. Kappe, *Angewandte Chemie International Edition*, 2011. **50**(48): p. 11312-11359.
137. Wu, Z., D.-e. Jiang, A.K.P. Mann, D.R. Mullins, Z.-A. Qiao, L.F. Allard, C. Zeng, R. Jin, and S.H. Overbury, *Journal of the American Chemical Society*, 2014. **136**(16): p. 6111-6122.
138. Skorodumova, N.V., S.I. Simak, B.I. Lundqvist, I.A. Abrikosov, and B. Johansson, *Physical Review Letters*, 2002. **89**(16): p. 166601.

139. Binet, C., A. Badri, and J.-C. Lavalley, *The Journal of Physical Chemistry*, 1994. **98**(25): p. 6392-6398.
140. Bevan, D.J.M., *Journal of Inorganic and Nuclear Chemistry*, 1955. **1**(1-2): p. 49-59.
141. Tsunekawa, S., R. Sivamohan, S. Ito, A. Kasuya, and T. Fukuda, *Nanostructured Materials*, 1999. **11**(1): p. 141-147.
142. Wu, L., H.J. Wiesmann, A.R. Moodenbaugh, R.F. Klie, Y. Zhu, D.O. Welch, and M. Suenaga, *Physical Review B*, 2004. **69**(12): p. 125415.
143. Hailstone, R.K., A.G. DiFrancesco, J.G. Leong, T.D. Allston, and K.J. Reed, *The Journal of Physical Chemistry C*, 2009. **113**(34): p. 15155-15159.
144. Goldschmidt, V.M., F. Ulrich, and T. Barth, Oslo: *Mater. Naturv.*, 1925. **K1**.
145. Brauer, G., in *Progress in the science and technology of the rare earths*. 1968, Pergamon Press: Oxford.
146. Eyring, L., in *Synthesis of lanthanide and actinide compounds*, G. Meyer and L.R. Morss, Editors. 1991, Springer Netherlands. p. 187-224.
147. Adachi, G.-y. and N. Imanaka, *Chemical Reviews*, 1998. **98**(4): p. 1479-1514.
148. Zinkevich, M., D. Djurovic, and F. Aldinger, *Solid State Ionics*, 2006. **177**(11-12): p. 989-1001.
149. Zinkevich, M., *Progress in Materials Science*, 2007. **52**(4): p. 597-647.
150. Perrichon, V., A. Laachir, G. Bergeret, R. Frety, L. Tournayan, and O. Touret, *Journal of the Chemical Society, Faraday Transactions*, 1994. **90**(5): p. 773-781.
151. Tsunekawa, S., S. Ito, and Y. Kawazoe, *Applied Physics Letters*, 2004. **85**(17): p. 3845-3847.
152. Crozier, P.A., R. Wang, and R. Sharma, *Ultramicroscopy*, 2008. **108**(11): p. 1432-1440.

153. Hu, L., C. Wang, S. Lee, R.E. Winans, L.D. Marks, and K.R. Poeppelmeier, *Chemistry of Materials*, 2013. **25**(3): p. 378-384.
154. Wang, R., P.A. Crozier, and R. Sharma, *The Journal of Physical Chemistry C*, 2009. **113**(14): p. 5700-5704.
155. Gao, P., Z. Kang, W. Fu, W. Wang, X. Bai, and E. Wang, *Journal of the American Chemical Society*, 2010. **132**(12): p. 4197-4201.
156. Agoston, P. and K. Albe, *Physical Review B*, 2011. **84**(4): p. 045311.
157. Diehm, P.M., P. Ágoston, and K. Albe, *ChemPhysChem*, 2012. **13**(10): p. 2443-2454.
158. Surrey, A., D. Pohl, L. Schultz, and B. Rellinghaus, *Nano Letters*, 2012. **12**(12): p. 6071-6077.
159. Gerhold, S., Z. Wang, M. Schmid, and U. Diebold, *Surface Science*, 2014. **621**(0): p. L1-L4.
160. Enterkin, J.A., K.R. Poeppelmeier, and L.D. Marks, *Nano Letters*, 2011. **11**(3): p. 993-997.
161. Smith, D.J. and L.D. Marks, *Ultramicroscopy*, 1985. **16**(1): p. 101-113.
162. Rabuffetti, F.A., H.-S. Kim, J.A. Enterkin, Y. Wang, C.H. Lanier, L.D. Marks, K.R. Poeppelmeier, and P.C. Stair, *Chemistry of Materials*, 2008. **20**(17): p. 5628-5635.
163. Blaha, P. and et al., (Technical Univ. Vienna, 2001).
164. Jia, C.L., M. Lentzen, and K. Urban, *Science*, 2003. **299**(5608): p. 870-873.
165. Rabuffetti, F.A., P.C. Stair, and K.R. Poeppelmeier, *The Journal of Physical Chemistry C*, 2010. **114**(25): p. 11056-11067.
166. Poth, J., R. Haberkorn, and H.P. Beck, *Journal of the European Ceramic Society*, 2000. **20**(6): p. 715-723.

167. Becerra-Toledo, A.E., M.R. Castell, and L.D. Marks, *Surface Science*, 2012. **606**(7–8): p. 762-765.
168. Yang, Z., T.K. Woo, M. Baudin, and K. Hermansson, *The Journal of Chemical Physics*, 2004. **120**(16): p. 7741-7749.
169. Baudin, M., M. Wójcik, and K. Hermansson, *Surface Science*, 2000. **468**(1–3): p. 51-61.
170. Baniecki, J.D., M. Ishii, K. Kurihara, K. Yamanaka, T. Yano, K. Shinozaki, T. Imada, K. Nozaki, and N. Kin, *Physical Review B*, 2008. **78**(19): p. 195415.
171. Sheiko, S.S., M. Möller, E.M.C.M. Reuvekamp, and H.W. Zandbergen, *Physical Review B*, 1993. **48**(8): p. 5675-5678.
172. Szot, K. and W. Speier, *Physical Review B*, 1999. **60**(8): p. 5909-5926.
173. Lee, S.B., F. Phillipp, W. Sigle, and M. Rühle, *Ultramicroscopy*, 2005. **104**(1): p. 30-38.
174. Szot, K., W. Speier, U. Breuer, R. Meyer, J. Szade, and R. Waser, *Surface Science*, 2000. **460**(1–3): p. 112-128.
175. Szot, K., W. Speier, J. Herion, and C. Freiburg, *Applied Physics A*, 1996. **64**(1): p. 55-59.
176. Gunhold, A., K. Gömann, L. Beuermann, M. Frerichs, G. Borchardt, V. Kempter, and W. Maus-Friedrichs, *Surface Science*, 2002. **507–510**(0): p. 447-452.
177. Lee, W., J.W. Han, Y. Chen, Z. Cai, and B. Yildiz, *Journal of the American Chemical Society*, 2013. **135**(21): p. 7909-7925.
178. Gunhold, A., L. Beuermann, M. Frerichs, V. Kempter, K. Gömann, G. Borchardt, and W. Maus-Friedrichs, *Surface Science*, 2003. **523**(1–2): p. 80-88.
179. Lin, Y., A.E. Becerra-Toledo, F. Silly, K.R. Poeppelmeier, M.R. Castell, and L.D. Marks, *Surface Science*, 2011. **605**(17-18): p. L51-L55.
180. Wilson, A.R., *Microsc. Microanal. Microstruct.*, 1991. **2**(2-3): p. 269-279.

181. Cancarevic, M., M. Zinkevich, and F. Aldinger, *Calphad*, 2007. **31**(3): p. 330-342.
182. Egerton, R.F., P. Li, and M. Malac, *Micron*, 2004. **35**(6): p. 399-409.
183. Knotek, M.L. and P.J. Feibelman, *Physical Review Letters*, 1978. **40**(14): p. 964-967.
184. Feibelman, P.J. and M.L. Knotek, *Physical Review B*, 1978. **18**(12): p. 6531-6539.
185. Knotek, M.L. and P.J. Feibelman, *Surface Science*, 1979. **90**(1): p. 78-90.
186. Strane, J., L.D. Marks, D.E. Luzzi, M.I. Buckett, J.P. Zhang, and B.W. Wessels, *Ultramicroscopy*, 1988. **25**(3): p. 253-257.
187. Petford, A.K., L.D. Marks, and M. O'Keeffe, *Surface Science*, 1986. **172**(2): p. 496-508.
188. Smith, D.J. and L.A. Bursill, *Ultramicroscopy*, 1985. **17**(4): p. 387-391.
189. Kuwauchi, Y., H. Yoshida, T. Akita, M. Haruta, and S. Takeda, *Angewandte Chemie International Edition*, 2012. **51**(31): p. 7729-7733.
190. Coene, W.M.J., A. Thust, M. Op de Beeck, and D. Van Dyck, *Ultramicroscopy*, 1996. **64**(1-4): p. 109-135.
191. Thust, A., W.M.J. Coene, M. Op de Beeck, and D. Van Dyck, *Ultramicroscopy*, 1996. **64**(1-4): p. 211-230.
192. Akhtar, M.J., Z.-U.-N. Akhtar, R.A. Jackson, and C.R.A. Catlow, *Journal of the American Ceramic Society*, 1995. **78**(2): p. 421-428.
193. Kim, Y.S., J. Kim, S.J. Moon, W.S. Choi, Y.J. Chang, J.-G. Yoon, J. Yu, J.-S. Chung, and T.W. Noh, *Applied Physics Letters*, 2009. **94**(20): p. -.
194. Heifets, E., R.I. Eglitis, E.A. Kotomin, J. Maier, and G. Borstel, *Physical Review B*, 2001. **64**(23): p. 235417.

195. Bengu, E., R. Plass, L.D. Marks, T. Ichihashi, P.M. Ajayan, and S. Iijima, *Physical Review Letters*, 1996. **77**(20): p. 4226.
196. Kang, Y., M. Li, Y. Cai, M. Cargnello, R.E. Diaz, T.R. Gordon, N.L. Wieder, R.R. Adzic, R.J. Gorte, E.A. Stach, and C.B. Murray, *Journal of the American Chemical Society*, 2013. **135**(7): p. 2741-2747.
197. Christensen, S.T., J.W. Elam, F.A. Rabuffetti, Q. Ma, S.J. Weigand, B. Lee, S. Seifert, P.C. Stair, K.R. Poeppelmeier, M.C. Hersam, and M.J. Bedzyk, *Small*, 2009. **5**(6): p. 750-757.
198. Feng, Z., A. Kazimirov, and M.J. Bedzyk, *ACS Nano*, 2011. **5**(12): p. 9755-9760.
199. Guan, Y., D.A.J.M. Ligthart, Ö. Pirgon-Galin, J.Z. Pieterse, R. van Santen, and E.M. Hensen, *Topics in Catalysis*, 2011. **54**(5-7): p. 424-438.
200. Zhang, H., M. Jin, and Y. Xia, *Chemical Society Reviews*, 2012. **41**(24): p. 8035-8049.
201. Hsieh, Y.-C., Y. Zhang, D. Su, V. Volkov, R. Si, L. Wu, Y. Zhu, W. An, P. Liu, P. He, S. Ye, R.R. Adzic, and J.X. Wang, *Nature Communications*, 2013. **4**.
202. Wang, J.X., H. Inada, L. Wu, Y. Zhu, Y. Choi, P. Liu, W.-P. Zhou, and R.R. Adzic, *Journal of the American Chemical Society*, 2009. **131**(47): p. 17298-17302.
203. Mavrikakis, M., B. Hammer, and J.K. Nørskov, *Physical Review Letters*, 1998. **81**(13): p. 2819-2822.
204. Xu, Y., A.V. Ruban, and M. Mavrikakis, *Journal of the American Chemical Society*, 2004. **126**(14): p. 4717-4725.
205. Grabow, L., Y. Xu, and M. Mavrikakis, *Physical Chemistry Chemical Physics*, 2006. **8**(29): p. 3369-3374.
206. Xu, Y. and M. Mavrikakis, *The Journal of Physical Chemistry B*, 2003. **107**(35): p. 9298-9307.
207. Wang, J.X., J. Zhang, and R.R. Adzic, *The Journal of Physical Chemistry A*, 2007. **111**(49): p. 12702-12710.

208. Wang, J.X., F.A. Uribe, T.E. Springer, J. Zhang, and R.R. Adzic, *Faraday Discussions*, 2009. **140**(0): p. 347-362.
209. Yang, X.-F., A. Wang, B. Qiao, J. Li, J. Liu, and T. Zhang, *Accounts of Chemical Research*, 2013. **46**(8): p. 1740-1748.
210. Lin, J., A. Wang, B. Qiao, X. Liu, X. Yang, X. Wang, J. Liang, J. Li, J. Liu, and T. Zhang, *Journal of the American Chemical Society*, 2013. **135**(41): p. 15314-15317.
211. Qiao, B., A. Wang, X. Yang, L.F. Allard, Z. Jiang, Y. Cui, J. Liu, J. Li, and T. Zhang, *Nature Chemistry*, 2011. **3**(8): p. 634-641.
212. Hackett, S.F.J., R.M. Brydson, M.H. Gass, I. Harvey, A.D. Newman, K. Wilson, and A.F. Lee, *Angewandte Chemie International Edition*, 2007. **46**(45): p. 8593-8596.
213. Kim, Y.-T., K. Ohshima, K. Higashimine, T. Uruga, M. Takata, H. Suematsu, and T. Mitani, *Angewandte Chemie International Edition*, 2006. **45**(3): p. 407-411.
214. Fu, Q., H. Saltsburg, and M. Flytzani-Stephanopoulos, *Science*, 2003. **301**(5635): p. 935-938.
215. Rim, K.T., D. Eom, L. Liu, E. Stolyarova, J.M. Raitano, S.-W. Chan, M. Flytzani-Stephanopoulos, and G.W. Flynn, *The Journal of Physical Chemistry C*, 2009. **113**(23): p. 10198-10205.
216. Ghosh, T.K. and N.N. Nair, *ChemCatChem*, 2013. **5**(7): p. 1811-1821.
217. Hu, Z. and H. Metiu, *The Journal of Physical Chemistry C*, 2011. **115**(36): p. 17898-17909.
218. Shapovalov, V. and H. Metiu, *Journal of Catalysis*, 2007. **245**(1): p. 205-214.
219. Song, W., A.P.J. Jansen, and E.J.M. Hensen, *Faraday Discussions*, 2013. **162**(0): p. 281-292.